Fault Location in Grid Connected Ungrounded PV Systems Using Wavelets

A Thesis Submitted

to the College of Graduate Studies and Research

in

Partial Fulfillment of the Requirements

for the Master of Science Degree

in the Department of Electrical and Computer Engineering
University of Saskatchewan

by

Indra Man Karmacharya

Saskatoon, Saskatchewan, Canada

Permission to Use

In presenting this thesis in partial fulfillment of the requirements for a Postgraduate degree from the University of Saskatchewan, it is agreed that the Libraries of this University may make it freely available for inspection. Permission for copying of this thesis in any manner, in whole or in part, for scholarly purposes may be granted by the professors who supervised this thesis work or, in their absence, by the Head of the Department of Electrical and Computer Engineering or the Dean of the College of Graduate Studies and Research at the University of Saskatchewan. Any copying, publication, or use of this thesis, or parts thereof, for financial gain without the written permission of the author is strictly prohibited. Proper recognition shall be given to the author and to the University of Saskatchewan in any scholarly use which may be made of any material in this thesis.

Request for permission to copy or to make any other use of material in this thesis in whole or in part should be addressed to:

Head of the Department of Electrical and Computer Engineering
57 Campus Drive
University of Saskatchewan
Saskatoon, Saskatchewan, Canada
S7N 5A9

Abstract

Solar photovoltaic (PV) power has become one of the major sources of renewable energy worldwide. This thesis develops a wavelet-based fault location method for ungrounded PV farms based on pattern recognition of the high frequency transients due to switching frequencies in the system and which does not need any separate devices for fault location.

The solar PV farm used for the simulation studies consists of a large number of PV modules connected to grid-connected inverters through ungrounded DC cables. Manufacturers report that about 1% of installed PV panels fail annually. Detecting phase to ground faults in ungrounded underground DC cables is also difficult and time consuming. Therefore, identifying ground faults is a significant problem in ungrounded PV systems because such earth faults do not provide sufficient fault currents for their detection and location during system operation. If such ground faults are not cleared quickly, a subsequent ground fault on the healthy phase will create a complete short-circuit in the system, which will cause a fire hazard and arc-flashing. Locating such faults with commonly used fault locators requires costly external high frequency signal generators, transducers, relays, and communication devices as well as generally longer lead times to find the fault.

This thesis work proposes a novel fault location scheme that overcomes the shortcomings of the currently available methods. In this research, high frequency noise patterns are used to identify the fault location in an ungrounded PV farm. This high frequency noise is generated due to the switching transients of converters combined with parasitic capacitance of PV panels and cables. The pattern recognition approach, using discrete wavelet transform (DWT) multi-resolution analysis (MRA) and artificial neural networks (ANN), is utilized to investigate the proposed method for ungrounded grid integrated PV systems.

Detailed time domain electromagnetic simulations of PV systems are done in a real-time environment and the results are analyzed to verify the performance of the fault locator.

The fault locator uses a wavelet transform-based digital signal processing technique, which uses the high frequency patterns of the mid-point voltage signal of the converters to analyze the ground fault location. The Daubechies 10 (db10) wavelet and scale 11 are chosen as the appropriate mother wavelet function and decomposition level according to the characteristics of the noise waveform to give the proposed method better performance. In this study, norm values of the measured waveform at different frequency bands give unique features at different fault locations and are used as the feature vectors for pattern recognition. Then, the three-layer feed-forward ANN classifier, which can automatically classify the fault locations according to the extracted features, is investigated. The neural network is trained with the Levenberg-Marquardt back-propagation learning algorithm.

The proposed fault locating scheme is tested and verified for different types of faults, such as ground and line-line faults at PV modules and cables of the ungrounded PV system. These faults are simulated in a real-time environment with a digital simulator and the data is then analyzed with wavelets in MATLAB. The test results show that the proposed method achieves 99.177% and 97.851% of fault location accuracy for different faults in DC cables and PV modules, respectively. Finally, the effectiveness and feasibility of the designed fault locator in real field applications is tested under varying fault impedance, power outputs, temperature, PV parasitic elements, and switching frequencies of the converters. The results demonstrate the proposed approach has very accurate and robust performance even with noisy measurements and changes in operating conditions.

Acknowledgments

First of all, I would like to express my sincere gratitude to Prof. Ramakrishna Gokaraju for his continuous support, guidance and supervision during my graduate study. His constant patience, enthusiasm, motivation, technical suggestions, and knowledge helped and inspired me to successfully complete my graduate research work and thesis. I am also indebted to Dr. Gokaraju for giving me this opportunity to pursue the M.Sc. program under his supervision and providing me funding from his NSERC Discovery and Engage Grants from Littelfuse Startco.

I would like to acknowledge the support of faculty of the Department of Electrical and Computer Engineering at the University of Saskatchewan that helped me greatly for my research work by building the valuable foundation through different courses, and granting the Department scholarship. I would also like to thank Mr. Kim Haluik, P.Eng, from Littelfuse Startco Inc., for providing funding for my research work. I am also very grateful to Dr. Ali B. Dehkordi and Mrs. Heather Meiklejohn, P.Eng, from RTDS Technologies Inc., for their invaluable suggestions relating to the parameter estimation of the frequency dependent π cable model, and continuous technical supports on real-time modeling and simulations of PV systems.

I would like to extend my thanks to all the students from the Power Systems Simulation Laboratory, especially Mr. Shea Pederson, Mr. Bikash Shrestha, Mr. Binay K. Thakur, Dr. Eli Pajuelo and Mr. Nripesh Ayer, for a pleasant working environment, technical discussions and the continuous support during my stay in the research group.

Finally, I would like to thank my family for their love, understanding, encouragement and constant support throughout my years of study. I owe special thanks to my wife, Mrs. Reena Shrestha for always being an inspiration for me. This thesis would not have been possible without her.

Dedicated

to my

dear wife

Table of Contents

List of Tables

List of Figures

List of Symbols and Abbreviations

AC	Alternating current
A/D	Analogue to digital converter
AI	Artificial Intelligence
ANN	Artificial Neural Network
AWGN	Additive white Gaussian noise
CA	California
coifN	Coiflets wavelet family
CT	Current transformer
CWT	Continuous Wavelet Transform
db10	Daubechies 10 wavelet
dbN	Daubechies wavelet family
DC	Direct current
DFT	Discrete Fourier Transform
DWT	Discrete wavelet transform
EMT	Electromagnetic transient
FFT	Fast Fourier Transform
FIR	Finite impulse response
FPGA	Field-programmable gate array
FT	Fourier Transform
GFDI	Ground fault detection and interruption
GPC	GIGA Processor Card
GPS	Global positioning system
GTWIF	Gigabit Transceiver Workstation Interface Card
GTAI	Gigabit transceiver analogue input card
GTAO	Gigabit transceiver analogue output card
GTDI	Gigabit transceiver digital input card
GTDO	Gigabit transceiver digital output card
GTNET	Gigabit Transceiver Network Interface Card

GUI	Graphical user interface
HIL	Hardware-in-loop
HVDC	High-voltage direct current
IGBT	Insulated-gate bipolar transistor
IMD	Insulation monitoring device
LC	Inductive and capacitive circuit
LCL	Inductance-capacitance-inductance filter
MLP	Multi-layer perceptron
MPPT	Maximum power point tracking
MPP	Maximum power point
MRA	Multi-resolution analysis
MSE	Mean squared error
MVDC	Medium voltage direct current
NC	North Carolina
NCC	Non-current carrying conductor
PB5	Latest Processor card in RTDS
PCC	Point of common coupling
p.f	Power factor
PI	Proportional-integral controller
PV	Photovoltaic
PWM	Pulse width modulation
RC	Resistive and capacitive circuit
RCD	Residual current detector
R/L	Resistive/inductive load
RMS	Root mean square
RSCAD	Software Suite for RTDS
RTDS	Real Time Digital Simulator
RT	Real-time
SC	Short circuit
SIEA	Solar Industries Energy Association

SNR	Signal to noise ratio
SPWM	Sinusoidal pulse-width modulation
SSTDR	Spread spectrum time domain reflectometry
STFT	Short Time Fourier Transform
STC	Standard test condition
STD	Standard deviation
symN	Symlets wavelet family
TDR	Time-domain reflectometry
TW	Traveling Wave
USA	United States of America
U.S NEC	United State National Electric Code
VSC	Voltage source converter
VSI	Voltage source inverter
WIF	Workstation Interface Card
WT	Wavelet Transform
a	Diode ideality factor
a_{ref}	Diode ideality factor at STC
a_j	Approximation coefficients
a_N	Approximation coefficient at level N
C_{lek}	Leakage capacitance of a PV module
C_{dc}	DC-link capacitor
C_f	Capacitor of shunt high pass filter
C_{HG}, C_{HG}	Capacitance between high voltage and low voltage terminals to ground, respectively
C_{HL}	Capacitance between high to low voltage terminals of transformer
D	Duty cycle of converter
d_j	Detailed coefficients
$\|d_j(k)\|$	Norm value of detailed coefficients
E_g	Energy gap of solar cell
F	Ratio of R_p and R_{si}
f	Lowest frequency of interest

f_{sw}	Switching frequency of the inverter
f_n	Nominal (power) frequency
f_{res}	Resonance frequency of harmonic filter
F_s	Sampling frequency of original signal
G	Solar insolation
G_{ref}	Solar insolation at STC
h_1(n)	High-pass filter
h_0(n)	Low-pass filter
$H_1(\omega)$	Frequency response of high-pass filter
$H_0(\omega)$	Frequency response of low-pass filter
I	Output current of a solar cell
I_{ph}	Photo-current
I_D	Diode current of PV cell
I_{sh}	Leakage current through parallel resistance of PV module
I_o	Diode reverse saturation current
$I_{ph_{ref}}$	Photo current at STC
I_{oref}	Diode saturation current at STC
$I_{sc_{ref}}$	Short circuit current of a module at STC
$I_{mp_{ref}}$	Maximum power current of a module at STC
I_{pv}	PV array current
I_{sc}	Short circuit current of PV array
I_{mp}	Maximum power current of PV array
k	Boltzman constant
k_i	Short circuit current temperature coefficient
l	Length of the cable
L_f	Series inductance of AC filter
L_{hf}	Inductance of shunt high pass filter
L_{tr}	Leakage inductance of transformer
N_c	Number of series connected cells in a module
N_{cp}	Number of parallel connected cells in a module

N_p	Number of modules in parallel
N_s	Number of series connected modules
N_L	Decomposition level
P	Real power flow from inverter
P_s	Power of signal
P_n	Power of noise
P_{max}	Maximum power generation of PV array at knee point
q	Electron charge
Q	Reactive power flow from inverter
Q_{ref}	Reference reactive power
R_{iso}	Insulation resistance
R_s	Series resistance of a solar cell
R_{sh}	Parallel resistance of a solar cell
R_{so}	Series resistance of a module at STC
R_{sho}	Parallel resistance of a module at STC
R_p	Parallel insulation resistance of a PV module
R_{si}	Series insulation resistance of a PV module
R_f	Series resistance of AC filter
R_{hf}	Damping resistor of shunt high pass filter
s	Dilation parameter
T	Given temperature
T_{ref}	Temerature at STC
t_k	Target outputs of ANN
t_{on}	Switch on time of converter
T_{cs}	Total switching period of converter
u	Translation parameter
V_{mid1}, V_{mid2}	Mid-point voltages of buck converters
V	Output voltage of a solar cell
V_t	Diode thermal voltage at given temperature
$V_{t_{ref}}$	Diode thermal coltage at STC

$V_{oc_{ref}}$	Open circuit voltage of a module at STC
$V_{mp_{ref}}$	Maximum power voltage of a module at STC
V_{pv}	PV array voltage
V_{oc}	Open circuit voltage of PV array
V_{mp}	Maximum power voltage of PV array
V_{mpp}	Maximum power point voltage
V_{dc}	DC-link voltage
V_{apcc}	Voltage at PCC
V_1	per phase voltage of inverter
$\mathrm{V}_{dc_{ref}}$	DC reference voltage
V_{L-L}	Line to line voltage at PCC
$\mathrm{V}_{dc_{min}}$	Minimum allowable DC-link voltage
W_{signal}	Signal energy
x	Feature vector
X_f	Reactance of filter of inductance
y_k	Actual outputs of ANN
$\mathrm{Z}_{base_{LV}}$	Base impedance at low voltage side of transformer
Z_{cap}	Impedance of filter capacitor
δ	Power angle between inverter and grid
ΔI_L	Inductor ripple current
ω_r	Resonant frequency
ν	Traveling wave velocity
τ	Traveling wave time constant
$\Psi(t)$	Mother wavelet function
$\Psi(t)$	Scaling function

Chapter 1

Introduction

1.1 Background

Photovoltaic (PV) generation systems have made significant progress and have gained popularity in the past few years as a prominent renewable energy source. This trend has been driven mainly by the development of mature technology, growing concerns over climate change, and the falling costs of PV systems. With advancements in nano-technologies, many new materials, devices, and fabrication techniques have been discovered for optimal extraction of power from solar cells, along with significant decreases in the cost of PV panels. According to the Solar Industries Energy Association (SIEA) [1], overall PV system pricing in the USA fell by 17% from 2014 to 2015 and also drastically declined from $8 per watt in 2005 to $2.1 per watt in 2015. Nowadays, people are becoming more concerned about the global environment. Solar PV systems are the best solution for environmental problems associated with traditional energy resources because they do not emit any gas; do not need water, coal, or oil; and do not have rotating parts and are therefore silent.

Figure 1.1 shows the annual growth of solar PV installations in the USA from 2008 to 2015. It can be noted that solar PV deployments in 2015 reached an all-time high of 7,260 MW_{dc}, up 16% over 2014 and 8.5 times the amount installed five years earlier. The residential PV market experienced its largest annual growth rate to date, an impressive achievement given 2015 marked the fourth consecutive year of greater than 50% annual growth. For the last five years, the utility-scale PV market has increased dramatically, accounting for 57% of the capacity installed in 2015.

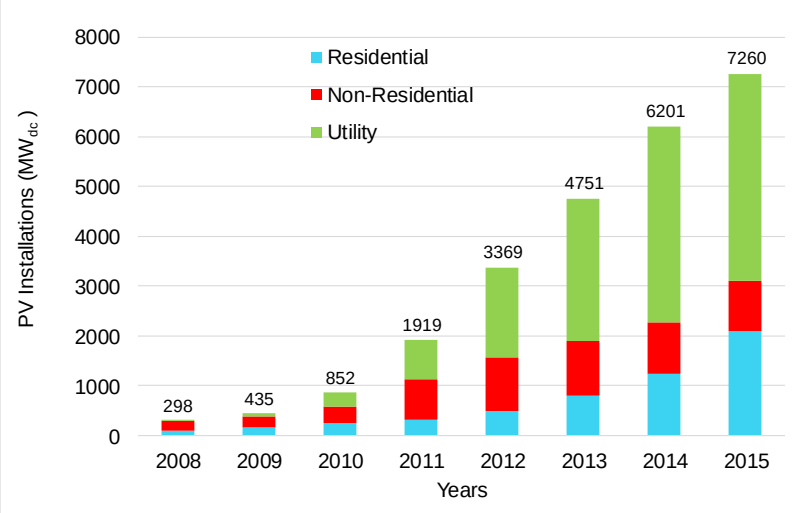

Figure 1.1: Annual USA solar PV installations, 2008-2015 [1]

In recent years, not only did annual installations increase but the capacity of the individual grid-connected utility PV power plants also started trending towards larger sizes (in the range of hundreds of megawatts) to transmit higher amounts of power to the grid system. For instance, the world's largest solar PV power plant in operation is the 579 MW Solar Star Project developed by SunPower Company in Rosamond, California, USA. Particularly in the case of large-scale PV systems, it is important to ensure that reliable operation of the system is maintained by effectively implementing fault monitoring, detection, and diagnosis equipment. Higher capacities result in high bus voltages and current levels in PV systems. Therefore, when ground faults occur on the system, the energy available at the point of the fault increases and can possibly result in arc-flashes, shock hazards, equipment damage, and fires. Thus, it is important when considering ground fault protection of PV farms to understand the difference between a grounded and an ungrounded PV system. The following section briefly explains the functional behaviors of grounded and ungrounded PV systems under ground fault conditions.

1.2 PV System DC Grounding Techniques

The DC side of systems can be grounded and, based on their type of grounding, the systems are classified as grounded or floating (ungrounded). Grounding practices in PV systems vary depending on the operating voltage, size of the plant, type of installation (ground-mount, roof-top, building mounted, floating in water, etc.), and geographic location. According to U.S. NEC Article 690.5, any PV system with a system voltage over 50 V needs ground fault-protection [3]. As is common knowledge, the various types of grounding affect a system's fault tolerance and its response to ground faults.

Generally, a PV system consists of a number of exposed non-current carrying (NCC) metal surfaces such as PV module frames, supporting racks, metal enclosures, distribution panels, a cabinet of power converters, and the chassis of end-use appliances [3,4]. These surfaces could be energized in a fault situation due to electrical contact with current carrying conductors. Therefore, all exposed metals are connected to the earth in both grounded and ungrounded PV systems to avoid the potential risk of electric shock hazard from these exposed metals and to facilitate the operation of protective equipment. This type of grounding in PV systems is referred as equipment grounding.

1.2.1 Grounded PV systems

A grounded PV system has one intentional electric connection from either the positive or negative bus to ground, always situated at the DC side of the inverter. This ground connection is usually made through a ground fault detection and interruption (GFDI) fuse. In such a system, galvanic isolation is generally achieved through the use of an isolation transformer interface between the inverter's electronic AC output and the utility connected AC terminals of the inverter. Grounded PV systems are commonly used in North America. An accidental connection between an energized conductor and grounded surface or earth, termed a ground fault, completes a loop causing significant current flow into ground as shown in Figure 1.2. If the ground fault current overreaches the GFDI fuse rating, the fuse will blow and stop the fault current flowing towards the ground. Thus, for grounded PV systems,

the ground fault is easily detected and located by measuring the fault current with ground fault protection equipment.

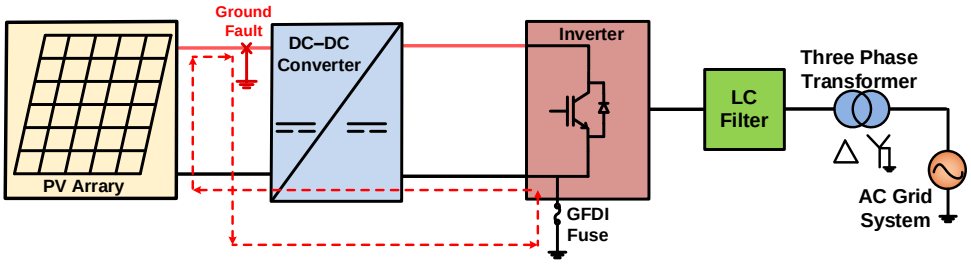

Figure 1.2: A grounded PV system

However, when a ground fault occurs on a grounded conductor or at a location in the array where the potential to ground is low, the fault current will be very low. In these cases, the fault current does not trip the fuse and the ground fault in the PV array remains undetected. This gap in traditional GFDI fuses is described as the "blind spot" [3, 5]. Typically, if the ground fault happened at strings of the PV array during the low solar irradiance period, such as during night, on a cloudy day, or at a time of partial shading, the fault current will be small and the ground fault may not be detected by GFDI fuses. Moreover, if the subsequent ground fault occurs on the unfaulty conductor, it will cause a short circuit in the system and circulate high fault current, resulting in shock and arc-flash hazards, equipment damage, and fire. Hence, it is always important to detect and locate ground faults, and isolate the faulty parts in the system before such severe damage can happen.

A few years ago, PV system fires in Bakersfield, CA, USA (April, 2009) and in Mount Holly, NC, USA (April 2011) were associated with double ground faults in the system. The investigation results revealed that both fire events happened due to undetected ground faults within the blind spot range, followed by a second ground fault on a healthy bus that caused a short circuit in the system and resulted in the flow of a high amount of current through the grounding conductor and damage to the conductor [2, 3, 6]. Figure 1.3 explains with a schematic the fault current paths and how the Mount Holly fire happened.

The first ground fault on the sub-array conductor as shown in Figure 1.3 (a) produced a small current of 2 A through the GFDI fuse, which is lower than the rating of the fuse and

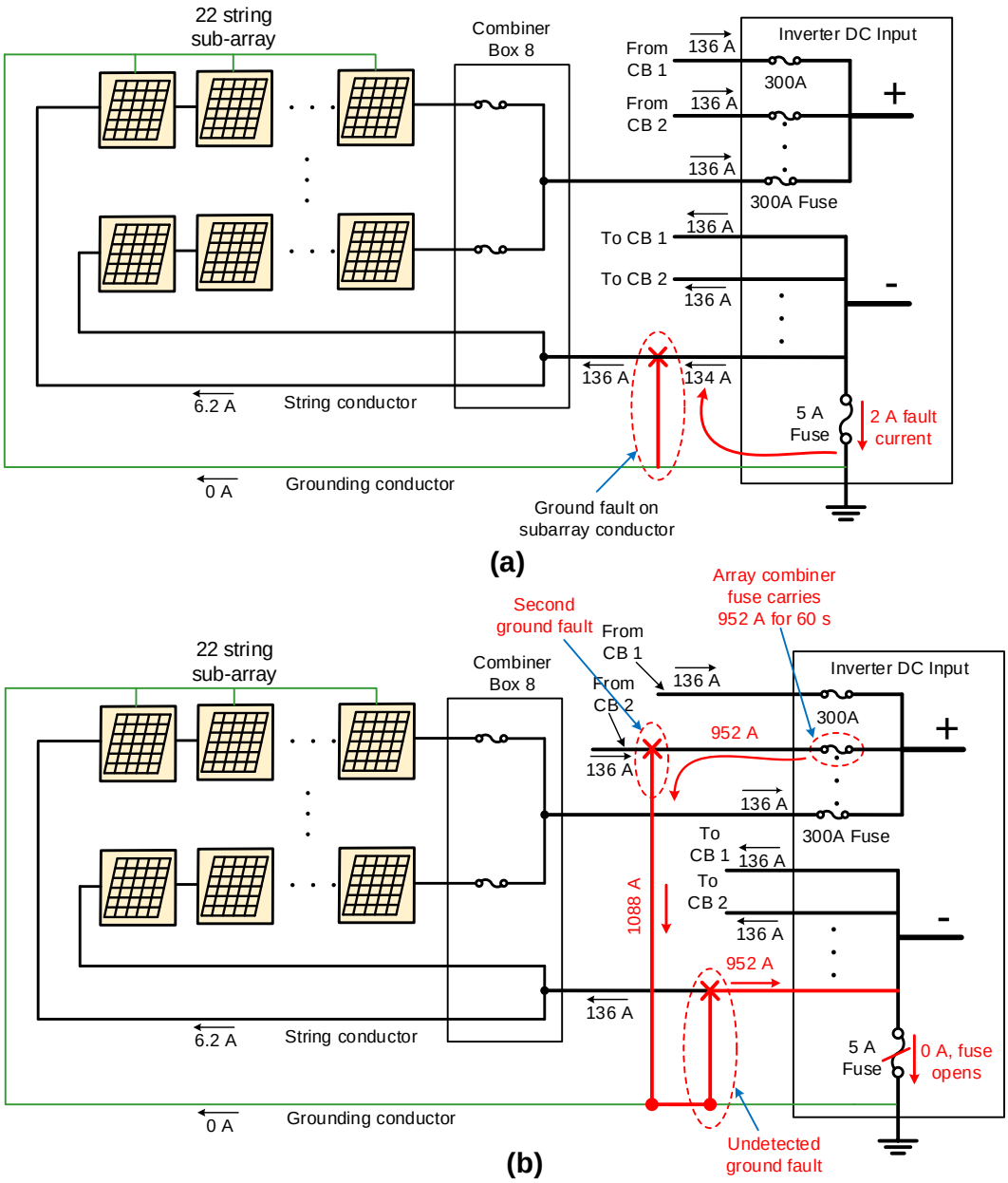

Figure 1.3: Mount Holly fire accident [2]. (a) Undetected ground fault within the blind-spot, (b) Second ground fault resulting in a short circuit and flow 952 A through conductors.

therefore the fault could not be detected. However, the subsequent ground fault in another sub-array conductor created a short circuit in the system that resulted in 952 A current flow through the conductors. This large amount of current initiated a fire before the fault was isolated by an array combiner fuse as shown in Figure 1.3 (b).

1.2.2 Ungrounded PV systems

An ungrounded or floating PV system has no intentional connection from either the positive or the negative bus to ground, as shown in Figure 1.4. Because this type of PV system does not have any connection from bus to ground, there is no parallel current-carrying path between the DC and the AC electrical systems. This means that inverters used with ungrounded PV systems do not require an isolation transformer. Thus, transformer-less inverters are generally used in ungrounded PV systems. It turns out that many of the potential benefits of deploying ungrounded PV systems are specifically associated with the use of transformer-less inverters. The advantages most commonly attributed to non-isolated inverters include higher efficiency, improved economics, and increased ground-fault sensitivity [7].

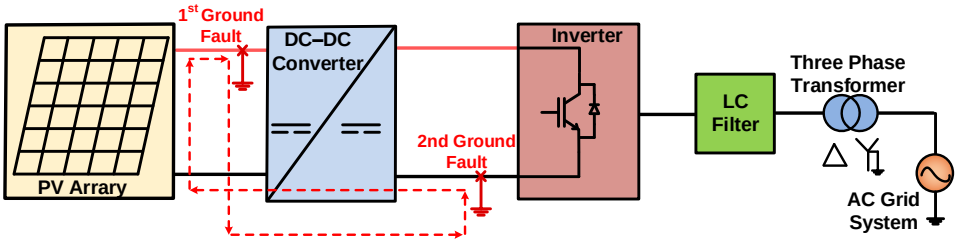

Figure 1.4: An ungrounded PV system

As the inverters in ungrounded PV systems do not have a transformer, power loss is reduced because there are no core and winding losses of the transformer, and efficiency of the inverter is increased. Generally, transformer-less inverters are 1-2% more efficient than transformer isolated inverters. Moreover, with more efficient non-isolated inverters, the PV system's output power can be increased and a high rate of return on investment can be achieved. In addition, by eliminating the isolation transformer in a grid-connected inverter, the cost of the inverter is significantly reduced. As stated earlier, ground faults with a small current can be undetected by GFDI fuses in a grounded system. However, ungrounded PV systems can detect changes in ground current as low as 300 mA, which is an order of magnitude lower than solidy grounded systems [7]. The ground fault protection employed in transformer-less inverters used on ungrounded PV arrays allows for much lower and more

consistent current and trip-time settings. Therefore, ground faults are detected and cleared more quickly before they convert into arcing faults capable of starting a fire. It has been noted that non-isolated inverters are three times more sensitive to ground faults than isolated inverters [7]. Ungrounded PV systems are commonly used in Europe and Asia. Because of the highlighted benefits of transformer-less inverters, however, ungrounded PV systems are now also becoming popular in North America. Furthermore, PV systems are being developed in different areas, such as the sea shore, water surfaces (floating PV), and on aircrafts. In these locations, only ungrounded PV systems can be implemented.

Even though ungrounded PV systems increase the ground fault sensitivity, fault detection and location is not as simple as in a grounded system because a ground fault will not complete a loop and the fault current will not flow. Thus, current sensing ground fault relays cannot be used in cases of ungrounded systems. When the first ground fault occurs on an ungrounded system, the system will become a grounded system and will continue to work as a normal system. However, when a second ground fault occurs on the healthy conductor, as shown in Figure 1.4, a short circuit will happen and result in high fault currents flowing in the system, which might cause shock hazards, arc-flashes and fire. Hence, it is crucial that the ground fault be detected, located and isolated in ungrounded PV systems as soon as possible.

Ground fault detection in ungrounded PV systems is typically achieved by monitoring insulation resistance (R_{iso}) between both current carrying conductors to ground [8–10]. The R_{iso} measured by an insulation monitoring device (IMD) is compared with the minimum threshold insulation resistance recommended in [9]; and it generates the early indication of ground faults if the measured resistance of the system drops below the preset value. This is one of the most sensitive and robust ground fault detection techniques in ungrounded PV systems.

Another popular ground fault protection scheme in ungrounded PV systems is the use of residual current detectors (RCDs) [3, 5]. In this method, RCDs are installed for each string or for the whole array and can measure the differential current entering and leaving the PV system through the positive and negative conductors. When the ground fault occurs, the difference in currents will be higher than the threshold setting for the differential current

recommended in [3, 11], and the RCDs generate a trip signal and open the circuit breaker in the PV system. However, the set point of the RCDs would be computed by considering the leakage current of the PV modules. The RCD fault detection mechanism could be used in both grounded and ungrounded PV systems to protect against ground and line to line faults. It should be noted that both R_{iso} and RCD methods will detect the ground faults anywhere in the system, but locating these faults is more tedious and time consuming in an ungrounded PV system.

1.3 Literature Review

After fault detection, the location of the faults in ungrounded PV systems must be identified for troubleshooting and maintenance of the faulty parts. This process could be inherently difficult and take a long time for a large-scale PV farm.

1.3.1 Fault Location Techniques in Ungrounded PV Systems

Various techniques have been described in the literature regarding fault location methods for ungrounded PV systems. The currently available fault locating technologies used in solar PV systems are listed and summarized here.

1.3.1.1 Injecting and Tracing High Frequency Signals (Bender's method)

The fault location approach currently employed in most industrial ungrounded PV systems is use of a pulse generator to send a high frequency signal into the faulted system and trace the injected signal to locate the fault. This type of fault locating method for high-impedance grounded or ungrounded systems is briefly discussed in [12]. Researchers at Bender Inc., USA, have implemented this approach to fault location in industrial products that, have been commercially distributed in the solar PV industry [8]. The signal, different from the power frequency and switching frequency of converters, is injected between the current carrying conductors and the ground. The injected signal flows into the ground at

the point of the earth fault and returns back to the pulse generator through the ground. Furthermore, the signal can be followed manually by using portable current probes and the exact location of the ground fault can be located. Generally, fault location by tracing the signal consumes a lot of time; there is also the chance of errors because it is done manually. This method can be used to pinpoint ground faults while PV systems are in operation. However, this approach involves tracing the fault point in live equipment enclosures and also requires reaching cables at difficult locations, which increase the risk of arc-flash and shock hazards for working personnel.

Bender's fault location technique can also be implemented for automatic fault locations with fixed installed transducers and relays [13]. With permanently mounted protection devices and current transformers (CTs), the time required and difficulty in finding and isolating ground faults are significantly decreased. However, this method needs more devices (dedicated pulse generators and CTs), which increases cost, complexity, and space in the PV systems.

1.3.1.2 Traveling Wave (TW) Method

Another commonly employed fault location approach in AC and DC transmission lines is the traveling wave-based technique. TWs are naturally occurring surges generated when the fault occurs on the line. In the literature, the TW method has been implemented with single-ended or double-ended principles [14, 15]. The single-ended algorithm estimates the fault location by monitoring the time difference of the fault induced waves and the associated reflected waves at one end of line. On the other hand, the double-ended approach is based on measuring the propagation time of the TWs to reach both terminals of the line using a common reference time. The synchronized time is measured using Global Positioning System (GPS) clocks installed on both sides of the line terminals.

TW technology was presented and implemented to locate faults in AC transmission lines as far back as the early 1950s [16]. With the advancement of communication and digital signal processing technologies, TW-based fault location methods have been implemented in

recent industrial applications for more accurate and reliable fault location estimations. In recent papers [15, 17], TW fault locators were developed in industrial hardware that uses time-synchronized measurements of the TW currents at the line terminals to determine accurate fault locations. It has also been illustrated that the TW fault locator combined into transmission line protective relays can determine the locations of faults to within half a kilometer, or about one tower span, in transmission lines.

Furthermore, TW fault locators are also commonly used in high voltage direct current (HVDC) systems to determine the exact location of faults in transmission lines. In [14], a fault location system for HVDC transmission lines is developed and field operating experiences in a 500 kV HVDC transmission system are described. The maximum location error of the fault location methods is about 3 km, which is higher than in the case of AC transmission lines. Some researchers from the Manitoba HVDC Research Center utilized the wavelet transform to detect the arrival times of TWs and showed an accuracy of 500 m for long HVDC transmission lines [18, 19].

Although modern TW fault locators are highly accurate and reliable for AC and HVDC transmission lines, this technique would be very difficult to implement for small size distribution and distributed generation systems. This is due to a very small propagation time and the low latency between incident waves and associated reflected waves that might be very hard to detect individually in short length cables. The use of GPS systems in short cables also increases the cost of the protection systems.

1.3.1.3 Time Domain Reflectometry (TDR) Method

Time domain reflectometry has been used over the last decade for detection and location of different faults in large solar PV systems. In this approach, an external voltage signal is applied into the system from one end of the line and reflection of the signal from the fault point is monitored along with the incident waveform. In [20], the experimental analysis of injected and reflected waveforms to identify and localize the common faults in a 1 MW PV plant is presented. Other papers discuss the auto-correlation plots (the incident signal with

the reflected signal) generated by spread spectrum time domain reflectometry (SSTDR) to find the location of ground and arc faults in a PV system [21, 22]. The authors also showed that the performance of the SSTDR fault location method do not depend on varying fault current, irradiance and fault resistance. However, the cost of this technology is slightly higher because of the external pulse generator and high frequency sampling requirements.

1.3.1.4 Artificial Intelligence Methods

In the literature, several authors have proposed a fault location method using different artificial intelligence (AI) algorithms. An overview of commonly used AI approaches for transmission line protection is provided in [23]. Artificial neural networks (ANNs) and fuzzy logic are the most commonly used AI techniques for fault diagnosis. Others [24, 25] describe an ANN-based fault locating algorithm for three-phase transmission lines that uses fundamental components of pre-fault and post-fault voltage and current phasors as inputs. The output of the neural network is the estimated fault position. Similar to AC transmission lines, neural networks have also been implemented for fault diagnosis in PV systems [26, 27]. In [27], a fault diagnosis in a PV array, especially for short-circuiting, is proposed using a three-layered feed-forward neural network. The inputs to the ANN in this case are irradiance, temperature, and maximum power point voltage and current. Furthermore, a two-layered ANN is used in [26] to predict the expected power using temperature and insolation as the inputs. An analytical method is combined with ANN outputs to diagnose the PV string faults. However, this method only examines the occurrence and types of faults in the PV strings and the fault location approach has not been investigated. The ANN-based technique is found to be accurate for finding the position of PV faults. This method utilizes raw sampled data as the input to the ANN, and hence it requires long training and computation times.

1.3.1.5 Pattern Recognition Methods

Pattern recognition techniques have been widely utilized over the past few decades in the field of power systems to detect, classify, and locate faults. Generally, wavelet transform-

based MRA is deployed to analyze and extract the features of the fault induced transient waveform, and artificial intelligence algorithms are implemented for pattern recognition. A technique is introduced in [28] based on wavelet multi-resolution signal decomposition for monitoring and classifying typical disturbances in HVDC transmission systems. The technique described in [29,30] analyzes the patterns of the bus voltage and current waveform of transmission line by integrating both DWT and an ANN algorithm. It was shown that the proposed approach precisely detects the fault location in the transmission line with and without series compensation.

Yan Pan in her Ph.D. thesis work [31,32] describes a novel approach for locating ground faults in ungrounded shipboard DC distribution systems that utilizes the high frequency noise generated by repetitive switching of power converters interacting with parasitic elements in the system. The author shows that only one noise containing signal can provide different waveform patterns for ground faults at different positions in the system. These patterns could be decomposed using DWT-based MRA and could classify the fault locations. Moreover, this approach has been tested in an experimental hardware setup and the test results verified the approach to differentiate various fault locations in the real environment [33]. These papers do not discuss how to classify the exact fault location in DC distribution systems.

The noise pattern analysis approach discussed in [34] integrates the wavelet-based MRA technique and ANN for detection and classification of common faults (ground and short circuit) on ungrounded MVDC shipboard power systems. The authors propose a method for selection of a proper mother wavelet and an optimal level of decomposition. The fault diagnosis technique was tested on a real-time platform with hardware-in-loop setup based on a real time digital simulator (RTDS) and a LabVIEW real-time (RT) target. It has been reported that the algorithm has a high accuracy and its performance is not affected by changes in system parameters and environmental noise. However, the author does not discuss the use of the proposed algorithm for locating exact fault positions in DC distribution systems.

The concept of noise patterns generated by inverters has been employed to investigate the fault locating approach in ungrounded grid connected PV systems [35]. The authors

analyzed the feasibility of the ground fault location method in central inverter type PV topology without considering maximum power point tracking of the PV array. It has been shown that it is possible to utilize system noise to locate ground faults in PV systems with the electromagnetic simulation results and wavelet MRA. This work did not analyze the ground and line-line faults on PV panels. The average value based simple classifier proposed has a low fault location accuracy and takes a longer time to pinpoint ground faults in the cables.

1.4 Objective of the Research

The following are the objectives of this thesis in brief:

1. Develop a new pattern recognition-based fault location technique for ungrounded PV systems using DWT-based MRA and a classifier based on ANNs.
2. Develop a real-time simulation model of a utility-scale multi-string ungrounded solar PV system, considering complexities of maximum power point tracking of the PV array and a frequency dependent cable model.
3. Study and analyze the performance of the fault locator under different environmental noise conditions and changes in system parameters of the PV systems.
4. Test, verify, and determine the accuracy of the fault locator for cable and PV module faults in ungrounded PV farms.

1.5 Organization of Thesis

The thesis is organized into five chapters:

Chapter 1 sets the background with discussion of the present scenario of different types of solar PV installations based on system grounding and the importance of ground fault protection in large-scale PV systems. Following this, the various challenges of fault diagnosis

and commonly used fault detection of grounded and ungrounded PV systems are highlighted. A brief review of the literature on different existing fault location techniques in ungrounded PV systems is provided, along with the capabilities and limitations for each of them. This is followed by a discussion of the motivation behind the development of a fault locator that is able to overcome the previously discussed complexities, and which is the primary objective of the thesis.

Chapter 2 explains the real-time electromagnetic simulation model of grid connected multi-string ungrounded PV system. The high-frequency models of the PV system components and its control systems are presented and the requirements of small time-steps in the real-time simulation platform are also explained. Following this, the necessity of frequency dependent cable models in this research and modeling of frequency dependent π cable models are discussed.

Chapter 3 introduces the new pattern recognition-based fault locating approach, which uses unique patterns of high frequency noise generated by interacting switching transients of power converters with parasitic elements of cables and PV panels. Discrete wavelet MRA is chosen instead of different conventional signal processing tools due to its time-frequency resolution advantage, which is able to extract the characteristic features from the noise signal. Following this, the choice of a proper mother wavelet function and number of decomposition scales to extract accurate results from wavelet analysis is discussed. The last section explains the neural network architecture and the training algorithm employed as a fault classifier.

In Chapter 4, detailed simulation and classification results are discussed for different kinds of faults at various locations of the PV system. The feature extraction results for ground and line-line faults in cables and PV panels are described. This is followed by a discussion of results of the ANN classifier for various test scenarios. From the obtained results, the accuracy of the fault locating technique is computed and discussed for cable and PV panel faults. A parameter sensitivity analysis considering varying system parameters and environment noise levels is then conducted to study the feasibility of the fault location approach for practical applications, and the results discussed.

Chapter 5 concludes the research work and the thesis. It provides a summary, thesis contributions, and suggestions for future work.

Appendix A gives the parameters of the test system modeled in this thesis. Appendix B contains cable physical data and the steps to compute the frequency dependent π model parameters along with estimated values.

Chapter 2

Modeling of a Grid Integrated Photovoltaic System

2.1 Introduction

The transient modeling and simulation of grid-connected PV system components are necessary to implement proposed signal processing based fault location method. The main reason is because electromagnetic transient (EMT) simulations provides behavior of the system right from DC to the kHz range. The realistic scenarios of such systems can be implemented by modeling each component in a real-time electromagnetic simulation environment.

In this chapter, the grid-connected multi-string ungrounded PV system is modeled and simulated using real-time EMT simulation software. The design, control, and modeling details of the PV array with its parasitic elements, DC-DC converters and its control for maximum power point tracking (MPPT), and the central inverter and its pulse-width modulation (PWM) controls are discussed. The frequency dependent π cable modeling and the need for frequency dependent cable model for the proposed fault location method is also described.

2.2 Real Time Electromagnetic Transient Simulation

The power system behavior due to switching, short circuits, etc., can be studied with high accuracy using EMT simulations. In order to analyze the system with such high pre-

cision, the power system components need to be modeled at detailed circuit level in time-domain, which increases computing resources, and calculation time of EMTs. Basically, in time-domain approach there are no inherent limitations in studying harmonics, nonlinear effects, and balanced or unbalanced networks [36]. The EMT type simulation uses Dommel formulation based on the work by H. W. Dommel in 1969. EMT type simulations can be done in an off-line mode or in real-time. With offline simulations there are no time constraints involved and it can be made very accurate within the modeling limitations (data, models, and related mathematics).

Real-time simulations use dedicated processors that are capable of generating results in synchronism with a real-time clock. Real-time simulators can be interfaced with physical devices, and data exchange have to be done within the real-time clock, which also imposes restrictions on design of such tools.

The real-time EMT simulation of grid connected PV system was carried out in Real Time Digital Simulator (RTDS) from RTDS Technologie$s^{®}$ Inc. RTDS is a fully digital real time power system simulator extensively used for detailed modeling and simulation of power and control systems, smart grid and distributed generations, power electronic devices, and power hardware-in-the-loop (HIL) studies. RTDS consists of both specially designed hardware and software to perform real-time EMT simulations [37].

The main components of the RTDS are Workstation interface cards (GTWIF or WIF), PB5 Processor cards (PB5), GIGA Processor cards (GPC), analogue input/output cards (GTAI/GTAO, digital input/output cards (GTDI/GTDO), network interface cards (GTNET), and a software RSCAD^{TM}. The RTDS software, called RSCAD, use Graphical User Interface (GUI) particularly designed for interacting with the RTDS simulator hardware. It consists of the unique library with power systems, control systems, and small time-step (power electronics) components. RSCAD allows simulation circuits to be constructed, run, operated, and results to be recorded, and analyzed [38].

The RTDS hardware uses advance parallel processing techniques, which reduce the computational time so that it is capable of providing continuous real-time EMT simulation using

a time-step of 50 μs. Such time-step allows for the simulation of phenomena ranging from 0 to $\simeq$ 3 kHz. In this research, the main power system network (PV array, transformer, load, and grid system) and required control systems were simulated with large time-step of 50 μs. However, such time-steps were not sufficiently small to simulate high frequency switching circuits used in currently available power electronic devices. Thus, to model such power electronic converters, a small time-step simulation was introduced in RSCAD, which uses dedicated high speed processors and some calculation shortcuts in order to reduce time-steps in the range 1.4 to 2.5 μs [39]. All the power electronic converters, and frequency dependent cable models were simulated with small time-steps of 1.4 to 2.5 μs as discussed in the Section 2.4.

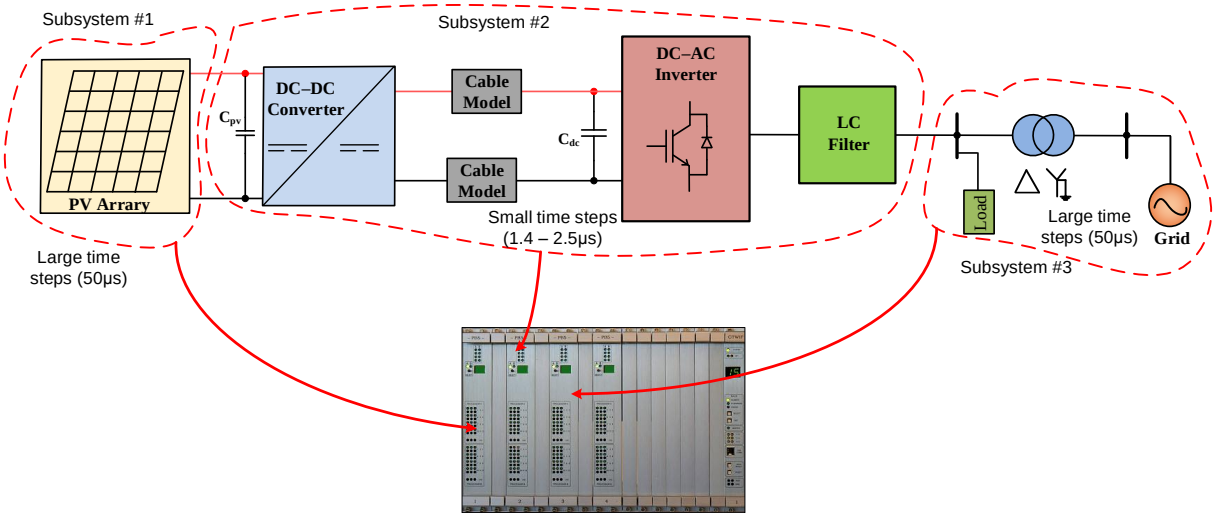

Figure 2.1: Division of simulation in RSCAD

Typically, a large network is divided into sub-networks with large and small time-step subsystems. Each subsystems are assigned to the different processor. Furthermore, the voltage source converter (VSC) bridge simulation is accomplished by allocating a separate processor for small time-step simulations as shown in Figure 2.1.

The power system signals are interchanged between large and small time-step simulations using RSCAD VSC interface transformer components as shown in Figure 2.2 [37]. These transformers can connect the output of the DC/AC converter from small time-step to power system network with large time-step. However, the output of the PV array are purely DC

signals, which can not flow through the transformer, an interface transformer can not be used to interface between PV array and small time-step components.

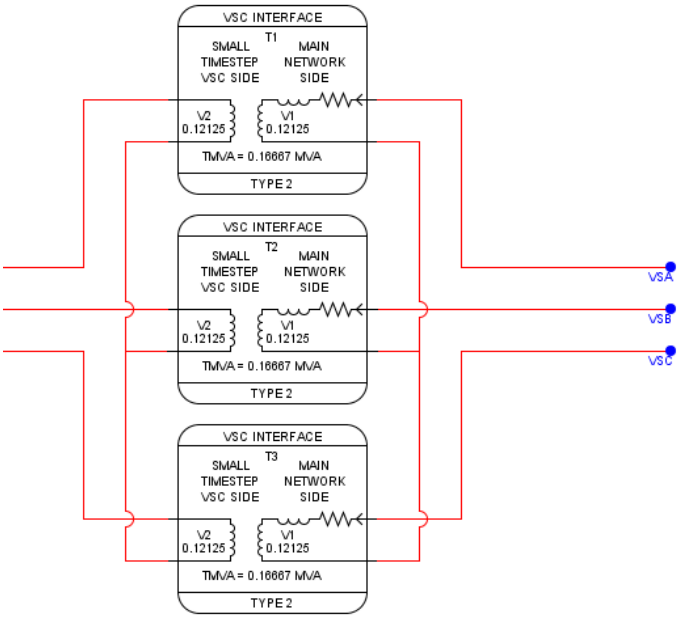

Figure 2.2: RSCAD VSC Interface Transformer

In order to interface the PV array simulated in large time-step with small time-step portions, the voltage and current information has to be transferred between them [37]. Figure 2.3 shows the signals, which can be exchanged between large and small time-step simulations. The output voltage of PV array from large time-step was transmitted to small time-step simulation as a DC voltage source. Furthermore, the current from small time-step side was transferred back to large time-step as a current source branch as shown in Figure 2.3. The power electronic components can be effectively modeled in small time-step, and were interfaced with PV array model simulated in large time-step.

2.3 PV System Configurations

Depending upon the interconnection of PV modules and converters, a number of different configurations of grid connected PV systems have been developed and used over last few

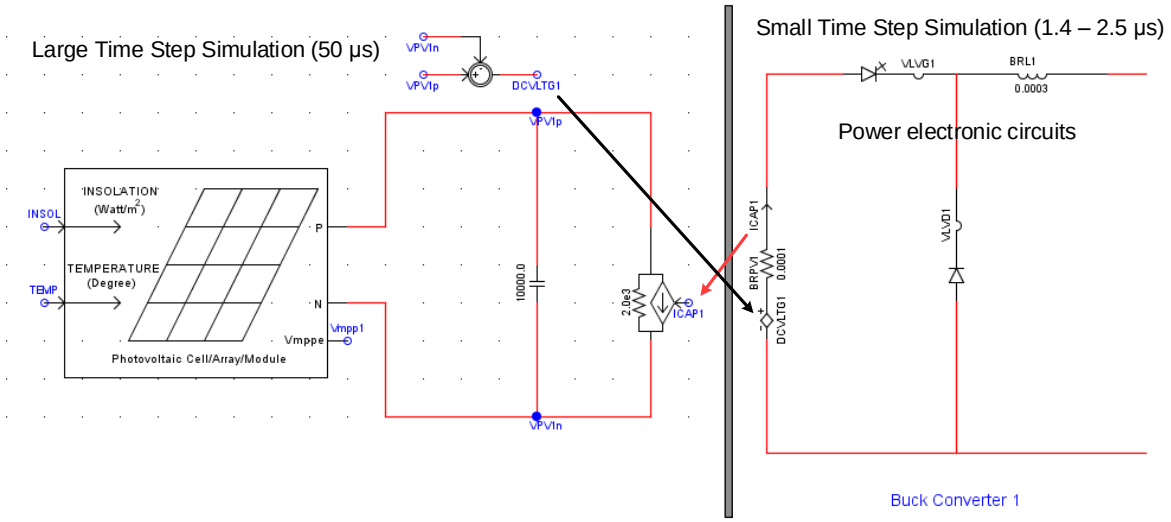

Figure 2.3: PV array interface with a small time-step simulation in the RSCAD

decades. A detailed review of such available topologies were discussed in [40–44]. The three kinds of PV system configurations are presented in Figure 2.4 and discussed below:

2.3.1 Central Inverter Type

In central inverter structure, the number of series and parallel connected modules are directly connected to a single central inverter as shown in Figure 2.4(a). Special diodes are required to allow different string voltage in common DC bus. This topology has several drawbacks, such as power loss due to module mismatch and partial shading conditions, losses in diodes, and it is less reliable because of the possibility of failure of the central inverter, which will result in entire failure of the PV plant. However, due to high efficiency of large inverters, low cost, and simplicity of utilizing single inverter, central inverter topology is commonly used for the large-scale PV systems (typical $>$ 350 kW) [45].

2.3.2 String Inverter Type

In string inverter structure, the number of PV modules are connected in series to form PV string, and individual PV string is integrated to grid by small designated inverter as

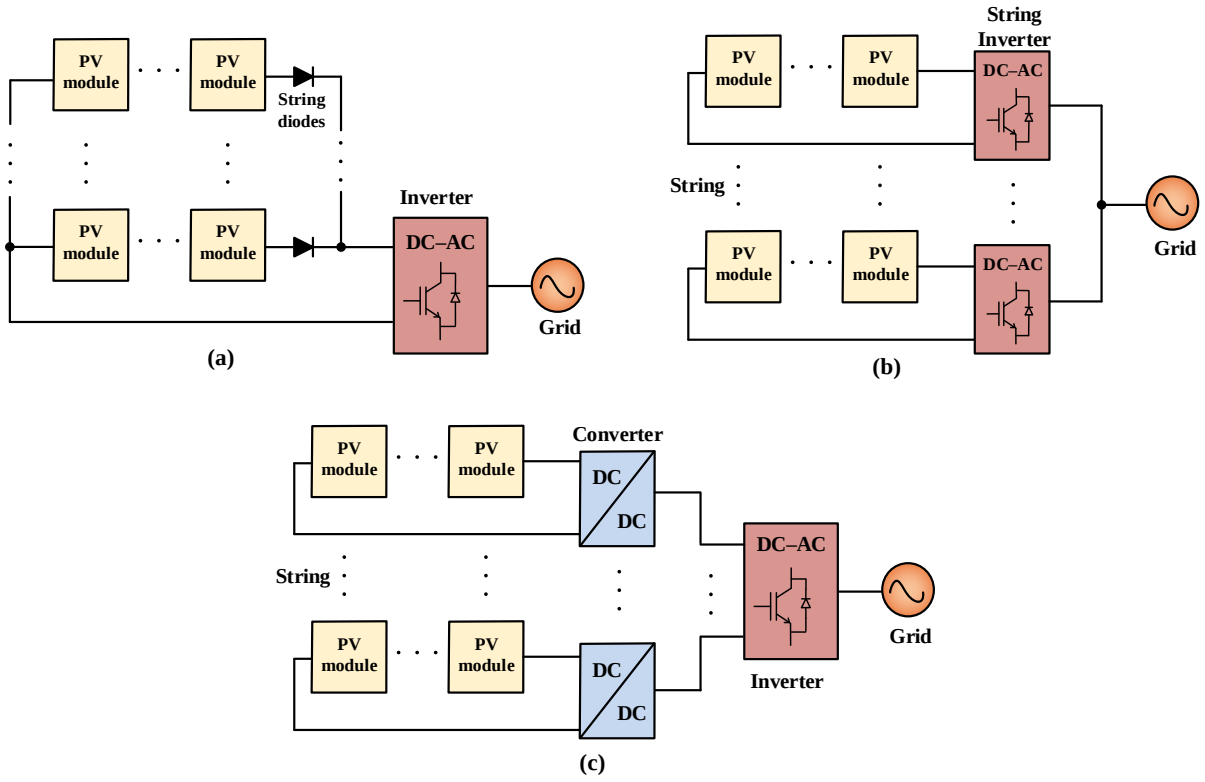

Figure 2.4: Topologies of PV systems: a) Central inverter, b) String inverter, c) Multi-string inverter

shown in Figure 2.4(b). Each string inverters have their own MPPT that reduce the module mismatch and partial shading losses. The system reliability is increased due to number of string inverters. However, for large-scale systems (typical $>$ 350 kW), the cost will be considerably high due to the large number of inverters. Also, the string inverter has a power limit due to limited number of series connections in order to increase the nominal power [40].

2.3.3 Multi-String Converter Type

The multi-string converter structure has been developed to combine advantage of string inverter and central inverter topology. Each string is connected to individual DC/DC converter, and interfaced to central inverter through common DC bus as shown in Figure 2.4(c). Each DC-DC converter is used to implement MPPT scheme of individual string, which will reduce the mismatch and partial shading problems. Accordingly, this topology provides

better overall efficiency, low cost, independent control, integration of PV strings of different technologies, and can be used for different PV orientations [43].

Multi-string configuration is commonly used in utility-scale PV system due to aforementioned advantages. In this research, multi-string grid connected ungrounded PV system was used as a test system, and fault location in the PV farm and the cables are investigated.

2.4 500 kWp Grid Connected Multi-String Ungrounded PV Test System

A test system shown below in Figure 2.5 was modeled and simulated in real-time simulation environment in RTDS. A multi-string ungrounded PV system was connected to grid using 500 kW, three-phase, two level voltage source inverter (VSI), which converts DC power generated from PV array into AC power. Two 250 kWp PV array were connected to individual DC-DC converter (buck converter) to implement MPPT technique to achieve maximum efficiency of PV array. Each PV array has 48 parallel strings, and each string consists of 17 modules connected in series. The parameter of PV modules are shown in Appendix A.1. The multi-string PV arrays were connected to 600 V common DC bus through DC underground cables, and DC bus was integrated with the DC-link capacitor, and input terminal of three-phase inverter. The VSI and DC-DC converters were controlled based on sinusoidal pulse-width modulation (SPWM) technique.

Harmonic filter connects the output terminals of the VSI to respective phases of point of common coupling (PCC). The 500 kVA, 0.21/20 kV, three-phase, Δ/Y, step-up transformer was used to transfer PV power to distribution system. Station service load of 100 kW, and a 210 V, unity p.f, three-phase dynamic load was connected to the output of the inverter at PCC. The mid-point voltages (V_{mid1} or V_{mid2}) of DC-DC converters with respect to grounding were measured and analyzed using signal processing method described in Chapter 3 for detection and location of fault in the PV system. Ground faults at different locations are shown in Figure 2.5 to implement the proposed fault location method. The detailed de-

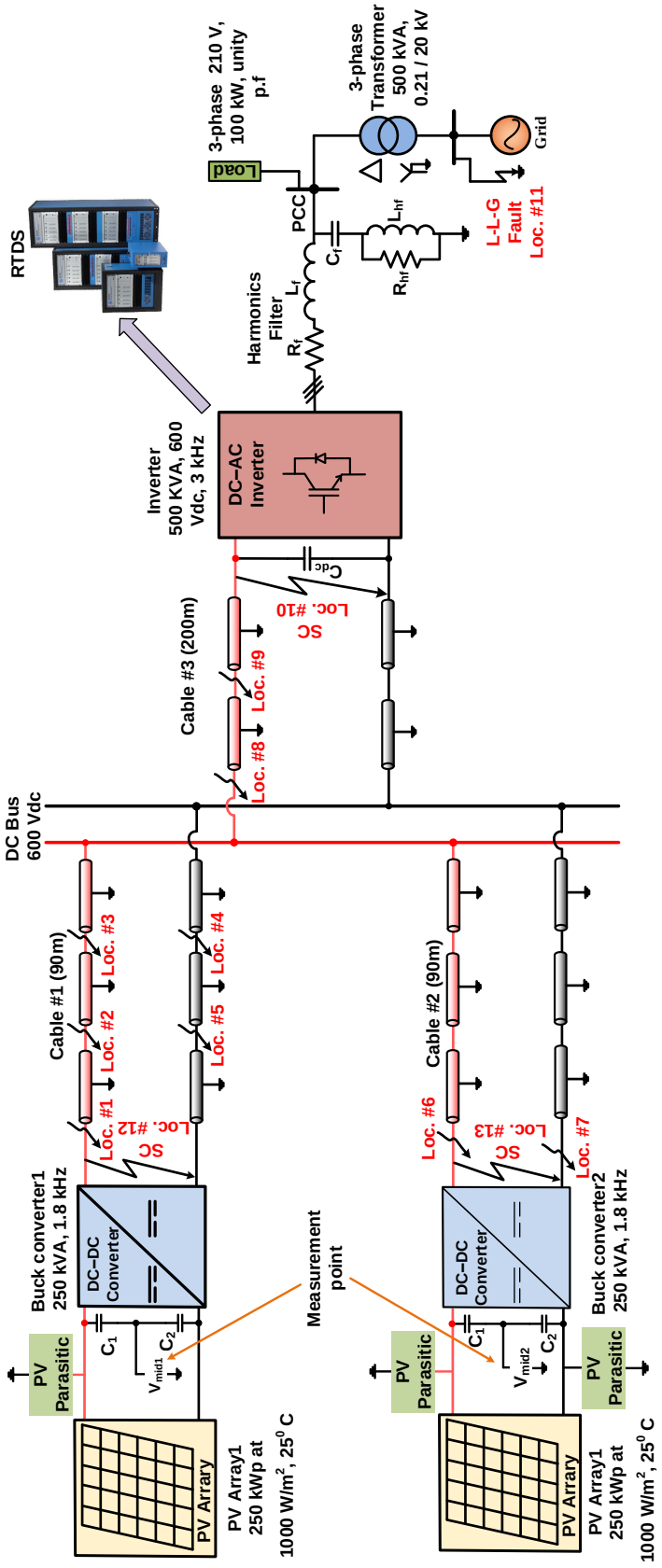

Figure 2.5: 500 kWp multi-string grid integrated solar PV system

sign, control, and modeling of individual component of PV test system are presented in the following sections.

2.4.1 PV Array Modeling

Solar cell is a fundamental component of a solar array. The single solar cell produces very small power, and in order to produce enough power to supply load, each cell is connected in series and/or parallel to form a module. The PV modules are then combined in series and parallel to form PV arrays as shown in Figure 2.6. The combination of individual solar cells into PV arrays enables higher values of voltages and currents to be obtained at terminals of PV array. Suppose that the number of series connected cells in a module is denoted by N_c, the number of parallel connected cells in a module is N_{cp}, the number of modules in parallel is N_p, and the number of series connected modules is denoted by N_s.

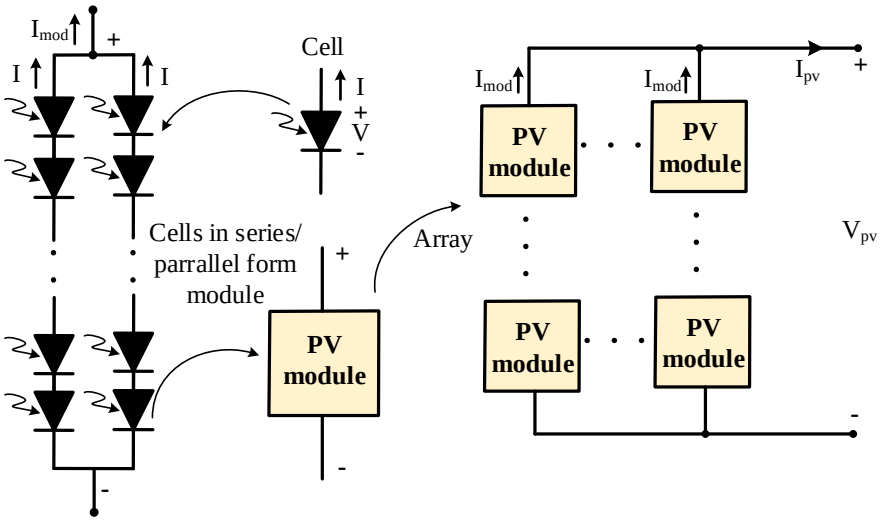

Figure 2.6: Elements of PV array

2.4.1.1 Mathematical model of solar cell

A solar cell is a non-linear device having a current-voltage characteristics, which depends on solar radiation and ambient temperature. Single-diode model and double-diode model are

most commonly used to represent the electrical characteristics of solar cells [46, 47]. Single diode model accurately represents nonlinear current-voltage characteristics of solar cell by including a series and parallel resistance with ideal solar cell as shown in Figure 2.7.

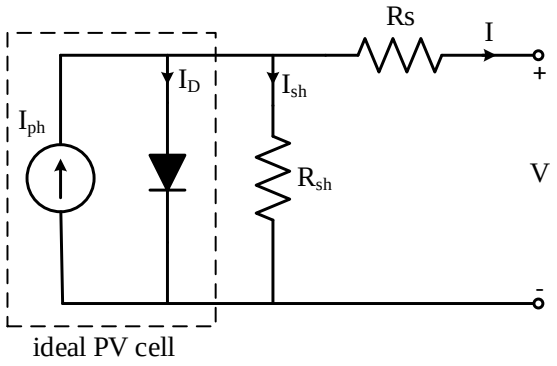

Figure 2.7: Single diode five parameter model of PV cell

RTDS/RSCAD PV array was modeled either using single diode five parameter model or single diode four parameter model as explained in [37]. From the equivalent circuit of a single diode five parameter model, the output current of solar cell could be written as:

$$I = I_{ph} - I_D - I_{sh} \tag{2.1}$$

$$I = I_{ph} - I_o \left[exp\left(\frac{V + R_s I}{N_c a V_t} \right) - 1 \right] - \frac{V + R_s I}{R_{sh}} \tag{2.2}$$

where I_{ph} is photo-current, I_D is diode current of PV cell, I_o is diode reverse saturation current, and a is diode ideality factor, which measures the closeness of diode performance with ideal diode equation. R_s and R_{sh} are series and parallel resistances of solar cell, respectively, and I_{sh} is leakage current through the parallel resistance. V_t is the diode thermal voltage at any given temperature T(in K), which is expressed as:

$$V_t = \frac{kT}{q} \tag{2.3}$$

where $k = 1.3806503 \times 10^{-23}$J/K, the Boltzman constant, and $q = 1.60217 \times 10^{-19}$C, an

electron charge.

The photo-current of PV cell depends linearly on the solar insolation $G\,(W/m^2)$, and the temperature T (in K) according to the following Equation [47]

$$I_{ph} = \left[I_{ph_{ref}} + k_i(T - T_{ref})\right] \frac{G}{G_{ref}} \tag{2.4}$$

The diode saturation current and ideality factor are also dependent on temperature and defined as:

$$I_o = I_{oref} \left(\frac{T}{T_{ref}}\right)^3 exp\left[\frac{E_g}{aV_t}\left(1 - \frac{T_{ref}}{T}\right)\right] \tag{2.5}$$

$$I_{oref} = \frac{I_{sc_{ref}}}{exp(V_{oc_{ref}}/aV_{t_{ref}}) - 1} \tag{2.6}$$

$$a = a_{ref}\left(\frac{T}{T_{ref}}\right) \tag{2.7}$$

where $I_{ph_{ref}}$ is light generated current at standard test condition (STC) i.e., $G_{ref} = 1000\,W/m^2$, and $T_{ref} = 25^0\,C$. I_{oref} and a_{ref} are diode saturation current, and ideality factor at STC, respectively. E_g is energy gap (eV) of solar cell semiconductor material, and k_i is short circuit current temperature coefficient $(\%/^0\,C)$. $V_{t_{ref}}$ is diode thermal voltage at STC.

Typically, parameters $I_{ph_{ref}}$, I_{oref}, a_{ref}, R_s, R_{sh} are not provided by PV manufacturers. These parameters have to be estimated from specific data short circuit current ($I_{sc_{ref}}$), open circuit voltage ($V_{oc_{ref}}$), maximum power voltage ($V_{mp_{ref}}$), maximum power current ($I_{mp_{ref}}$), series resistance (R_{so}), and parallel resistance (R_{sho}) available on the PV data sheets for STC. The RTDS PV array model include option to estimate unknown PV cell parameters using either an analytical method or an iterative method [37].

After estimation of solar cell parameters from analytical or iterative methods, the total PV array current (I_{pv}) was calculated using Equation 2.2, 2.4, 2.5, and 2.7 as below:

$$I_{pv} = N_{cp}N_pI_{ph} - N_{cp}N_pI_o\left[exp\left(\frac{V_{pv} + \frac{N_s}{N_pN_{cp}}R_sI_{pv}}{N_sN_{cs}aV_t}\right) - 1\right] - \left(\frac{V_{pv} + \frac{N_s}{N_pN_{cp}}R_sI_{pv}}{\frac{N_s}{N_pN_{cp}}R_{sh}\frac{G}{G_{ref}}}\right), \tag{2.8}$$

where V_{pv} is PV array output voltage.

For STC (insolation = 1000 W/m^2 and temperature = $25^0\,C$ values), the operating point of PV array was found from I-V characteristics as shown in Figure 2.8. The curves range from the short circuit current (I_{sc}, 0) to the open circuit voltage (0, V_{oc}). The maximum electrical power (P_{max}) generation is at the knee point (I_{mp}, V_{mp}).

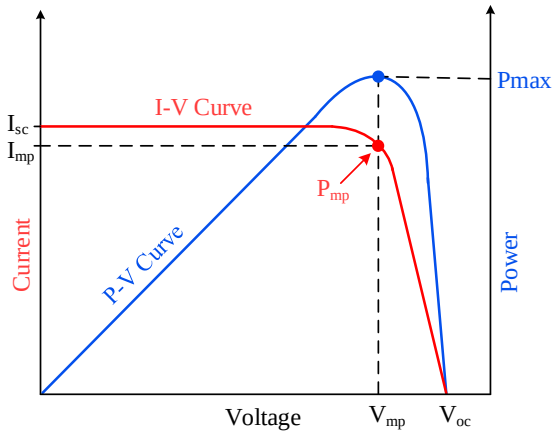

Figure 2.8: I-V and P-V curve of a PV array

2.4.1.2 PV Parasitic Elements

The RTDS/RSCAD PV model discussed in Section 2.4.1.1 do not consider insulation between PV module and ground. A complete electrical model of PV array and PV insulation to ground is required to analyze ground faults in an ungrounded PV system. PV electrical insulation is also important for safety; it can vary from kΩ to MΩ under normal operating conditions depending upon PV array sizes, PV insulation characteristics, and also other environmental conditions. Therefore, an equivalent circuit model simulating the behavior of PV module insulation was proposed in [48], as shown in Figure 2.9. Here, the PV module insulation has leakage capacitance C_{lek}, series insulation resistance R_{si}, and parallel insulation resistance R_p.

The PV array insulation resistance was calculated from following mathematical expres-

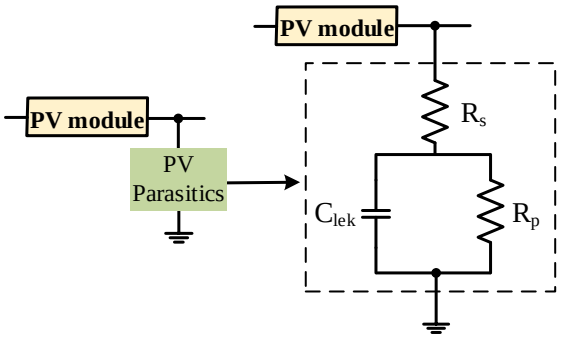

Figure 2.9: Equivalent circuit model for insulation of a PV module

sion:

$$R_{iso} = \frac{R_{si} + R_p}{N_p \times N_s}, \tag{2.9}$$

where F parameter is equal to R_p/R_{si}, and R_{iso} is PV array insulation resistance. Therefore, R_{si} and R_p are defined as:

$$R_s = \frac{\frac{R_{iso}}{N_p \times N_s}}{1+F}, \qquad R_p = F \times R_{si} \tag{2.10}$$

The parasitic elements R_{si}, R_p, and C_{lek} are dependent on meteorological variables, such as relative humidity, module temperature, solar irradiance, wind speed, and air pressures. The effects of meteorological variables in PV insulation parameters of a real 68 kWp PV system were analyzed and discussed in [48].

In normal operating conditions, the value of insulation resistance and leakage capacitance were measured as $R_{iso} \in [0.12,\ 4.6]$ MΩ, and $C_{lek} \in [0.7,\ 42]$ μF in a real 68 kWp PV generator, respectively [48]. Moreover, an estimation of PV parasitic capacitance was also analyzed and provided that PV module made with crystalline silicon cells has capacitance of [60-110] nF per kW of installed DC power [49]. Based on above equations and measurement results, parasitic elements of PV arrays were approximated, and are tabulated in Appendix A.2.

2.4.2 Maximum Power Point Tracking Control

It is shown from I/V and P/V characteristics of PV array (Figure 2.8), the power generated is nonlinear, and there is one operating point where power is maximum. In order to achieve maximum efficiency of PV array, the PV array is operated at maximum power point (MPP). The MPP of the PV array depends on module temperature and solar insolation, so it is necessary to constantly track MPP point of PV array. Therefore, MPPT technique is used to maintain the PV array operating at its MPP.

The different types of MPPT algorithms are well established in the literature. They can be broadly categorized as (a) direct methods, (b) indirect methods, and (c) artificial intelligent methods. Direct methods includes, perturbation and observation, and incremental conductance method [50]. Indirect methods like fractional open circuit voltage [51], Lambert function approximation [52], curve fitting [53], etc., were also used to estimate MPP. Artificial intelligent-based MPPT techniques were also proposed in [54].

The RTDS/RSCAD PV model include an option to estimate MPP for given insolation and temperature using Lambert function approximation, and Fractional open circuit voltage approximation [37]. Direct MPPT methods; incremental conductance, and perturbation & observation can be also implemented using MPPT control component in the RSCAD.

2.4.2.1 MPPT Implementation

The MPPT technique was implemented in DC-DC converters to extract maximum power from PV arrays. Buck and boost DC-DC converters are mostly used topologies. However, in this research, buck converter was proposed for MPPT control as shown in Figure 2.10. The maximum efficiency of PV array was achieved by maintaining output voltage of PV array to MPP voltage for given irradiance and temperature.

The MPP reference voltage (V_{mpp}), at which PV array is to be operated, was obtained from Lambert function approximation MPPT algorithm. Then, PV array output voltage (V_{pv}) was compared with reference voltage (V_{mpp}), and error signal was used as input to

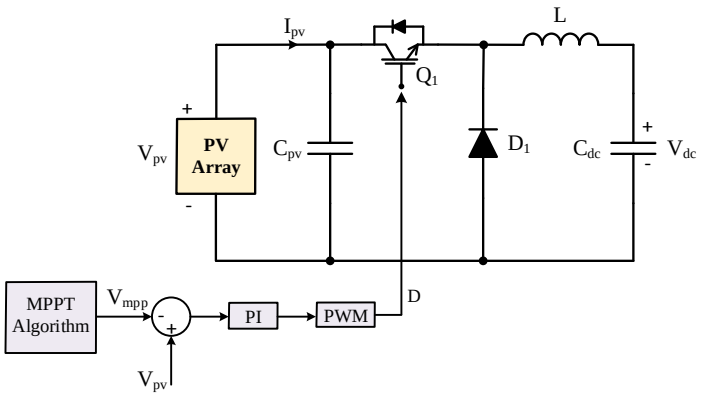

Figure 2.10: MPPT control circuit using buck converter

proportional-integral (PI) controller as shown in Figure 2.10 [55]. The duty cycle (D) of buck converter was generated by PWM technique, as explained in Section 2.4.3.2, by comparing output of PI controller with the high frequency triangular wave. The PWM signal was supplied to gate terminal of IGBT switch (Q_1), which control the on and off time of switch so that the output of PV array follow the reference voltage.

The input and output voltage relationship of the buck converter is given by Equation 2.11 [56]:

$$V_{dc} = D \times V_{pv}, \tag{2.11}$$

where the duty cycle (D) of converter is equal to ratio of switch on time (t_{on}) to total switching period (T_{cs}).

For the given test system, DC-link voltage (V_{dc}) must be adjusted at fixed reference value. Therefore, there is a fixed relationship between (V_{pv}) and duty cycle. From Equation 2.11, the output voltage of PV array can be maintained at MPP voltage by controlling the duty cycle of the buck converter. The parameters of the buck converter are designed considering output ripple current equal to 30% of the rated output current [57]. The switching frequency of 1.8 kHz was used for both DC-DC converters. The detailed parameters of buck converter and PI controller are presented in Appendix A.3.

2.4.3 PV Inverter Modeling

The transformer-less, ungrounded, voltage source inverter (VSI) was used as a grid-tied inverter to convert DC power output from PV array to AC power. The primary function of VSI was to convert fixed DC voltage to three-phase AC voltage with variable magnitude and frequency [58]. The most commonly used two-level three-phase VSI was implemented as central inverter for proposed PV test system as shown in Figure 2.5. The simplified schematic diagram of two-level three-phase VSI is also shown in Figure 2.11.

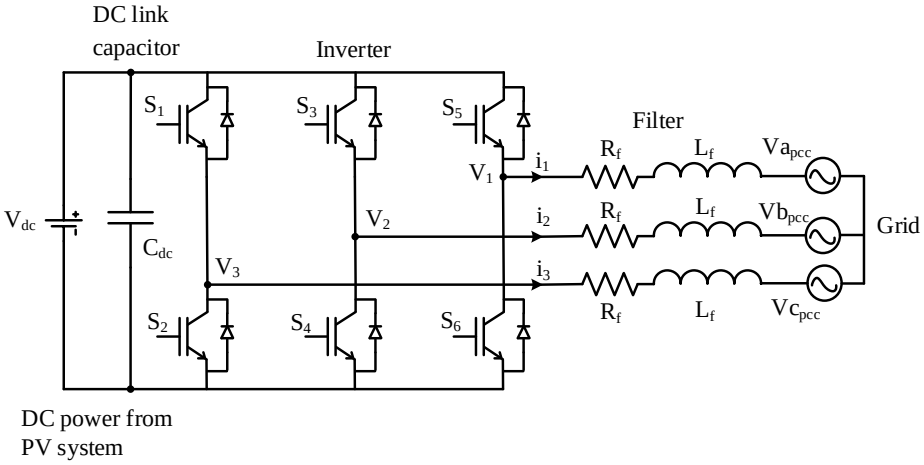

Figure 2.11: Two-level, three-phase voltage source inverter

2.4.3.1 Voltage Source Inverter Control

Different VSI control principles were investigated in literature the [59–62]. One way to control VSI is power-angle control or voltage control, and another method is vector control or current control. In voltage control method, an AC terminal voltage is controlled to maintain at reference value. However, in current control method, the inverter output currents are controlled to remain at reference current. The pros and cons of both control algorithms were analyzed in [59–61]. Voltage control technique was employed in this thesis for the operation of VSI due to simplicity of implementation.

The relationship between inverter output voltage and PCC voltage can be represented by the phasor diagram as shown in Figure 2.12, and resistance of filter is very small so that it is neglected in phasor diagram [62]. The real and reactive power flow between inverter and grid can be written as:

$$\begin{aligned} P &= \frac{V_1 V_{a_{pcc}}}{X_f}\delta, \\ Q &= \frac{V_1(V_1 - V_{a_{pcc}})}{X_f}, \end{aligned} \tag{2.12}$$

where V_1 and V_{apcc} are per phase inverter output voltage and PCC voltage, respectively. X_f is reactance of filter inductance, and δ is phase angle between V_1 and V_{apcc}, which is so small that it is approximated $sin(\delta) \approx \delta$ and $cos(\delta) \approx 1$.

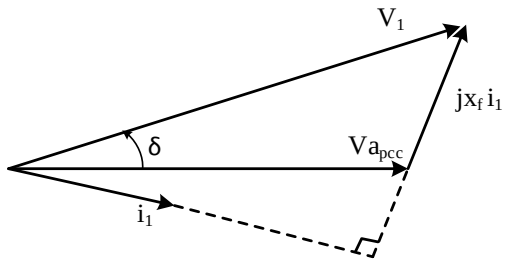

Figure 2.12: Phasor diagram of voltage angle control

From Equation 2.12, it is obvious that active power mainly depends upon phase angle (δ), and reactive power is proportional to the voltage magnitude difference. Thus, the real power can be controlled by varying the voltage phase angle, and the reactive power can be controlled by adjusting the voltage magnitude of the inverter output.

In order to implement voltage control algorithm, simple active power (P) controller and reactive power (Q) controller were designed as shown in Figure 2.13, and Figure 2.14, respectively [55]. The P-controller shown in Figure 2.13 maintains DC link voltage (V_{dc}) to required DC reference voltage ($V_{dc_{ref}}$), which in this case is 600 V DC, using PI controller. The DC reference voltage ($V_{dc_{ref}}$) was used as base voltage for DC side of the system. Hence, the output of PI controller (Ang) was phase angle (δ) in radians and can be used as input

to PWM as discussed in Section 2.4.3.2. The limiter used in P-controller limits the phase angle value within -1.57 to +1.57 radians (-90^0 to $+90^0$ degrees).

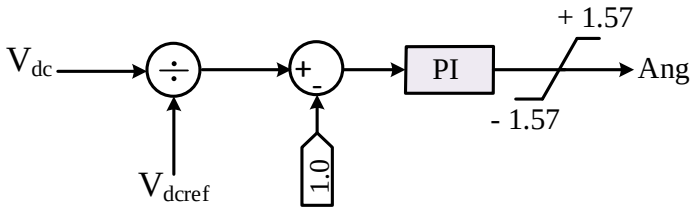

Figure 2.13: Active power controller

The second PI controller shown in Figure 2.14 is used to adjust reactive power (Q_{meas}) flow from the inverter to the required reactive power (Q_{ref}) value. The output reactive power (Q_{meas}) was converted into per-unit value using inverter rating as base MVA. Hence, the output of PI controller (Mag) was per-unit voltage magnitude, which is limited between 0 to 1. The voltage magnitude signal (Mag) was also used as input to PWM as discussed in Section 2.4.3.2. The parameter of PI controllers were tuned by trial and error method, and tabulated in Appendix A.4.

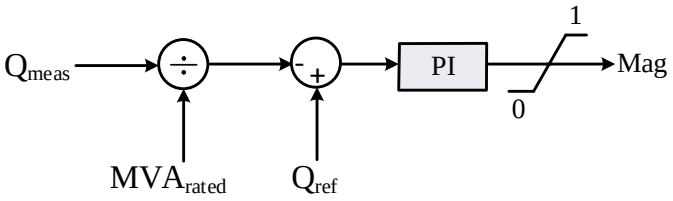

Figure 2.14: Reactive power controller

2.4.3.2 Pulse Width Modulation (PWM)

The SPWM scheme was used to achieve firing pulse of six IGBT switches ($S_1 - S_6$) of two level three-phase inverter as shown in Figure 2.11. The switching signals were determined by comparing sinusoidal modulating signal with high frequency triangular carrier wave as

shown in Figure 2.15. When the value of sinusoidal signals exceeds that of triangular wave, then the inverter switch is turned on, and when it is less, the switch is turned off [58].

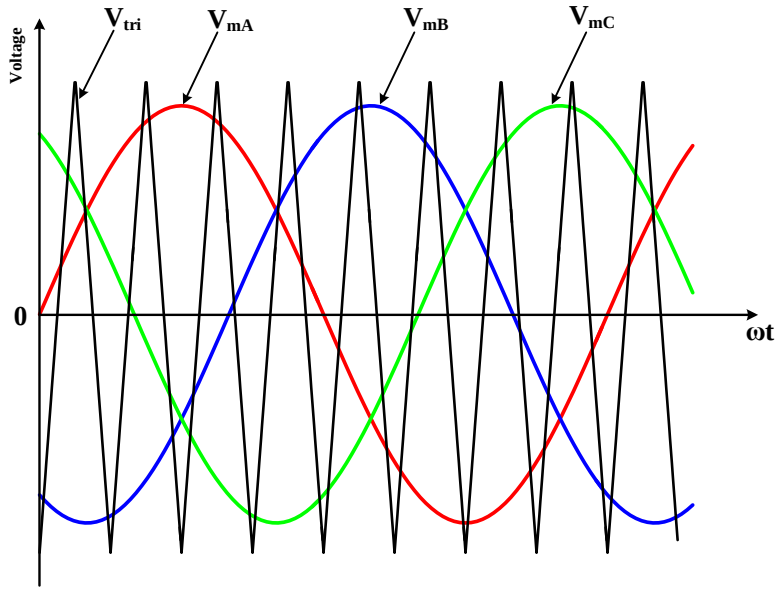

Figure 2.15: Sinusoidal pulse-width modulation control technique

The sinusoidal modulating signals of 60 Hz frequency, phase angle equal to output of P-controller (Ang) with additional shifting of -2.0944 and 2.0944 radians (-120 and 120 degrees), and magnitude equal to output of Q-controller (Mag), were generated using sine wave generator as shown in Figure 2.16.

To generate PWM switching pulses, a high frequency triangular wave (V_{tri}) was compared with three sinusoidal modulating signals. In real-time simulation, all the control circuits were simulated in large time-step. However, in order to get precise switching instants, triangular wave was generated in small time-step simulations.

A high resolution triangular wave was produced in small time-step using triangle wave generator, which was designed to get inputs from large time-step control circuits. The control circuit shown in Figure 2.17 was used to generate support signals, triangle wave's phase (TANGLEAC) in radians, and rate of change of phase (TOMEGAAC) in radians per second. The frequency of triangle wave (3 kHz) is multiplication of frequency modulation

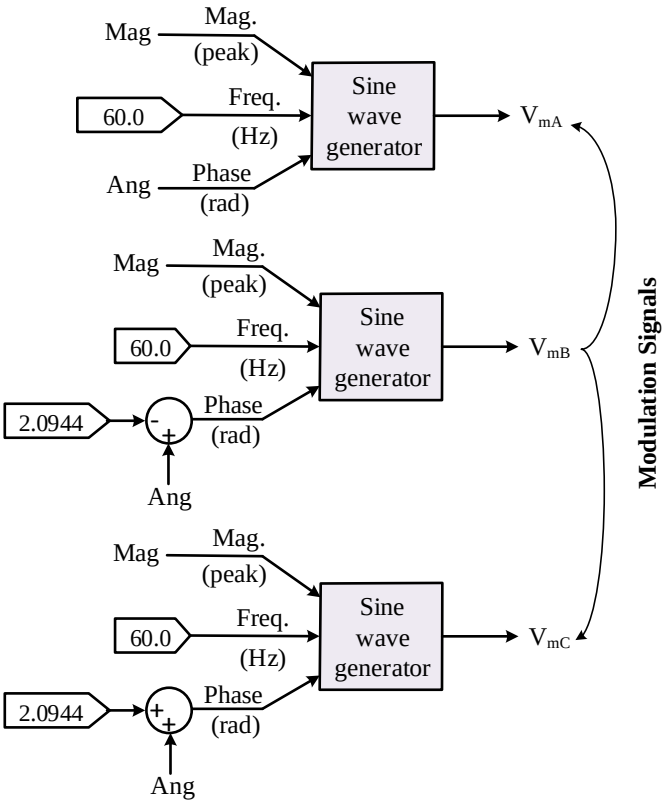

Figure 2.16: Modulation waveform generator

factor (50) and fundamental frequency (60 Hz). The phase angle of fundamental signal was multiplied by frequency modulation factor, and maintained between 0 and 2π to obtain phase signal for triangle wave. A small time-step triangle wave generator shown in Figure 2.18 uses the phase and frequency information generated from large time-step control circuit of Figure 2.17 to produce high resolution triangle wave as discussed in [37].

The final stage of firing pulse generation was comparison between three sinusoidal modulating signals, and high resolution triangle wave obtained from triangle wave generator. The comparison was done in small time-step simulation using firing pulse generator as shown in Figure 2.18. The output of firing pulse generator (firing pulse word) was obtained from three comparators by setting output equals to 1 when modulation signal was greater than triangle wave, and 0 otherwise. In RTDS, inverters were designed in such a way that each IGBT switch was controlled by different bit of a firing pulse word. Hence, by implementing

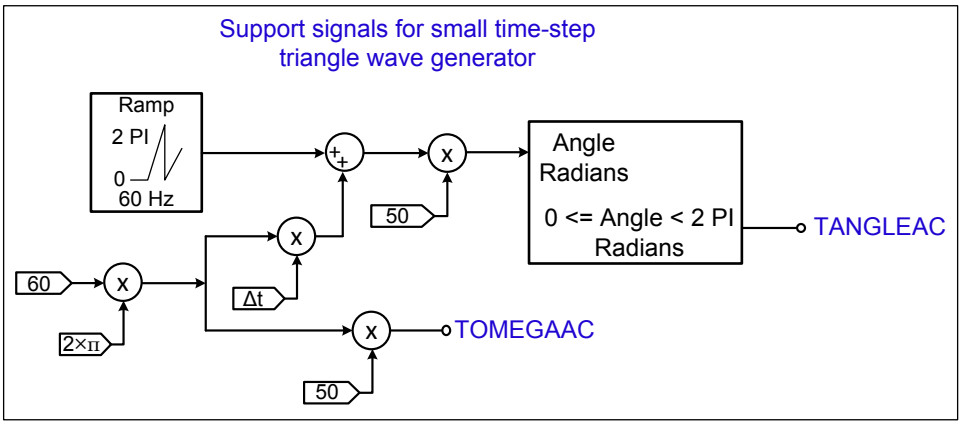

Figure 2.17: Generation of support signals for small time-step triangle wave generator

voltage control and SPWM technique, grid integrated VSI can convert DC power produced from solar PV to AC power, and can be transferred to distribution network.

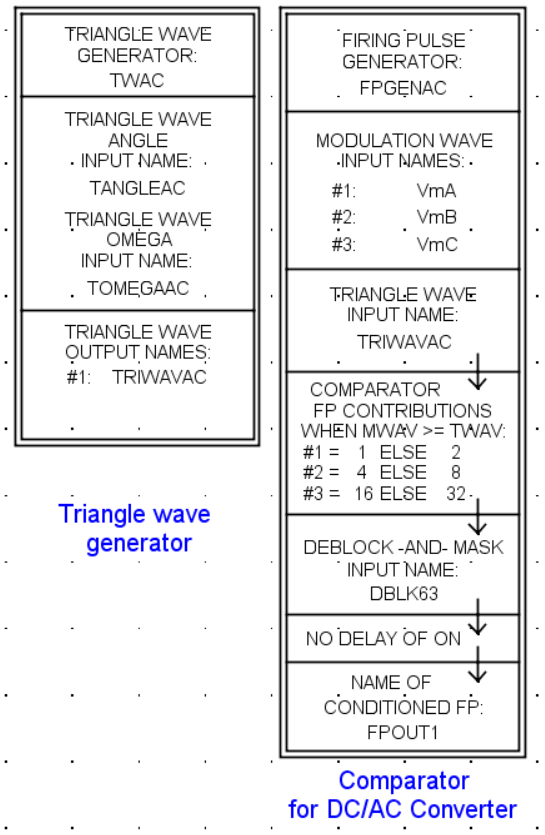

Figure 2.18: Small time-step triangle wave and firing pulse generators

A switching frequency of 3 kHz was considered for VSI to avoid excessive losses due to high frequency switching. The parameters of 500 kW central inverter are given in Appendix A.4.

2.4.4 DC Link Capacitor

The main purpose of DC-link capacitor is to maintain constant DC voltage, and to reduce the ripple in DC-link voltage within the permissible limit. The minimum DC link voltage is related to the output line-line voltage of inverter, which is determined by following equation [56]:

$$V_{dc} \geq \frac{2\sqrt{2}}{\sqrt{3}} V_{L-L}, \tag{2.13}$$

where V_{dc} is DC link voltage, and V_{L-L} is line to line voltage at PCC.

The size of DC-link capacitor was computed using following expression [63]

$$\begin{aligned} C_{dc} &= \frac{2 \times P_{max} \times 16.7 \times 10^{-3}}{V_{dc}^2(1-k^2)} \\ k &= \frac{V_{dc,min}}{V_{dc}} \end{aligned} \tag{2.14}$$

where P_{max} is the maximum power output, $V_{dc,min}$ is minimum allowable DC-link voltage, and 16.7×10^{-3} is the time corresponding to one cycle at power frequency of 60 Hz.

2.4.5 AC Harmonics Filter

The output currents and voltages from grid-connected inverter contains harmonic distortion due to high frequency switching in the inverter. The harmonic filter shown in figure 2.19, consisting of series reactor (L_f), and shunt high-pass filter with capacitor (C_f), inductor (L_{hf}), and damping resistor (R_{hf}) [64], was designed, and implemented to limit the current and voltage harmonics as recommended in IEEE standard 519 [65].

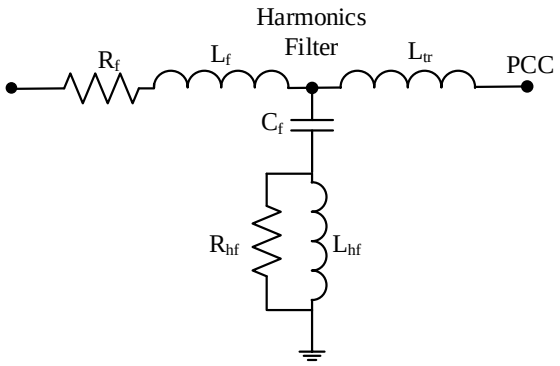

Figure 2.19: AC Harmonics filter

The size of reactor (L_f) was selected using the following expression:

$$L_f = \frac{1}{8}\frac{V_{dc}}{\Delta I_L f_{sw}}, \tag{2.15}$$

where ΔI_L is inductor ripple current, which is assumed to be 20% of rated current, and f_{sw} is switching frequency of the inverter.

The parameters of high-pass filter were designed using following steps [**?**]

- The impedance of capacitor can be arbitrarily chosen as 10 p.u at 60 Hz so that shunt branch acts as an open circuit at nominal frequency (f_n) of 60 Hz. Suppose, the base impedance at low voltage side of transformer is $Z_{base_{LV}}$, and at nominal frequency of 60 Hz, the impedance of capacitor is Z_{cap}. Then, the value of filter capacitance is given by

$$C_f = \frac{1}{2\pi \times 60 \times Z_{cap}} \tag{2.16}$$

- The value of inductor can be selected, neglecting series resistance, such that a resonance occurs at inverter switching frequency of 3 kHz. Therefore, from equation of the resonant frequency of a series LC circuit,

$$L_{hf} = \frac{1}{\omega_r^2 \times C_f} \tag{2.17}$$

where $\omega_r = 3$ kHz is resonant frequency.

- The value of series damping resistor was obtained such that the impedance of parallel connected inductor at switching frequency is equal to the value of resistance.

$$R_{hf} = \omega_r \times L_{hf} \tag{2.18}$$

The leakage inductance (L_{tr}) of step-up transformer is also considered as part of LCL filter. Hence, a resonance frequency (f_{res}) of harmonic filter designed above is given by [66]:

$$f_{res} = \frac{1}{2\pi}\sqrt{\frac{L_f + L_{tr}}{L_f L_{tr} C_f}} \tag{2.19}$$

which also satisfies the condition, $10f_n \leq f_{res} \leq 0.5f_{sw}$. The designed values of filter parameters are given in Appendix A.4.

2.4.6 Transformer Model

The 500 kVA, 210 V/20 kV, step-up, delta-grounded star, three-phase transformer was used to step up inverter output voltage to distribution voltage level. The utility transformer in grid-connected PV systems act as galvanic isolation between power electronic converters and the AC grid. In order to get high frequency behavior of grid connected PV systems, transformer is required to model in high frequency domain. The detailed transformer model with parasitic capacitance between windings, capacitance between phases, and capacitance between phase to grounding were discussed in [67–69]. In RTDS, a simplified linear transformer model with parasitic capacitance was modeled to simulate high frequency behavior as shown in Figure 2.20. The capacitance C_{LG}, C_{HG}, C_{HL} are parasitic capacitance between low voltage terminal to ground, high voltage terminal to ground, and high voltage to low voltage terminals, respectively. The electrical parameters and parasitic capacitance of step-up transformer used in simulations are tabulated in Appendix A.5.

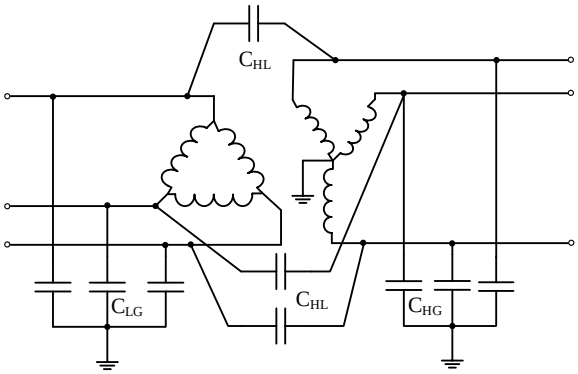

Figure 2.20: Parasitic capacitance of three-phase transformer

2.4.7 Dynamic Load Model

It is shown in Figure 2.5 that three-phase, 100 kW load was connected at low voltage side of transformer. A dynamic load model was simulated in RTDS to adjust active and reactive power of load dynamically. The series RL type load was used to represent the dynamic load model as explained in [37].

2.4.8 Grid Model

A grid system was represented as an equivalent voltage source (20 kV and 60 Hz) behind the inductive impedance as shown in Figure 2.5. The PV system was connected to infinite bus where frequency and voltage were constant. The grid voltage was taken as reference voltage throughout the system simulation. The grid system and load parameters used for simulation are given in Appendix A.6.

2.4.9 Cable Model

Classical lumped parameter cable model is not capable to represent transient behavior of the system for different frequencies. This is because resistance and inductance of the cable are frequency dependent due to skin and proximity effects. When frequency of the signal increases, the resistance value increases due to the skin effect. Furthermore, inductance of

the cable decrease with increase in frequency as shown in Table 2.1 due to reduction of flux-linkage inside the conductor. For different frequencies, the value of resistance, inductance, and capacitance of 30 m long 1,000 V power cable used in this research are given in the table.

Table 2.1: 30 m, 1000 V cable parameters

Freqency (Hz)	Resistance ($m\Omega$)	Inductance (μH)	Capacitance (nF)
60	10.83	114.05	4.40
1 k	114.61	54.64	4.40
3 k	173.56	46.89	4.40
20 k	202.37	44.16	4.40
100 k	284.82	44.08	4.40

The limitations of lumped cable model has been minimized with various frequency dependent traveling wave-based cable models developed in the literature [70–72]. The frequency dependent ("Modal") cable model [71] and frequency dependent ("phase") cable model [70, 72] are widely used distributed parameter models in EMT simulations. The traveling wave-based frequency dependent cable model requires simulation time-step lower than propagation time of traveling wave in the cable. The travel time (τ) of cable is related to cable length (l) by relation

$$\tau = \frac{l}{\nu} \tag{2.20}$$

where traveling wave velocity (ν) is equal to be 3×10^8 m/s. The cables used in PV systems were very short in length between 30 and 200 meters. As an example for 30 m cable, travel time was calculated as 0.1 μs. Therefore, to simulate frequency dependent modal or phase cable model, the simulation time-step should be less than 0.1 μs. However, in real-time simulation platform, the simulation hardware has not been designed, which can simulate with time-step less than 1.4 μs. Because of aforementioned limitations, frequency dependent π cable model in RTDS was employed, which was simply enhanced lumped π model with frequency dependent resistance and inductance. The detailed modeling of frequency dependent π cable model is discussed in next sub-section.

2.4.9.1 Frequency Dependent Π Cable Model

A frequency dependent π cable model was used to simulate short cables in high frequency transient simulation. The "enhanced pi" cable model proposed in [73], and frequency dependent π cable model discussed in [37] were the available frequency dependent models for the short transmission lines and cables. In this research, frequency dependent π cable model as shown in Figure 2.21 was modeled and EMT simulation was done in small time-steps.

The configuration of each π section consists of shunt RC branches, frequency dependent resistance, frequency dependent inductance, and fixed inductance part as shown in Figure 2.21. It is obvious from Figure 2.21 that the frequency dependent resistance network is a ladder network of parallel resistance and series inductance; whereas the frequency dependent inductance circuit is a ladder circuit of shunt inductance and series resistance. The characteristics of each part are discussed below:

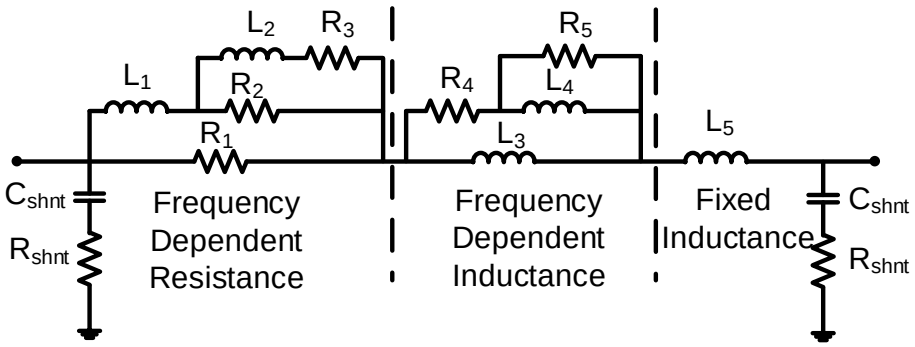

Figure 2.21: Configuration of frequency dependent π model

(a) Frequency Dependent Resistance:

The impedance of frequency dependent resistance ($Z_R(\omega)$) is given by the following

equation:

$$Z_R(\omega) = \cfrac{R_1}{1 + \cfrac{\cfrac{R_1}{j\omega L_1}}{1 + \cfrac{\cfrac{R_2}{j\omega L_1}}{1 + \cfrac{\cfrac{R_2}{j\omega L_2}}{1 + \cfrac{R_3}{j\omega L_2}}}}} \tag{2.21}$$

From the above equation, at very low frequency ($\omega \approx 0$), the impedance of frequency dependent resistance is equal to the parallel connection of R_1, R_2, and R_3. But, at very high frequency, the effective impedance will be only R_1. The typical impedance magnitude plot of frequency dependent resistance as a function of frequency is shown in Figure 2.22.

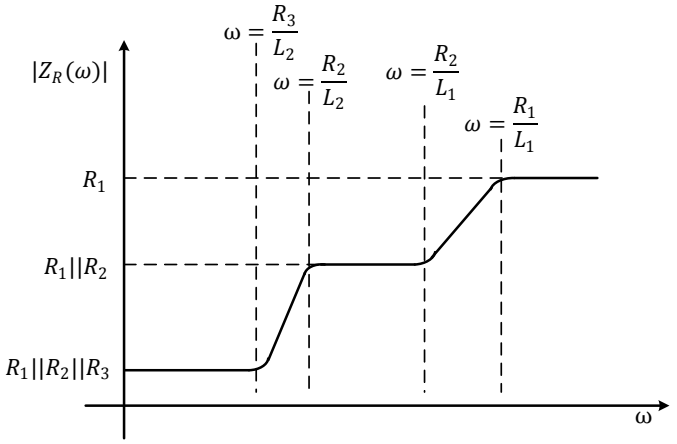

Figure 2.22: Impedance magnitude plot of frequency dependent resistance

The resistance values R_1, R_2, and R_3 are first determined to specify three resistance levels, and then inductance values L_1 and L_2 are calculated with different transition frequencies as shown in Figure 2.22. In order to get the proper sequence of transition frequencies, following inequalities should be satisfied: $R_1 > R_2 > R_3$ and $L_1 > L_2$.

(b) Frequency Dependent Inductance:

The impedance of frequency dependent inductance ($Z_L(\omega)$) is given by the equation below:

$$Z_L(\omega) = \cfrac{j\omega L_3}{1 + \cfrac{\cfrac{j\omega L_3}{R_4}}{1 + \cfrac{\cfrac{j\omega L_4}{R_4}}{1 + \cfrac{j\omega L_4}{R_5}}}} \tag{2.22}$$

It can be seen from Equation 2.22, at the frequency near to DC ($\omega \approx 0$), the impedance of frequency dependent inductance is equal to jωL_3. When the frequency increases, the impedance will drop to jωL_3//jωL_4 and eventually to $R_4//R_5$ at very high frequency.

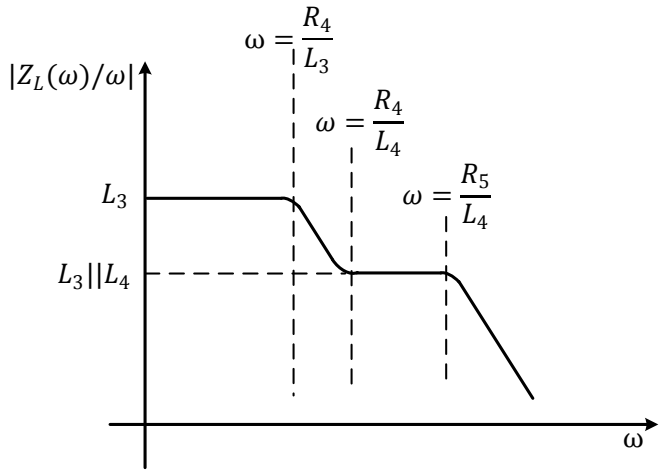

Figure 2.23: Impedance plot of frequency dependent inductance

The impedance magnitude plot of frequency dependent inductance as a function of frequency shown in Figure 2.23 demonstrates that after selecting inductance values L_3 and L_4, the resistance values R_4 and R_5 are obtained from transition frequencies. By satisfying inequalities, $R_4 < R_5$ and $L_3 > L_4$, proper transition frequencies can be obtained.

The frequency dependent π cable model parameters of 30 m (section of cable 1) and 100 m (section of cable 3) long cables are obtained using steps discussed in Appendix B.2, and

the parameters are given in Appendix B.3. The physical parameters of cables used in the test system are also given in Appendix B.1. The simulation results presented in Appendix B.2 show that frequency dependent π cable model can be convincingly used to study the transient behavior of the system.

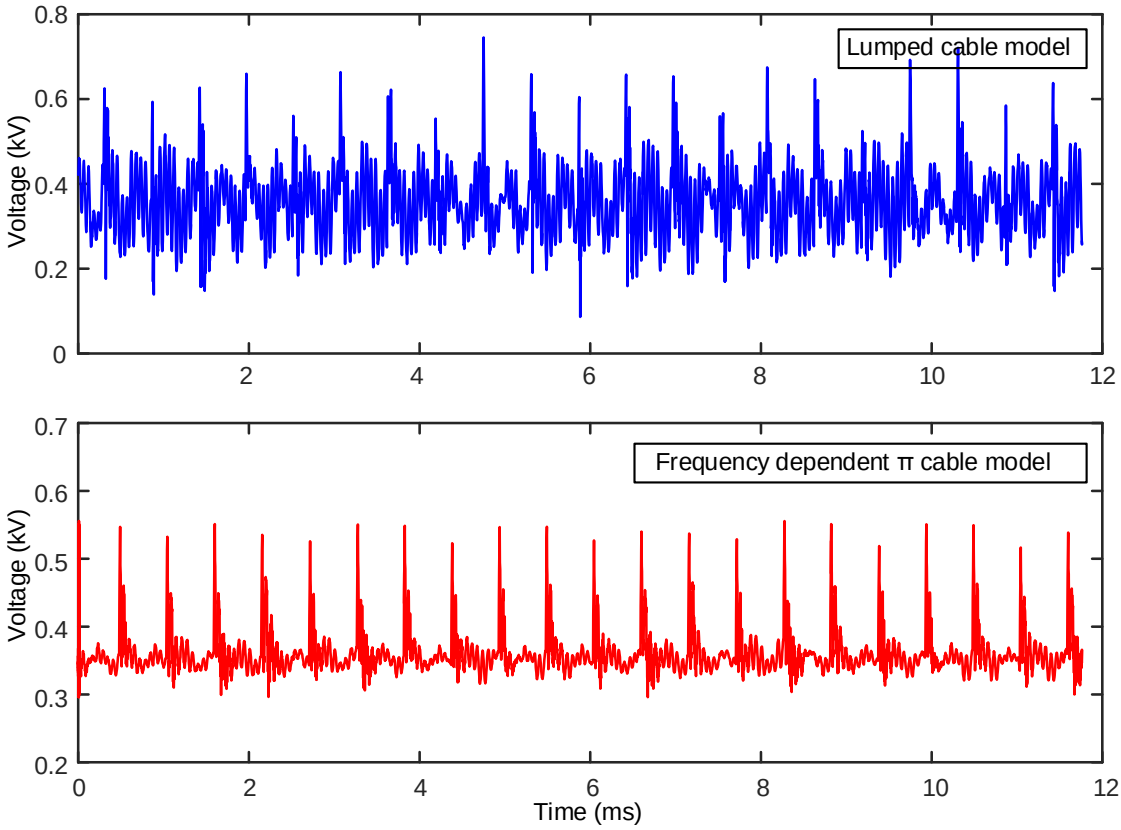

Figure 2.24: DC-DC converter mid-point voltage with different cable model

The given test system was simulated with different cable models, and results with the lumped cable model at 60 Hz and the frequency dependent π cable model are shown in Figure 2.24. The mid-point voltage of DC-DC converter 1 in Figure 2.5 was measured when ground fault occurs at negative conductor of the converter 1. Figure 2.24 shows the dominant frequency, amplitude, and damping of oscillations obtained with the two cable models and the differences in the results obtained.

2.5 Summary

In this chapter, multi-string grid-integrated 500 kWp PV system was modeled with RTDS. The operating principles, mathematical models, and control algorithms of PV test system were described. The MPPT control algorithm, which operates the PV array for maximum efficiency was discussed. Furthermore, a simple P-Q inverter control method to maintain constant DC-link voltage, and to control the active and reactive power flow through inverter to grid was explained. The switching frequencies of DC-DC converters and inverter were considered as 1.8 and 3 kHz, respectively. The frequency dependent modeling of short cable (around 30-100 m) was demonstrated using frequency dependent π cable model. The simulation results presented show that frequency dependent π cable model gives better simulation results than lumped cable model, in terms of dominant frequency and damping of oscillations.

Chapter 3

Pattern Recognition-based Fault Location Method

3.1 Introduction

In an ungrounded PV system, the converters switching transients interacting with parasitic elements of cables and PV panels generate high frequency noise patterns. These patterns are unique for each fault at various locations in the system. Hence, a noise pattern analysis-based algorithm is utilized in this thesis for fault location.

In this chapter, the performance of currently available fault locating methods using traveling waves is explained, and the practical difficulties of implementing the scheme for typically short length underground cables in a PV system is discussed. The proposed pattern recognition approach using wavelet transforms, which can detect faults accurately in ungrounded solar PV systems, is then explained. The DWT is used to extract the features for pattern recognition, and the role of an ANN as a fault locator is also discussed.

3.2 Traveling Wave (TW) Fault Location

As mentioned earlier, among the many fault location methods available, traveling wave fault locators are very efficient and have become more popular in AC transmission line and HVDC line protection systems [15, 17]. Traveling wave methods use the naturally occurring surges and waves generated by faults. The propagation time of the TWs to reach both terminals of the line are measured using a common time reference and the distance of the

fault from the line terminals is calculated. Recently, TW fault locators have been developed in industrial hardware that uses time-synchronized measurements of the TW currents at the line terminals to determine the accurate fault location. This fault locator is combined into transmission line protective relays and using standard CTs determines the location of a fault to within half a kilometer, or about one tower span in a transmission line [15, 19].

TW analysis of the faults in a 161 kV, 117.11 km long line in [15] demonstrated that the travel time of TWs is equal to 790.605 μs and that the method could locate faults with an accuracy of 300 m. However, the TW propagation time would be very small for the short length cables (around 200 m) used in solar PV farms, and in addition, the latency between the incident wave and its reflection might be so short that the TWs would be very hard to detect individually. Therefore, it would be difficult to use traveling wave theories for analysis of fault locations in solar PV systems. Also, it would be more costly to use GPS systems in both terminals of short cables. For these reasons, a wavelet MRA and ANN-based pattern recognition method is proposed to locate faults in ungrounded PV systems. In addition, previous work [17] advocates the practical implementation of waveform detectors that can capture transient signals using high speed analog-to-digital (A/D) converters that sample the current and voltage signals at a 1.56 MHz range. Thus, the high frequency noise signals found in an ungrounded PV system can be detected by monitoring at a MHz sampling rate using actual hardware and, hence, the proposed fault locator can be deployed in real world applications.

3.3 Pattern Recognition Algorithm

3.3.1 Noise Patterns and Fault Locations

The analysis of high frequency noise patterns to identify fault locations in ungrounded PV systems is proposed. These noise signal patterns are generated due to the power electronic converter switching frequencies and parasitic elements of PV panels and cables (such as cable insulation capacitance and stray inductance). The proposed location method requires

a distinguishable signal that uniquely identifies a fault position. The mid-point voltage of DC-DC converter 1 (V_{mid1}), with measurement point as indicated in Figure 2.5 , is monitored with two sample faults, respectively, occurring on positive (at Loc. #1) and negative (at Loc. #5) conductors. The simulation results shown in Figure 3.1 illustrate that the high frequency noise is accommodated in the measured voltage signal and different noise patterns are introduced due to ground faults at various locations of the PV system. Therefore, unique characteristics can be extracted from the noise in a suitable measurement signal and used in a classification algorithm to determine the exact fault location. Furthermore, it is noted that the mid-point voltage of DC-DC converter 1 or 2 results in a significant change in noise patterns for different ground fault locations. Hence, in the following sections, the V_{mid1} voltage signal is measured and analyzed. Thus, no external signal generator is required to locate the fault using the proposed method.

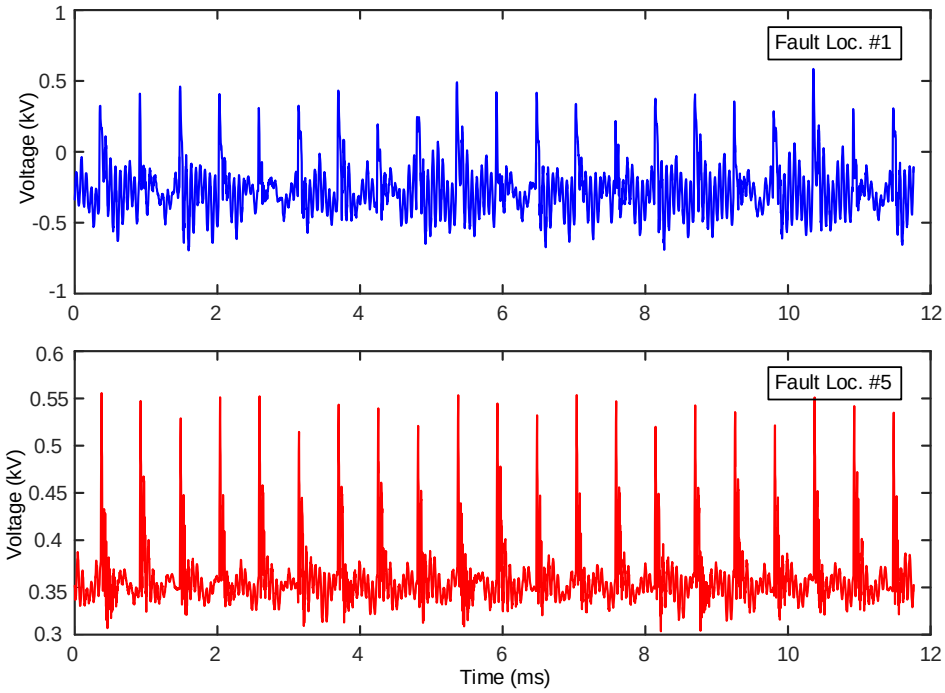

Figure 3.1: Noise signal during faults at Loc. #1 and Loc. #5

As stated earlier, the high frequency noise is generated by the oscillatory circuit that is established by the fault grounding point and the parasitic elements in the system. The simplified grid-connected PV system shown in Figure 3.2 is used to illustrate the oscillatory

circuits involved in a ground fault at a negative DC bus (point f). The oscillatory loops (red curve) shown in Figure 3.2 are related to the switching event of the inverter during the fault at point f. Each loop originates from the fault point and goes back to ground through PV modules and cable parasitic capacitance. For varying fault locations, oscillatory paths will be different and will generate varying noise patterns. These inherent noise patterns for different fault locations can be used for the signal analysis-based fault location method discussed in following section.

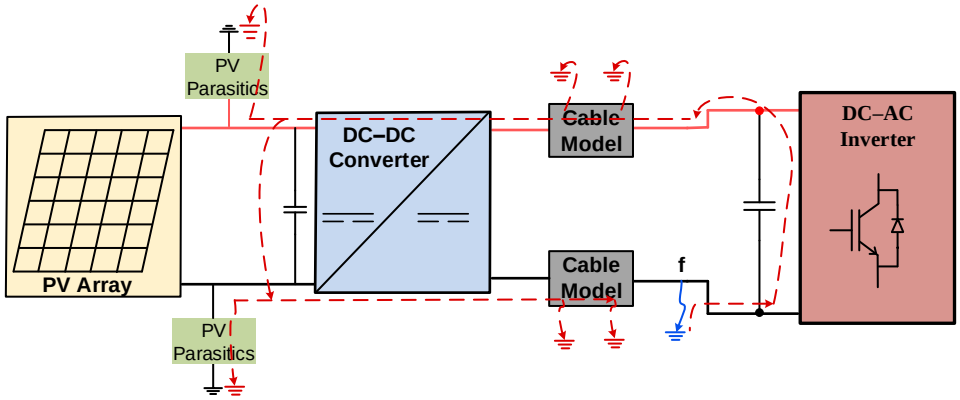

Figure 3.2: Oscillatory loops for a ground fault at a negative bus

3.3.2 Proposed Fault Location Algorithm

It has been investigated in the literature [32, 33] that the background noise caused by repetitive switching transients introduced by power electronic converters interacting with system parasitic elements can be analyzed to find the exact location of the ground fault in ungrounded DC shipboard power systems. The research in this thesis proposes the concept of noise pattern analysis of measured signals with wavelet transform (WT) and an artificial neural network (ANN) classification algorithm for real-time ground fault location in an ungrounded multi-string grid-connected PV system.

Figure 3.3 shows the flowchart of the proposed algorithm. As mentioned in Section 3.3.1, the mid-point voltage of DC-DC converter 1 (V_{mid1}) contains high frequency noise and provides different noise patterns for ground faults at different locations in the system.

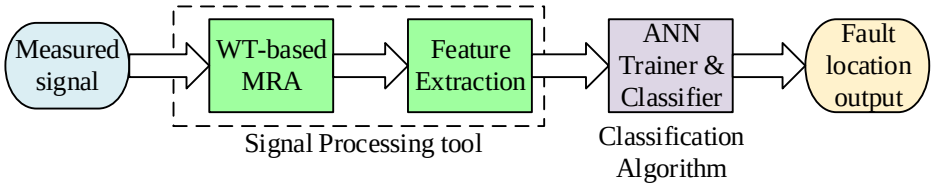

Figure 3.3: Flowchart of the proposed algorithm

Therefore, this voltage signal is measured and could be analyzed using WT-based MRA to implement the proposed algorithm. The measured time domain signal is transformed into a time-frequency domain by splitting it into low and high frequency components with a DWT-based MRA technique. The energy or norm of the noise signals at each frequency band gives a unique signature for different fault locations and is used as extracted features for pattern recognition. The extracted features are then used as inputs of a multi-layer neural network classification algorithm. The outputs of the ANN classifier give the exact location of the fault. Each component of the flowchart will be discussed in the following sections.

3.4 Signal Analysis

Different signal processing tools, such as fast Fourier transform (FFT), short time Fourier transom (STFT), and WT, can be used for analysis of the fault generated transient signals. The main objective of the signal analysis is to obtain time-frequency resolution of the transient signals and extract the unique characteristics for different fault locations.

3.4.1 Why Wavelets?

Conventional signal processing techniques such as discrete Fourier transform (DFT) or FFT are simple to implement in real systems but have some drawbacks. The frequency domain information of a signal computed by such methods is an average over the entire time duration of the signal. Thus, if there is a transient or spike in the signal, it will contribute to the Fourier transform (FT), but its location on the time axis will be lost [74]. That means

FFT gives the frequency components associated with the signal but will not indicate exactly when a particular event occurred. Therefore, non-stationary signals whose frequency varies with time will not be properly analyzed in terms of both frequency and time resolution using traditional Fourier transforms.

One way of solving the aforementioned problems is to implement windowed FFT or STFT. In STFT, the desired portion of the time window of the signal is selected for entire frequencies. However, the fixed window size limits the flexibility of time and frequency resolutions for analyzing transient signals. A wide window size results in good frequency but poor time resolution, whereas a narrow window size results in good time but poor frequency resolution. In [74], it is clearly shown that the frequency resolution increases and time resolution decreases as the size of the window increases. In order to obtain good time-frequency resolution, the STFT must be implemented a number of times with different window sizes.

However, wavelet analysis mitigates the shortcomings of the Fourier transform methods as it has capability to localize on both time and frequency. The non-stationary signals are decomposed into wide-band by applying a series of wavelet filters to detect high frequency components. Moreover, WT allows use of a flexible window size, which gives the appropriate time-frequency resolutions. This property enables wavelets to use short-time intervals for high-frequency components and long-time intervals for low frequency components, which helps to achieve better time-frequency analysis [74].

Over the past few decades, wavelet transform has been used in various research works in power systems. It has been proposed extensively for protective relaying, power quality analysis, HVDC systems monitoring, and fault detection and localization in generators, transformers, and transmission lines, etc. [28, 75–78]. Some of the papers in the literature explore the use of WT for pattern recognition-based fault detection, location, and classification in ungrounded DC shipboard distribution systems [32,34]. Furthermore, in recent years, the better performance of WT has been utilized for fault diagnosis in PV systems [79–81].

The voltage signals measured from PV systems are non-stationary signals due to switch-

ing transients of power electronic converters, as shown in Figure 3.4. That means the measured voltage is not periodic in nature and contains varying frequencies with time. Hence, in this research, the DWT was employed to achieve both time and frequency resolution of the high frequency noise containing signal. The WT-based MRA with wavelet filters is used to detect high frequency components in power systems due to converter switching transients. Then, to implement the fault localization method, the features are extracted using WT-based MRA, which will be discussed in the following sections.

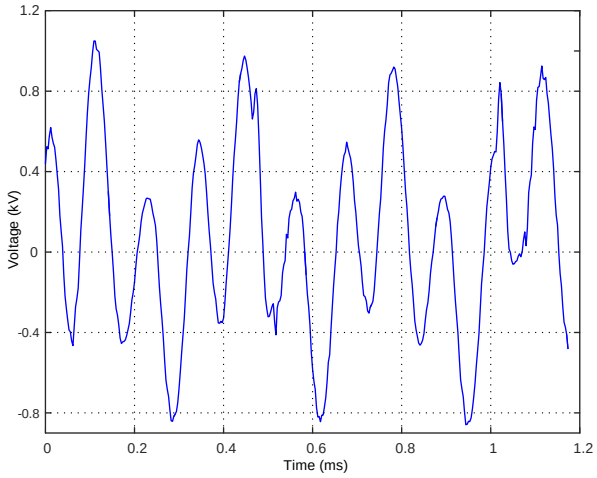

Figure 3.4: Zoomed mid-point voltage of DC-DC converter 1, an example of a non-stationary signal

3.4.2 Wavelet Transforms

As an alternative to STFT and to overcome limitations related to its time-frequency analysis properties, a linear transform is introduced, defined as the wavelet transform (WT). The WT is a powerful mathematical tool that decomposes a given signal into different frequency components and then analyzes individual components with desired time and frequency resolutions. In order to achieve good time-frequency resolutions, it must have a varying window function whose size increase in time during analysis of the low frequency content and decrease in time while dealing with the high frequency component of the signal. These requirements are fulfilled with the development of wavelet functions $\Psi(t)$, so called "mother wavelets". Mathematically, the continuous wavelet transform (CWT) of a time

domain signal $f(t)$ with respect to some mother wavelet function $\Psi(t)$ is defined as:

$$CWT_{\Psi}^{f}(u,s) = \int_{-\infty}^{\infty} f(t)\overline{\Psi_{u,s}(t)}dt \tag{3.1}$$

The bar symbol denotes the complex conjugate. The function $\Psi_{u,s}(t)$ is scaled or dilated and a translated version of mother wavelet function $\Psi(t)$ is given by:

$$\Psi_{u,s}(t) = \frac{1}{\sqrt{s}}\Psi\left(\frac{t-u}{s}\right); \qquad s > 0. \tag{3.2}$$

where 's' is the dilation (expansion or compression) or scale factor and 'u' is the translation (shifting) factor, and both variables are continuous in time. The normalization factor $\frac{1}{\sqrt{s}}$ is included so that the energy of the scaled wavelets, $\Psi_{u,s}(t)$, remains the same as the energy of the mother wavelet function, $\Psi(t)$. The continuous wavelet transform coefficients, $CWT_{\Psi}^{f}(u,s)$, measure the similarity between the original signal, $f(t)$, and a set of scaled wavelet functions, $\Psi_{u,s}(t)$ [75].

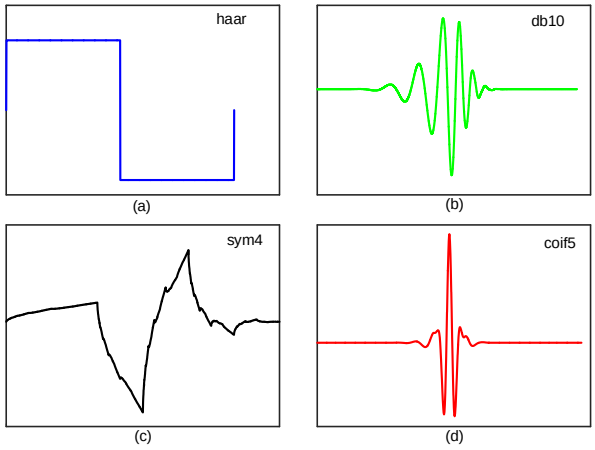

Figure 3.5: Different mother wavelets: (a) Harr, (b) Daubechies, (c) Symmlet, (d) Coiflet

The mother wavelet $\Psi(t)$ is a basic prototype function that acts as a variable windowing function with dilation and translation. Wavelets are small waves, oscillatory in nature and that decay very sharply resulting in a zero average value. In the literature, a number of mother wavelets are presented that can be used in real applications. There are several types of commonly used mother wavelets, such as Meyer, Haar, Symmlet, Daubechies, Morlet,

Coiflets, etc. The patterns of some wavelets are shown in Figure 3.5. In addition, the number of wavelet families, known as daughter wavelets, can be produced from a single base wavelet function by changing dilation and translation parameters.

The implementation of WTs in real engineering field applications would require a digital form of the CWT, which is referred to as a discrete wavelet transform (DWT). This is easy to implement in a real time application with digital computers. Consider the input signal $f(t)$ that is discretized where integer variable n refers to the sample number of a discrete series. In order to obtain a discrete version of the CWT, the scaling parameter (s) and translation parameter (u) are discretized with $s = a^j$ and $u = ku_o a^j$. Then, the DWT of sampled input sequence, $f(n)$, can be defined as

$$DWT_{\Psi}^{f}(j,k) = \frac{1}{\sqrt{a^j}} \sum_{n=-\infty}^{\infty} f(n)\Psi\left(\frac{n - ku_o a^j}{a^j}\right) \tag{3.3}$$

where k, j, a, and u_o are integer numbers with $a > 1$ and $u_o \neq 0$. By re-arranging Equation 3.3, the coefficient $DWT_{\Psi}^{f}(j,k)$ can be written as

$$DWT_{\Psi}^{f}(j,k) = \frac{1}{\sqrt{a^j}} \sum_{n=-\infty}^{\infty} f(n)\Psi\left(na^{-j} - ku_o\right) \tag{3.4}$$

Equation 3.4 can be compared with the convolution output $y(n)$ for the finite impulse response(FIR) digital filters

$$y(n) = \frac{1}{\sqrt{c}} \sum_{n=-\infty}^{\infty} f(n)h\left(k - n\right) \tag{3.5}$$

This shows that $\Psi(na^{-j} - ku_o)$ is the impulse response of a digital filter with transfer function $\Psi(\omega)$ [82]. Thus, by choosing appropriate values of scales and translations, a family of orthogonal wavelets can be generated. The popular way of doing this is to select $a = 2$ and $u_o = 1$ by which a dyadic wavelet transform is generated. Using this method, the DWT of Equation 3.4 can be realized by using multistage filter banks, commonly known as MRA.

3.4.3 Multi-resolution Analysis

The MRA introduced by Stephane G. Mallat [83] is a signal decomposition procedure that divides the signal into a set of frequency bands using a series of low-pass and high-pass filters. In other words, MRA decomposes the signal into low frequency approximation and high frequency details. The time domain signal $f(t)$ can be represented in terms of scaling, $\Phi(t)$, and wavelet, $\Psi(t)$, functions as given by [83–85]

$$f(t) = \sum_{k=-\infty}^{\infty} a_N(k)\Phi_{N,k}(t) + \sum_{j=1}^{N}\sum_{k=-\infty}^{\infty} d_j(k)\Psi_{j,t}(t) \tag{3.6}$$

The MRA can be used to convert the time domain signal into the wavelet domain by representing it at various resolution levels in terms of the following expansion coefficients A_{signal} [28],

$$A_{signal} = [a_N|d_1|d_2|.....d_N|] \tag{3.7}$$

where d_j is the detailed coefficient at various resolution levels and a_N is the last approximation coefficient at resolution level N.

The approximation coefficients can obtained by inner products of $f(t)$ with a scaling basis and, the detail coefficients can be calculated by inner products of the signal with a wavelet basis, as given below:

$$a_N(k) = \langle\ f(t), \Phi_{j,k}(t)\rangle = \int_{-\infty}^{\infty} f(t)\Phi_{j,k}(t)dt \tag{3.8}$$

$$d_j(k) = \langle\ f(t), \Psi_{j,k}(t)\rangle = \int_{-\infty}^{\infty} f(t)\Psi_{j,k}(t)dt \tag{3.9}$$

where the recursive scaling function $\Phi_{j,k}(t)$ and wavelet function $\Psi_{j,k}(t)$ can be computed as:

$$\Phi_{j,k}(t) = \sum_{n} h_0(n)\sqrt{2}\Phi(2t-n), \qquad n \in \mathbb{Z}, \tag{3.10}$$

$$\Psi_{j,k}(t) = \sum_{n} h_1(n)\sqrt{2}\Phi(2t-n), \qquad n \in \mathbb{Z} \tag{3.11}$$

Also, if 2^j is scaling and $2^j k$ is translation of t for a particular mother wavelet $\Psi(t)$, we will get

$$\Phi_{j,k}(t) = 2^{-j/2}\,\Phi(2^{-j}t - k) \tag{3.12}$$

$$\Psi_{j,k}(t) = 2^{-j/2}\,\Psi(2^{-j}t - k) \tag{3.13}$$

In addition, the high-pass filter $h_1(n)$ and low-pass filter $h_0(n)$ are quadrature mirror filters and associated with each other according to the following relation [84]:

$$h_1[n] = (-1)^n h_0[L - 1 - n] \tag{3.14}$$

where L is the filter length (even number only) and modulation by $(-1)^n$ transforms the low-pass filter into a high-pass filter.

Thus, to analyze a discrete signal with WT-based MRA, two digital filters can be implemented: one high-pass filter, $h_1[n]$, associated with a mother wavelet $\Psi(t)$, and its low-pass mirror version, $h_0[n]$, related to the scaling function $\Phi(t)$. A schematic diagram of MRA of a signal using discrete wavelet filters is provided in Figure 3.6, where three levels of decomposition are carried out and where $f[n]$ is the sampled signal of $f(t)$. The discrete input signal is decomposed to different frequency bands, passing through a high-pass filter $h_1[n]$ and low-pass filter $h_0[n]$, and then the outputs of filters are down-sampled by 2. The high frequency components, called detail coefficients (d_j), have high frequency and low time resolution whereas the low frequency components, known as approximation coefficients (a_j), provide low frequency and high time resolution.

Consider that the sampling frequency of an original input signal is F_s and $N = 1, 2, ...$ is the number of decomposition levels in MRA. Then, the frequency bands for different decomposition levels could be found by $\left[0, \frac{F_s}{2^{N+1}}\right]$ for a low-pass filter and $\left[\frac{F_s}{2^{N+1}}, \frac{F_s}{2^N}\right]$ for a high-pass filter. The input signal from a 340 kHz sampling frequency is decomposed into three levels; frequency bands for each decomposition level are shown in Figure 3.6. In this research, WT-based MRA is used to extract the unique features of the signals. The detailed coefficients from MRA provide different characteristics for the fault at different locations of

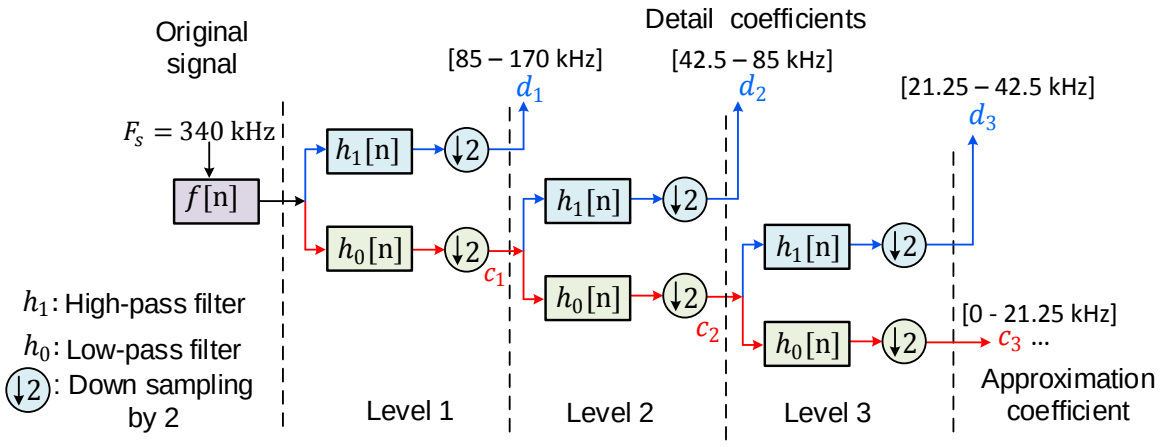

Figure 3.6: Multi-resolution analysis using DWT

the PV system (which will be discussed more in Section 3.4.6).

3.4.4 Choice of Mother Wavelet

The mother wavelet and the number of decomposition levels are two very important factors of WT-based MRA. The feature extraction, accuracy, and processing time performance of the proposed fault location algorithm mainly depend on the type of mother wavelet involved. Hence, it is very important to carefully choose the appropriate wavelet function to get accurate results from wavelet analysis. The choice of wavelet may vary with the various applications because different types of signals may require different mother wavelets in order to perform effectively.

The criteria for selecting a proper mother wavelet is discussed in [28]. As described in this paper, the selected mother wavelet function should have enough vanishing moments in order to represent the salient features of the transient signals. In addition, this wavelet should provide a sharp cut-off frequency that will help to reduce the leakage energy at adjacent resolution levels. At the same time, the chosen wavelet must be orthonormal and close to the analyzed signal so that it provides a perfect reconstruction with few decomposition levels.

A number of orthogonal wavelet families are available in the literature as discussed in

Section 3.4.2, such as the Daubechies family (dbN), Coiflets family (coifN), and Symlets family (symN), etc., where N is the order of the wavelet function. An algorithm is presented in [86] to determine a suitable wavelet for power system fault transient analysis based on the minimum root mean square difference between the original and reconstructed signal. The simulation results in this paper show that, among various orthogonal mother wavelets, the Daubechies wavelet results in least root mean square error and is most adequate for power system transient studies. In fact, Daubechies wavelets are the most popular and widely used mother wavelets in a variety of power system applications because they are well suited for detecting low amplitude, short duration, fast decaying, and oscillating signals. Based on these analyses, Daubechies wavelets are selected as appropriate mother wavelets for feature extraction.

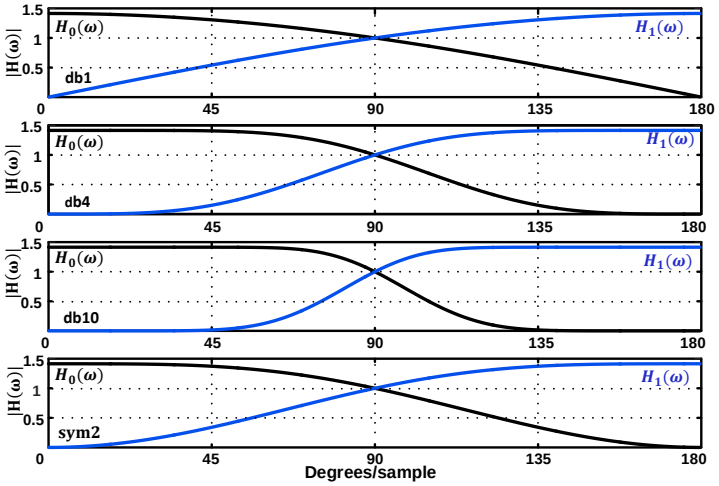

Figure 3.7: Frequency response of the different wavelet filters

The frequency response of high-pass filters (wavelet functions) and low-pass filters (scaling functions) of Daubechies (db1, db4, db10) and Symlet (sym2) mother wavelets are shown in Figure 3.7. Here, $H_1(\omega)$ and $H_o(\omega)$ represent the frequency response of high-pass and low-pass filters, respectively. It can be clearly shown from the frequency response plots that the db10 wavelet has a sharper cut-off frequency compared to the others. Thus, the leakage energy would be reduced between different resolution levels and more useful characteristics of the analyzed signal will remain after WT-based MRA decomposition.

Furthermore, Figure 3.8 shows the energy spectrum diagram of the measured signal, V_{mid1} (refer to Figure 2.5 during the fault at Loc. #6). Using db1, the energy of the measured signal is distributed over different resolution levels (in Figure 3.8 (a)) because of the wide cut-off frequency of the filters shown in Figure 3.7. In contrast, with db10 the energy is more concentrated at the 4^{th} resolution level and a very small part of the signal energy is leaked to neighboring resolution levels. Hence, from the above analysis, the db10 wavelet is selected for WT-based MRA to extract the unique features.

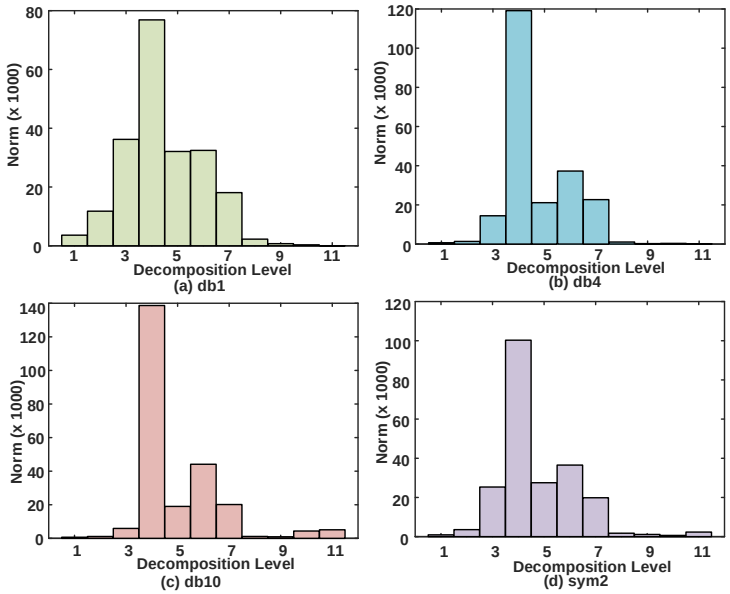

Figure 3.8: Energy spectrum for different types of wavelet functions

3.4.5 Selection of Decomposition Level

Using a higher decomposition level is preferable in order not to miss the salient features. However, as the decomposition level increases, the computational time becomes larger. Therefore, it becomes crucial to select an appropriate decomposition level that achieves a good balance between the number of candidate features and computing time.

In this thesis, the optimal number of decomposition levels is determined as presented in [87]. The suitable number of levels of decomposition (N_L) depends on the sampling frequency (F_s) of the signal being analyzed. It must be chosen in order to allow the high-

level signals (approximation and details) to cover the entire range of the frequencies. The minimum number of decomposition levels that is necessary for obtaining an approximation signal so that the upper limit of its associated frequency band is under the lowest frequency of interest (f), typically fundamental frequency, can be calculated as given below

$$2^{-(N_L+1)}F_s < f \tag{3.15}$$

Using this condition, the decomposition level of the approximation signal, the integer N_L, is defined as:

$$N_L = int\left(\frac{log(F_s/f)}{log(2)}\right) \tag{3.16}$$

After calculations and according to Equation 3.16, level 11 was chosen as the optimum decomposition level in this thesis. In addition, the frequency bands of different decomposition levels used in the proposed fault location algorithm are provided in Table 3.1. From the table, it is clear that the switching frequencies of the central inverter (3 kHz) and DC-DC converters (1.8 kHz) lie on decomposition levels 6 and 7, respectively. In fact, the noise signal is decomposed into 11 frequency bands to cover frequencies from 0.08 to 170 kHz, which will accommodate the resonant frequencies in the system.

Table 3.1: Frequency bands of different decomposition levels for cable fault analysis

Decomposition Level	**Frequency Band (Hz)**
1	85 - 170 k
2	42.5 - 85 k
3	21.25 - 42.5 k
4	10.625 - 21.25 k
5	5.3125 - 10.625 k
6	2.656 - 5.3125 k
7	1.328 - 2.656 k
8	664 - 1.328 k
9	332 - 664
10	166 - 332
11	83 - 166

Figure 3.9 illustrates the DWT-based MRA of the monitored signal, V_{mid1}, during a

ground fault at Loc. #1 (as shown in Figure 2.5). The detailed coefficients of the decomposed signals at different resolution levels describe the time of transients with different frequencies occurring in the analyzed signal. It is clear that the resolution levels D4 to D7 are more dominant with high amplitude, which represents the high frequency component of background noise and converter switching frequencies.

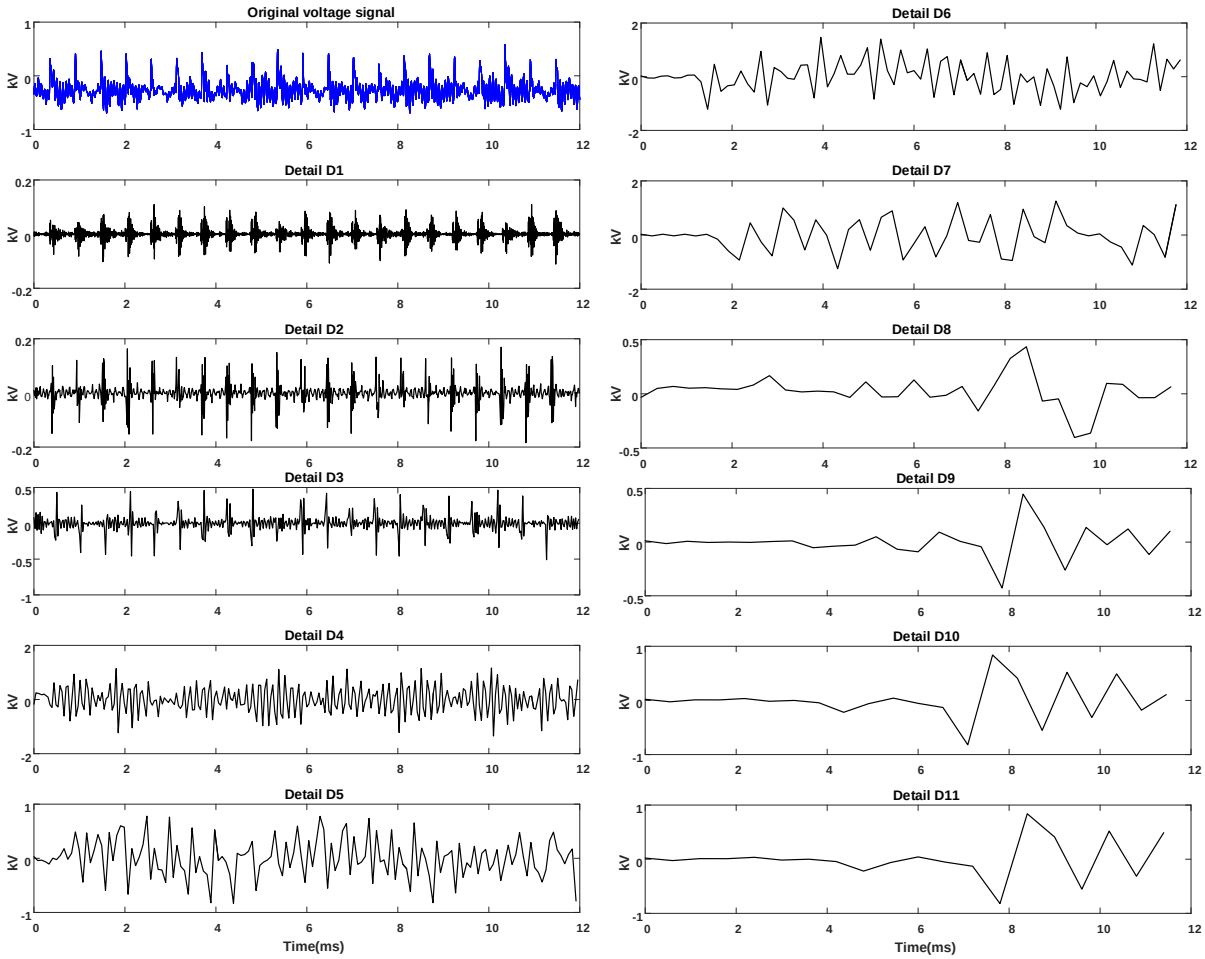

Figure 3.9: DWT-based MRA of the voltage signal, V_{mid1}, during a ground fault at Loc. # 1

3.4.6 Feature Extraction

After selecting the proper mother wavelet function and the optimum number of decomposition scales, the measured voltage signals are decomposed into different frequency bands

using WT-based MRA and the feature extraction process is implemented to obtain useful information from the transformed signal.

In pattern recognition problems, it is desirable to keep the dimension of the pattern representation at the classifier input as small as possible to obtain higher classification accuracy and lower computational load and time. Therefore, feature extraction methods are generally used to minimize the amount of information, either from the original signal or from its transformed data. Furthermore, the process of feature extraction consists of finding the unique waveform parameter, with significant information, that can represent the fundamental characteristics of the fault signal, referred to as features of the signal. In this work, the features are extracted from the detail coefficients at each frequency band, and can be used as inputs to the classifier.

If the scaling function and the wavelet functions have an orthonormal basis, then parseval's theorem relates the energy of the transient signal to the energy of the coefficients that represent the signal in the wavelet domain. Thus, the energy (W_{signal}) of the fault signal can be presented mathematically in terms of the expansion coefficient:

$$W_{signal} = \sum_{k=-\infty}^{\infty} |a_N(k)|^2 + \sum_{j=1}^{N} \sum_{k=-\infty}^{\infty} |d_j(k)|^2 \tag{3.17}$$

$$W_{signal} = W_{a_N} + \sum_{j=1}^{N} W_{d_j} \tag{3.18}$$

where

$$W_{a_N} = \langle a_N(k), a_N(k) \rangle = \|a_N(k)\|^2 \tag{3.19}$$

$$W_{d_j} = \langle d_j(k), d_j(k) \rangle = \|d_j(k)\|^2 \tag{3.20}$$

The second norm (referred to as the norm) of the detail coefficients $\|d_j(k)\|$, which were extracted at different frequency bands, is used as an input data vector for a classifier. This feature (norm) has been selected after the number of tests and comparisons between the performance of a neural network classifier with this feature and other features, such as

root mean square (RMS), standard deviation (STD), entropy, mean, and variance of each resolution level. A detailed comparison of classifier results with various features is presented in Chapter 4.

The norm of the decomposed signal is the square root of the sum of the square of the data vectors (detail coefficient) in each frequency band and is calculated as

$$norm_{d_j} = \|d_j\| = \sqrt{\sum_{i=1}^{n} |d_{ji}|^2} \tag{3.21}$$

where j represents level of decomposition and the maximum level is N, and d_j is the detail coefficients with n number of elements at level j. The proposed feature vector x can be mathematically represented as

$$x = \begin{bmatrix} x_1 \\ \vdots \\ x_j \\ \vdots \\ x_N \end{bmatrix} = \begin{bmatrix} \|d_1\| \\ \vdots \\ \|d_j\| \\ \vdots \\ \|d_N\| \end{bmatrix} \tag{3.22}$$

After the MRA decomposition of the monitored signal, the norm values are computed in each frequency band and the unique pattern used for the proposed fault location method. The bar diagram in Figure 3.10 represents the extracted feature (norm) at different resolution levels obtained from the MRA decomposition shown in Figure 3.9. The results clearly illustrate the energy at decomposition scales 3 to 7 dominates; this is due to the fact that these levels cover the high frequency component of background noise and switching frequencies of inverters (3 kHz) and buck converters (1.8 kHz). A detailed discussion of extracted features to distinguish fault locations in PV systems will be presented in Chapter 4.

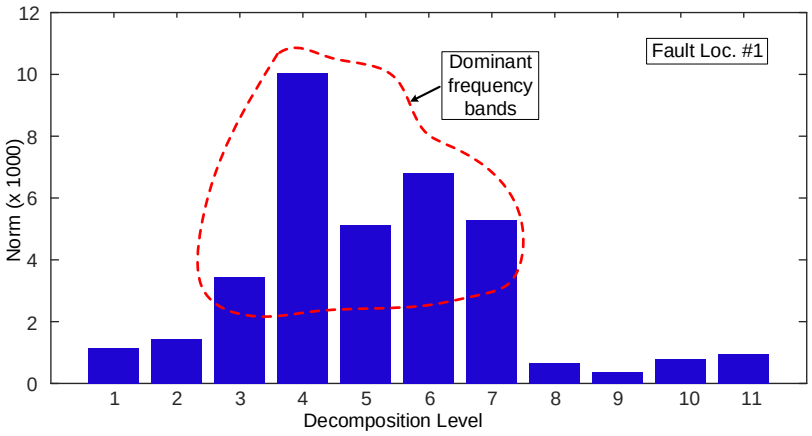

Level	Frequency Band (kHz)
1	85 - 170
2	42.5 - 85
3	21.25-42.5
4	10.63-21.25
5	5.32-10.63
6	2.66-5.32
7	1.33-2.66
8	0.66-1.33
9	0.33-0.66
10	0.17-0.33
11	0.083-0.17

Figure 3.10: Feature vector extracted during a ground fault at Loc. # 1

3.5 Classifier based on Artificial Neural Networks

The main purpose of the classifier element is to use the feature vector extracted from WT-based MRA to pinpoint the location of the fault in the system. In many real world problems, complete knowledge about the characteristic of the events and the systems cannot be obtained. Thus, the data measured can be used to learn the system behavior and implement machine learning algorithms to analyze power system transient events. There are many type of frequently used classifiers, such as ANNs, Bayesian classifiers, support vector machines, fuzzy-logic techniques, rule-based expert systems, etc. Among these classification algorithms, the ANN classification method is easy to implement in real time, accurate, and widely used in various aspects of power systems (fault location, power quality analysis, protective relaying applications, etc.). Thus, in this research, an ANN is employed as an intelligent classifier to find the fault location in PV systems. ANNs are highly effective for estimating the non-linear relationship between the input and output patterns even if the underlying signal models or the physical systems associated with the signals are largely unknown. It is able to adapt itself to the new state immediately, by re-training it, and can consider many characteristics of the input signals simultaneously to learn the correlations between them [88].

ANNs consist of many interconnected identical simple processing elements known as

neurons. The neurons operate in parallel and are connected together in structures that are closely modeled after biological neural systems. There are many types of ANN architectures and, among them, one of the most popular topologies is the feed-forward neural network. It does not contain any links between inputs and outputs. The structure and operational behavior of the feed-forward ANN is presented in the following section.

3.5.1 Feed-forward Neural Network

A multilayer feed-forward network, also referred to as multilayer perceptron (MLP), typically consists of an input layer, one or more hidden layers, and one output layer [89]. In this study, a three-layer feed-forward network, as shown in Figure 3.11, was adopted to realize an optimal fault locator. Each layer of an MLP contains several neurons that are connected by synaptic weights. In the proposed method, the number of neurons in the input layer (q) is the same size as the feature vector extracted from the WT-based MRA technique (i.e., q = 11). Similarly, the number of neurons in the output layer (m) is considered equal to the number of fault locations to be analyzed (in this thesis, m=14 for cable faults and m = 7 for panel faults). The outputs mathematically shown in Equation 3.23 indicate whether the monitored signal is under a normal condition or a fault condition at different locations [34]

$$\begin{aligned} \phi : R^q &\rightarrow \{0,1\}^m \\ \phi(x) &= (y_1, y_2, ..., y_i, ..., y_m) \end{aligned} \tag{3.23}$$

with

$$y_i = \begin{cases} 0 & \text{normal} \\ 1 & \text{fault} \end{cases}$$

where $i = 1, 2, ..., m$. The hidden layer is considered to have p number of neurons. The number of neurons in the hidden layer has been selected by trial and error with the goal of reaching better stability and a high convergence rate. After analysis with various neuron numbers, feed-forward networks with 18 hidden neurons were found to be sufficient for this fault location technique.

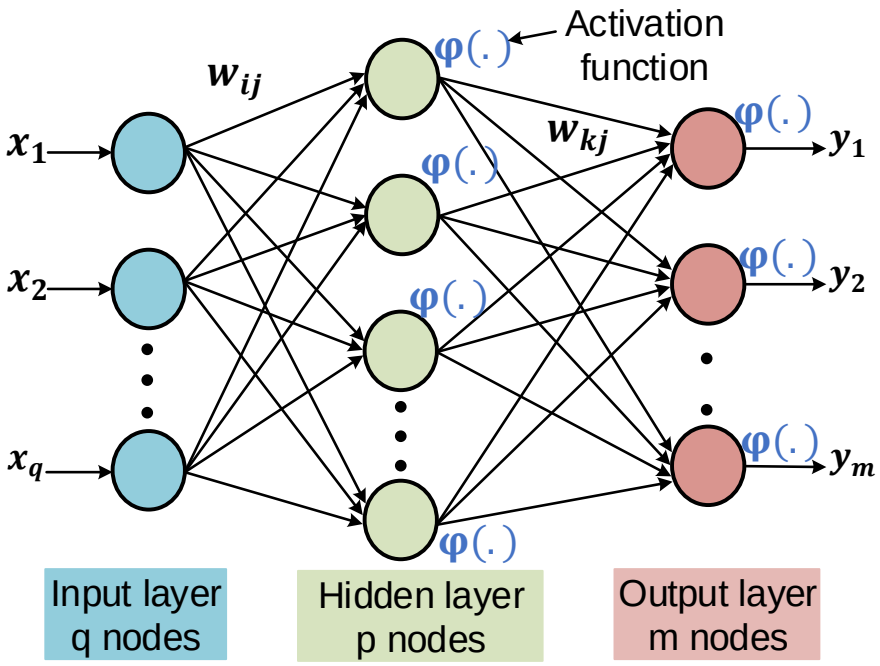

Figure 3.11: A three-layer feed-forward neural network

In the process of classification, each input signal is multiplied by the corresponding synaptic weight (w_{ij}) and the product is added with bias input, b_j. The total sum forms the input to the hidden neurons and is processed through a non-linear activation function $\varphi_j(.)$ of neuron j to obtain the outputs, $v_j(n)$, from each hidden neuron. Then, the output from neuron j from the hidden layer at time n can be obtained using

$$v_j(n) = \varphi_j(net_j(n)) \tag{3.24}$$

where the sum of weighted inputs at this neuron is given by

$$net_j(n) = \sum_{i=1}^{q} w_{ij}(n)x_i(n) + b_j \tag{3.25}$$

In a similar manner, the inputs of the output layer neurons are the outputs of the hidden layer nodes, and the output from neuron k of the output layer at time n is mathematically

expressed as

$$y_k(n) = \varphi_k(net_k(n)) \tag{3.26}$$

and the weighted sum at the input of neuron k of the output layer is calculated using

$$net_k(n) = \sum_{j=1}^{p} w_{kj}(n)v_j(n) \tag{3.27}$$

Nonlinear transfer functions, such as threshold, piecewise linear, log-sigmoid, and hyperbolic tangent [90, 91], are widely used activation functions in neural networks. A typical log-sigmoid transfer function is defined in Equation 3.28 and shown in Figure 3.12 (a). Here, the log-sigmoid function provides a continuous range of values from 0 to 1.

$$\varphi(x) = \frac{1}{1 + e^{-}x} \tag{3.28}$$

The second most popular activation function is a hyperbolic tangent or tan-sigmoid transfer function, which restricts the outputs between -1 and +1. The graphical representation of a tan-sigmoid function is shown in Figure 3.12 (b) and described by following equation:

$$\varphi(x) = tanh(x) = \frac{2}{1 + e^{-}2x} - 1 \tag{3.29}$$

In the proposed classifier design, the tan-sigmoid is used in the hidden layer and the log-sigmoid activation function is utilized in the output layer of the network.

3.5.2 Learning algorithm

As stated earlier, an ANN is capable of learning from the environment and can improve its performance through a continuous learning process. The neural network is trained to obtain a specific output for a particular input. The actual outputs, y_k, of the network are compared to the targets or desired outputs, t_k, and the difference between them corresponds to an error function. The objective of the learning process is to adjust the synaptic weights

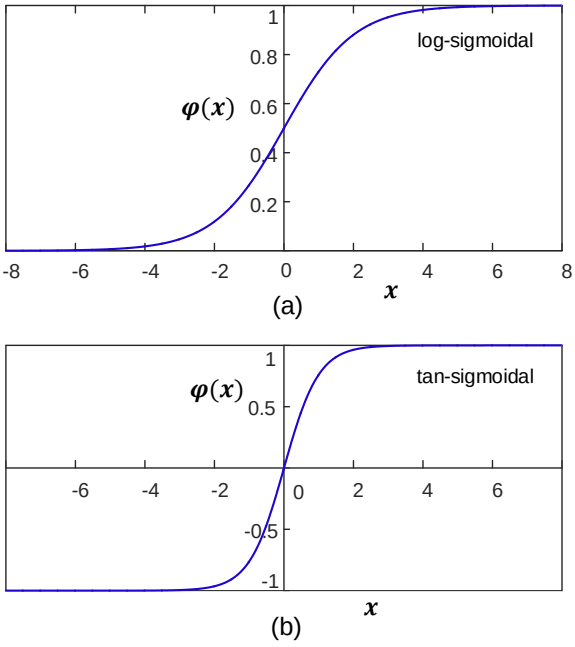

Figure 3.12: Activation functions (a) Log-sigmoid (b) Tan-sigmoid transfer function

and the biases of the network to minimize the error function. The training error function is a mean squared error (MSE) considered to be is equal to the average of the squared difference between the target and output, and defined as [91, 92]

$$MSE = \frac{1}{N}\sum_{k=1}^{N}(t_k - y_k)^2 \tag{3.30}$$

where N denotes the total number of patterns contained in the training set. Generally, the back-propagation algorithm is realized as the learning procedure of ANN because it is more effective in producing the desired values as output values. This algorithm computes the gradient of the error function to adjust the synaptic weights and biases for each iteration (epoch), which can contribute to minimization of the error. However, the standard back-propagation training algorithm converges very slowly. Because of this, various numerical optimization techniques, such as scaled conjugate gradient, gradient descent, gradient descent with momentum, and Levenberg-Marquardt, are applied in the standard back-propagation algorithm to enhance the speed of the learning process.

In the proposed ANN classifier, which is a three-layer feed-forward neural network, the

supervised Levenberg-Marquardt back-propagation (*trainlm*) training algorithm [90, 93] is been employed to update weight and bias values of the network. The Levenberg-Marquardt is one of the fastest optimization techniques used for back-propagation algorithms in ANNs. The training process of the ANN is repeated until the predetermined mean square error (0.2%) is achieved.

3.6 Summary

Chapter 3 discussed the various types of pattern recognition-based fault location techniques. The interaction of converter switching frequencies and parasitic capacitance of cable and PV panels produces high frequency noise signals with unique characteristics, which were used in the proposed fault location method. DWT was used for MRA, which decomposed the monitored signal into different frequency bands. Frequency response characteristics and the energy spectrum were analyzed to find the appropriate mother wavelet function (Daubechies db10) and the decomposition level for the MRA was calculated as 11. Furthermore, the norm values were extracted from the detail coefficients and used as feature vectors for the ANN classifier. Finally, the three-layer feed-forward neural network using the Levenberg-Marquardt back-propagation learning method was described and implemented as a fault classifier. Tan-sigmoid and log-sigmoid activation functions were utilized in hidden and output layers, respectively.

Chapter 4

Simulation Results

4.1 Introduction

As discussed in Chapter 2, the ungrounded multi-string PV system was modeled in a real-time electromagnetic simulation environment with RTDS. Then, the proposed pattern recognition-based fault location method described in Chapter 3 was implemented to detect and classify the exact fault location in the PV system. In this chapter, detailed simulation and classification results are presented for different kinds of faults at various locations in the PV system. Generally, the faults in PV arrays are mostly cable faults and PV panel faults. The proposed fault location method was tested for both types of faults. Finally, the behavior of the fault locator with different system parameters and noise levels was investigated.

4.2 Cable Faults

The underground cables used in large solar PV systems for transferring power from buck converters to the central inverters are prone to ground faults or line-line faults. These faults are usually due to failure of cable insulation or accidental short circuits between conductors with different potentials. The electromagnetic simulation models in RTDS were used to test the fault locating algorithm under different cable faults at various locations of the system. The detailed test system was described in Figure 2.5. The ground and line-line cable fault locations are shown and marked as loc. #1 to loc. #13. Here, the ground fault locations 1, 2, and 3 are at the positive conductor whereas locations 4 and 5 are at the negative conductor of the outgoing cable of DC-DC converter #1. Similarly, locations 6 and 7 simulate the ground

fault at the positive and negative conductors, respectively, of the output cable of DC-DC converter #2. In this case, the shortest cable length between two faults was selected to be 30 meters, which is the minimum resolution of the proposed fault locator. Also, locations 8 and 9 are ground faults at the positive conductor between DC bus and central inverter, and they are 100 meters apart from each other. Locations 10, 12, 13, and 11 are used to simulate the line-line faults in the DC and AC parts of the PV system, where locations 10, 12, and 13 are short circuit faults on inverter input and converter #1 and #2 outputs, respectively, and location 11 is line-line to ground fault on the infinite bus of the system. The following sections will describe the feature extraction and classification results for the above mentioned cable faults at different locations.

4.2.1 Results of Feature Extraction with DWT-based MRA

The fault locating method developed was first analyzed by simulating the PV system at a fixed operating condition with an irradiance of 1000 W/m^2, a temperature of 25^0C, and 50% humidity. Only low fault resistance (10 mΩ) is considered for the simulation. The mid-point voltage with respect to grounding of DC-DC converter #1, referred to as measured signal V_{mid1}, was analyzed using WT-based MRA with a db10 mother wavelet. This signal is recorded with a sampling frequency of 340 kHz and decomposed into 11 resolution levels covering the frequency of interest from 0.08 to 170 kHz, as shown in Table 3.1. The time domain waveform of the original signal, V_{mid1}, and its wavelet MRA decomposition results for ground faults at locations 1 and 2 are illustrated in Figure 4.1. Only the dominant frequency bands from D3 to D7 (as discussed in Section 3.4.6) are plotted. By comparing the detailed coefficients of the signal analyzed between the two ground fault locations, it is observed that the waveform patterns are quite different in terms of the magnitude of the noise signal and the time instants at which they appear for various frequency components.

Using these waveform patterns, norm values (corresponding to signal energy) are calculated in each frequency band and plotted as shown in Figure 4.2. The norms are used as features for pattern recognition, and demonstrate distinct patterns for the two fault locations. From Figure 4.2, a difference of approximately 1000 norms at levels 3 through 7

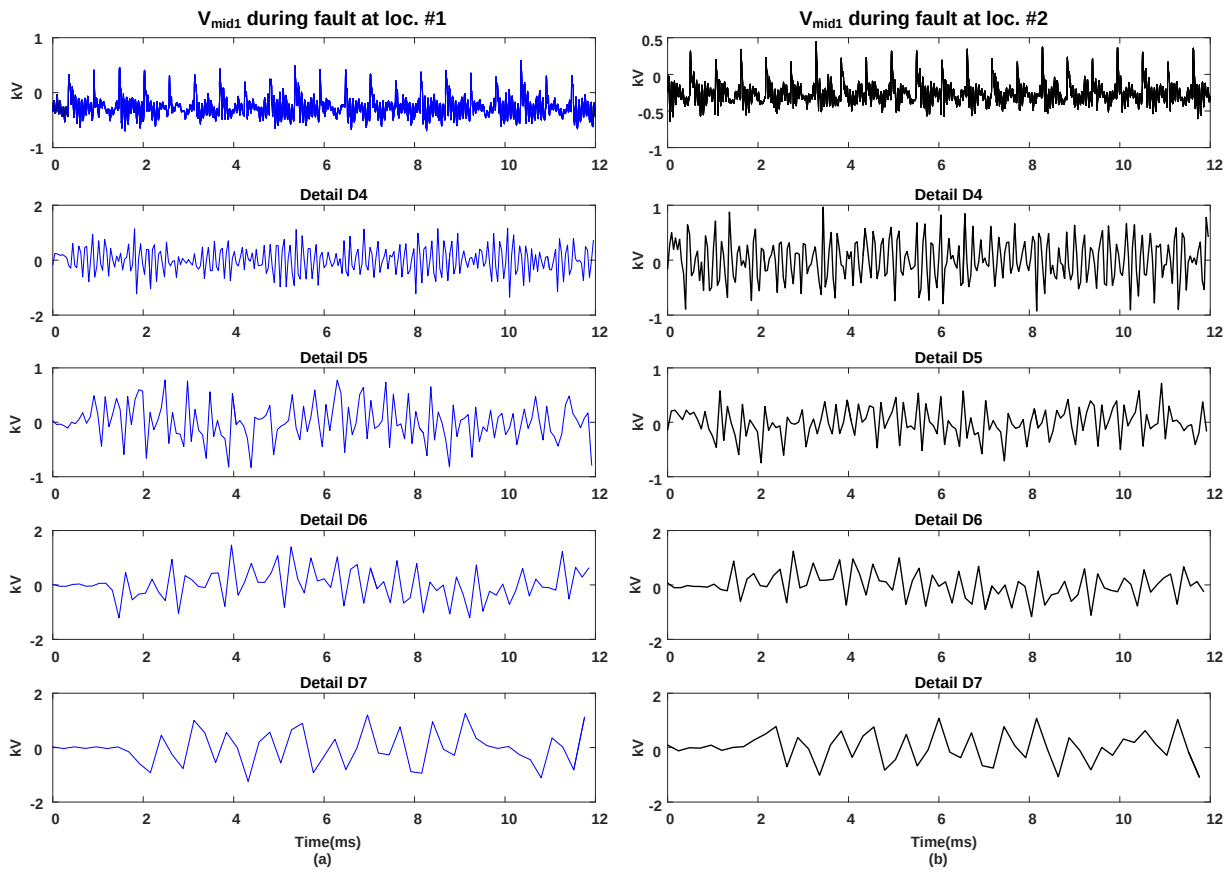

Figure 4.1: DWT-based MRA of V_{mid1} for faults at (a) Loc. # 1 and (b) Loc. # 2

is evident between the two fault locations. These differences in the norms reveal that the extracted features represent unique signatures for classification of ground faults at different locations.

The feasibility of the fault location method for short circuit faults using the wavelet feature extraction technique was also investigated. Line-line faults at different locations of the PV systems are simulated but, as an example, only a short circuit (SC) fault at the DC link of the inverter input (Loc. #10) and an SC fault at the high voltage side of the step-up transformer (Loc. #11) will be discussed. Figure 4.3 shows the extracted norms from wavelet MRA during faults at the DC side (Loc. #10) and the AC side (Loc. #11). The feature vector patterns of the DC and AC short circuits are drastically different. Also, the features of the AC side short circuits show large differences in the norms at resolution levels 4 through 7 compared to the DC side SC. This differences in features makes it possible

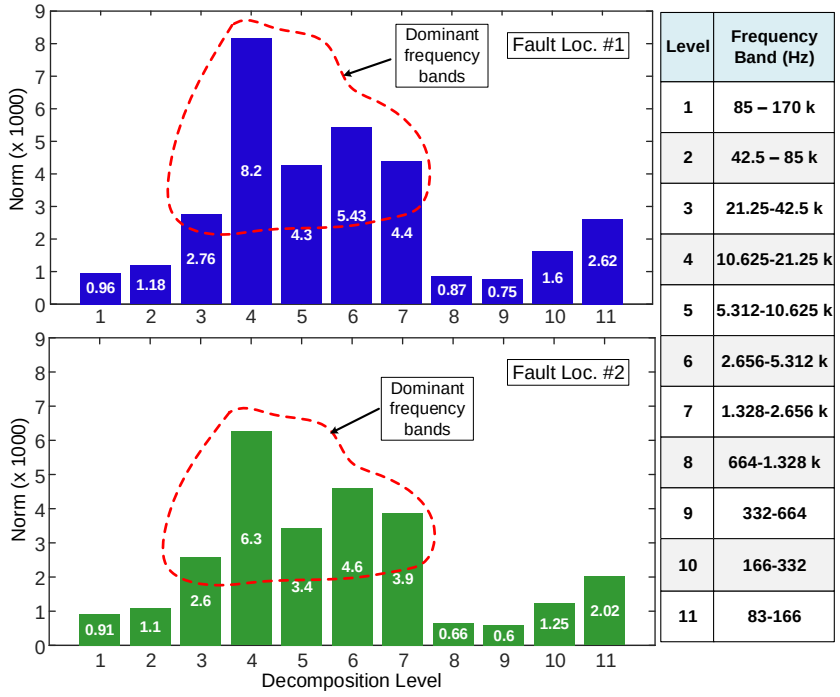

Level	Frequency Band (Hz)
1	85 – 170 k
2	42.5 – 85 k
3	21.25-42.5 k
4	10.625-21.25 k
5	5.312-10.625 k
6	2.656-5.312 k
7	1.328-2.656 k
8	664-1.328 k
9	332-664
10	166-332
11	83-166

Figure 4.2: Feature vector extracted for ground fault at Loc. # 1 and Loc. # 2

to differentiate SC faults on the DC side from SC faults on the AC side of grid connected PV systems.

It is possible to combine all of the characteristics of ground and line-line faults and derive a unique pattern for individual fault locations of the PV system. Figure 4.4 shows the feature patterns for ground faults at locations 1 to 7 for a specific PV system operating condition. In the dominant frequency bands shown in the highlighted portion of Figure 4.4, the norm values for each location are significantly different and can be used as input vectors for the ANN classifier. In particular, a large difference in the norms at decomposition level 4 is noted because the bandwidth (10.625 to 21.25 kHz) of this level covers the dominant resonant frequency of the noise signal of the PV system. Moreover, resolution levels 6 and 7 also provide clear distinguishable patterns of the norms for faults at different locations. The bandwidths of resolution level 6 and 7 cover the switching frequency of the inverter (3 kHz) and DC-DC converters (1.8 kHz).

In a similar manner, the norm patterns for line-line faults at locations 10 to 13 for fixed

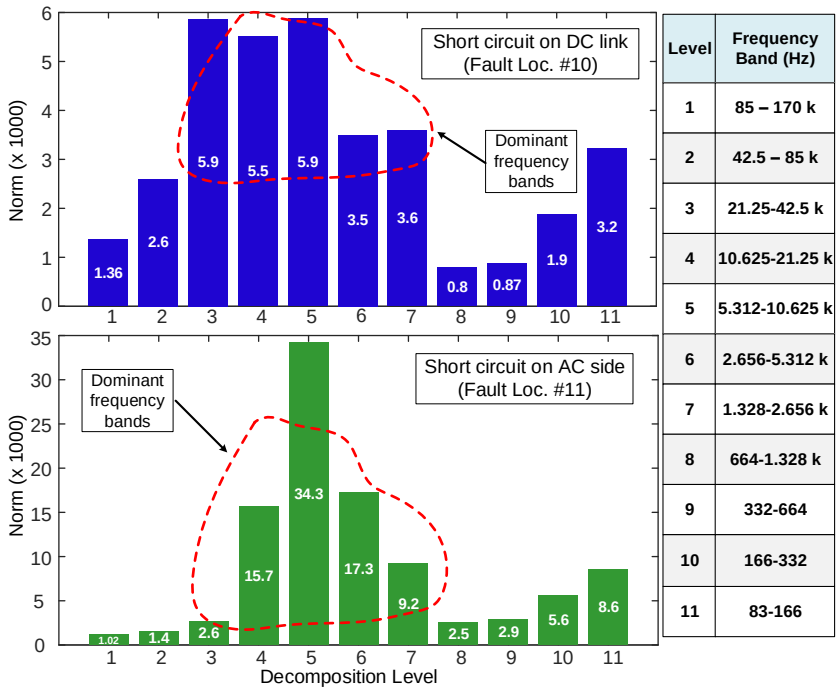

Level	Frequency Band (Hz)
1	85 – 170 k
2	42.5 – 85 k
3	21.25-42.5 k
4	10.625-21.25 k
5	5.312-10.625 k
6	2.656-5.312 k
7	1.328-2.656 k
8	664-1.328 k
9	332-664
10	166-332
11	83-166

Figure 4.3: Feature vector extracted for short circuit faults on the DC link (Loc. # 10) and AC side infinite bus (Loc. # 2)

operating conditions are shown in Figure 4.5. It can be noticed that a unique signature of SC fault locations at dominant frequency bands 3 to 7 can be achieved and pattern of this feature can be used to determine line-line fault locations for the DC and AC sides of the PV system.

The feature vectors obtained from the above analysis with the db10 wavelet were then used as inputs to the ANN classification algorithm. Thus, the aforementioned observations can be employed to generate an ANN-based classifier that can be installed online to locate different PV system faults.

4.2.2 Results of the ANN classifier

Typically, test cases are generated randomly by varying power output (irradiance level), temperature, humidity, and fault resistances for each fault location in the PV system. Table 4.1 shows the range of operating conditions simulated to obtain data for ANN training and

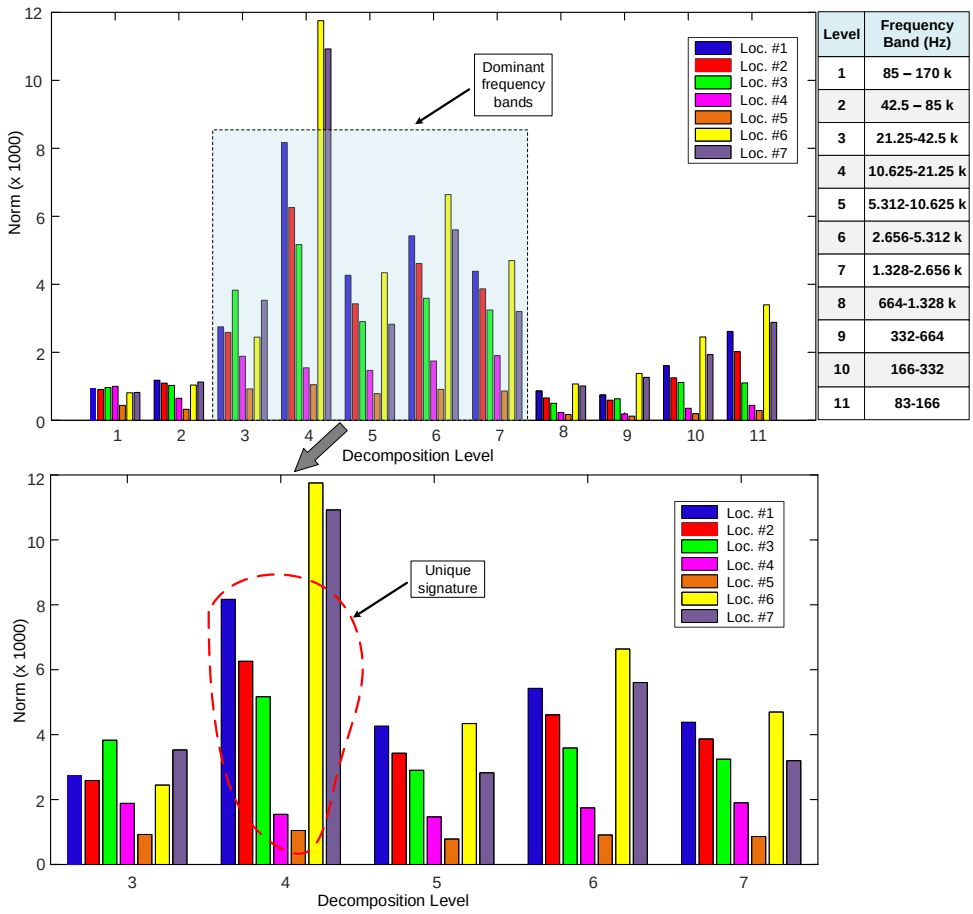

Figure 4.4: Feature patterns for ground faults at seven different locations

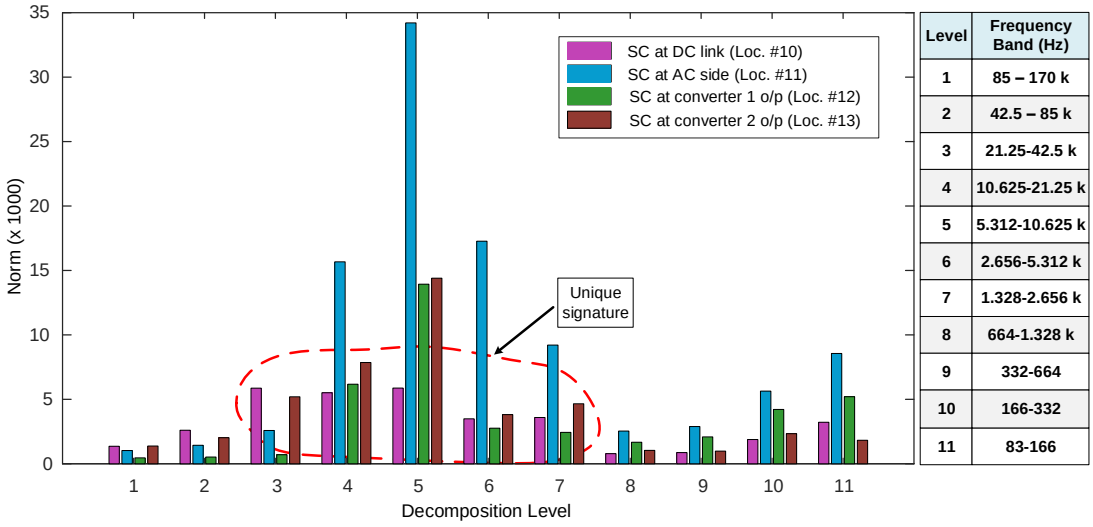

Figure 4.5: Feature patterns for line-line faults at different locations

testing. The behavior of the fault locating technique with different system parameters will be analyzed in Section 4.4.

Table 4.1: Operating parameter ranges for the PV system

Parameters	**Minimum**	**Maximum**
Power output	200 kW	500 kW
Insolation	250 W/m^2	1000 W/m^2
Temperature	10^0 C	30^0 C
Relative humidity	30 %	70 %
Fault resistances	10 mΩ	500 mΩ

In this thesis, 625 test cases of normal operating conditions and different system parameters for each fault location (Loc. #1 to #13) are simulated. Thus, the total training set consists of 8,750 sets (625 for each of the 13 faults and 625 for the no fault case). The feature vectors are generated for each case to utilize as inputs to the ANN classifier. Two sets of training data were used for comparison. The network was first trained with 50% of total test cases (8,750 test scenarios) and tested for the remaining 50%, which gave a 98.02% accuracy. In the second scenario, 80% of the total test cases are used for ANN training and the rest of the data are used for testing, which gave an accuracy of 99.177%. In general more training data gives accurate results but also requires longer training time (note that the final computational time of the method would remain the same). The 80-20% training-testing set results are reported in the rest of thesis.

As stated in the previous chapter, the three-layer feed-forward neural network with 11 input, 18 hidden, and 12 output neurons was trained off-line using the Levenberg-Marquardt optimization technique in a MATLAB neural network toolbox [90] until MSE (as an indicator of performance) was $< 0.2\%$. The trained ANN classifier was tested and validated for new test scenarios, which were not used in training, to illustrate how accurately the proposed method is able to locate the faults. The outputs of the ANN vary from 0 to 1 due to use of a log-sigmoid activation function in the output layer. Because the outputs of a multi-layer neural network rarely give exactly the target of 0 or 1 for each output neuron, a decision threshold output level of 10% is built into the ANN, i.e., outputs < 0.1 are classified as undisturbed and outputs > 0.9 are considered as faulty cases.

Typically, the accuracy of the fault location technique is expressed as:

$$\% \text{ accuracy} = \left(1 - \frac{\text{number of classification error}}{\text{total number of test cases}}\right) \times 100 \tag{4.1}$$

where the total number of test cases simulated for cable faults is equal to 8,750.

Table 4.2: Fault location results for cable faults in PV systems

Fault location	Accuracy	Average	Overall accuracy
No fault	100 %	99.92 %	99.177 %
Loc. #1	99.2 %		
Loc. #2	100 %		
Loc. #3	100 %		
Loc. #4	100 %		
Loc. #5	100 %		
Loc. #6	100 %		
Loc. #7	100 %		
Loc. #8	100 %		
Loc. #9	100 %		
Loc. #10	94.24 %	97.32 %	
Loc. #11	100 %		
Loc. #12	100 %		
Loc. #13	95.04 %		

The fault location accuracy was calculated for simulated test scenarios for ground and line-line faults. Table 4.2 illustrates the fault location results for cable faults in PV systems. It is noted that a 99.92% correct fault locating rate is obtained for ground faults, whereas a 97.32% success rate was found for line-line faults. Thus, the overall fault locating accuracy for cable faults in PV systems is 99.177% with the proposed fault location method. For line-line faults at DC cables, no circulatory loop is formed by the fault point and the parasitic elements of the PV modules and cables. Hence, only a small amount of high frequency noise due to leakage currents to ground would be produced and this is what was used to locate the SC fault locations. In addition, the features of the short circuit faults at locations 10 and 13 are slightly similar to one other. Therefore, the fault location accuracy for DC line-line faults is marginally lower compared to the ground fault location accuracy. An overall accuracy of 99.177% demonstrates the effectiveness of the developed technique to correctly locate the faults on an ungrounded PV system.

4.3 PV Panel Faults

Utility-scale solar farms consist of large numbers of PV modules to generate the bulk power. In practice, PV panels are subjected to different kind of faults such as ground faults, intra-string and cross-string faults (i.e., line-line type faults), open circuit faults, and mismatch faults. Major manufacturers have reported that around 1% of the total number of installed PV panels are likely to fail annually. Ground type faults and line-line faults are considered to be frequently occurring faults in PV systems. Therefore, the test results for ground faults and line-line type faults in PV modules are presented in this thesis.

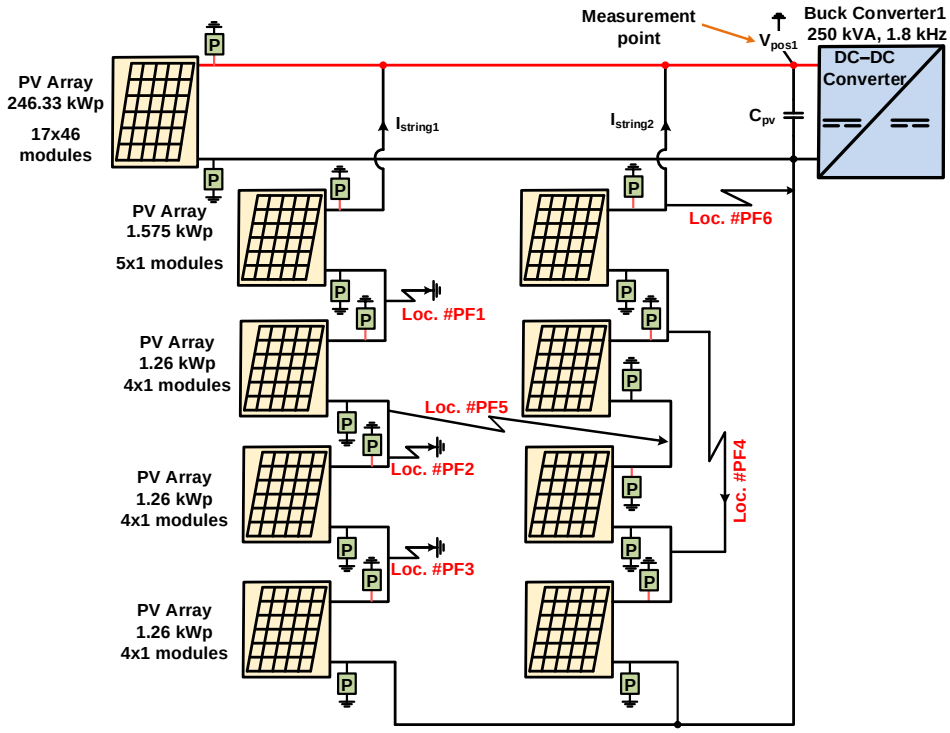

Figure 4.6: Different types of faults in PV farms

Figure 4.6 shows the PV module configurations of 250 kWp PV array 1 of the PV test system shown in Figure 2.5. Each PV array consists of 48 parallel strings with 17 modules in each string. To demonstrate the fault location method in PV farms, two strings are separated and the rest are treated as a PV array of 46 strings. Each string is divided into four sections, with one group of 5 panels and three groups of 4 panels as shown in Figure 4.6. Real-time electromagnetic simulations of the PV test system with this detailed PV array configuration

were carried out for faults at various locations of the farm, with different system parameters as described in Table 4.1. Three fault locations, $PF1$, $PF2$, and $PF3$, simulate ground faults on string 1. Similarly, $PF4$ simulates a short circuit fault on string 2, $PF5$ simulates a cross-string line-line fault, and $PF6$ simulates an intra-string line-line fault.

Table 4.3: Frequency bands of different decomposition levels for PV panel faults

Decomposition Level	**Frequency Band (Hz)**
1	5 - 10 k
2	2.5 - 5 k
3	1.25 - 2.5 k
4	625 - 1.25 k
5	312.5 - 625
6	156.25 - 312.5
7	78.125 - 156.25
8	39 - 78.125
9	19.5 - 39

Due to the limited simulation capability of the real-time digital simulator, PV panels could not be modeled in small time-steps (2.94 μs). Therefore, the PV farms shown in Figure 4.6 were simulated in large time-steps (50 μs) and the electrical information transferred to small time-step simulations as discussed in Section 2.2. The input positive terminal voltage with respect to grounding of buck converter #1, V_{pos1}, was measured and analyzed using DWT-based MRA with a db10 mother wavelet. This signal was recorded with a sampling frequency of 20 kHz and decomposed into 9 resolution levels covering frequeincies from 0.195 to 10 kHz, as shown in Table 4.3. For standard operating conditions of the PV system, norm values of six fault locations are extracted for each frequency band and patterns are plotted in Figure 4.7. It can be seen from the bar diagram that there is a large difference in the norms for different fault locations for frequency bands 1 to 6, which makes the proposed fault location method practical for PV faults. Typically, decomposition levels 2 and 3 cover switching frequencies of inverter and buck converters, respectively. Also, level 6 contains the third, fourth, and fifth harmonics of the fundamental power frequency (60 Hz) and provides clear differentiation in norm values for different fault locations.

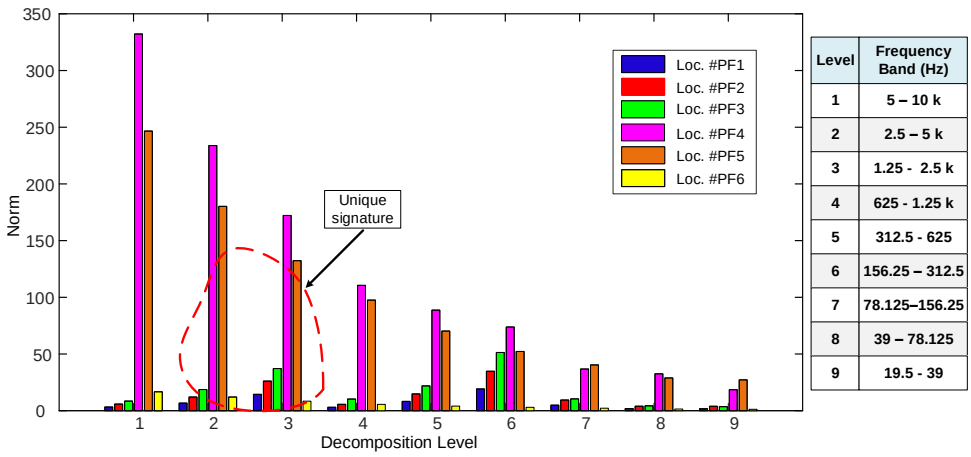

Figure 4.7: Feature patterns for faults in PV modules (Loc. $\#PF1$ to Loc. $\#PF7$)

As in the case of cable faults, 625 test cases were simulated for each fault location with different system parameters provided in Table 4.1. Thus, the total number of test scenarios for PV panel faults simulated was 4,375. The feature vectors were extracted for each case from the detailed coefficients obtained from the MRA decomposition of the monitored signal. Then, 80% of the 4,375 cases were utilized to train the ANN and 20% were used to test and validate the fault location algorithm. The ANN classifier as discussed in Section 4.2.2 with 9 input, 18 hidden, and 7 output neurons was trained until the MSE was $< 0.6\%$. After training the ANN, the fault location accuracy was computed using Equation 4.1 for the various test scenarios for ground faults and different line-line faults in PV farms.

Table 4.4: Fault location results for PV module faults

Fault location	Accuracy	Average	Overall accuracy
No fault	100 %	98.08 %	97.851 %
Loc. $\#PF1$ (ground fault)	99.36 %		
Loc. $\#PF2$ (ground fault)	99.68 %		
Loc. $\#PF3$ (ground fault)	95.2 %		
Loc. $\#PF4$ (SC fault)	93.44 %	96.91 %	
Loc. $\#PF5$ (cross-string fault)	97.28 %		
Loc. $\#PF6$(intra-string fault)	100 %		

Table 4.4 shows the accuracy of the proposed fault location technique for PV module faults in an ungrounded PV system. The proposed algorithm can correctly classify 98.08% of ground faults and 96.91% of line-line faults the in PV modules. This indicates that an

overall fault location accuracy of 97.851% can be obtained for PV panel faults with the fault location method developed in this thesis. The fault location accuracy for ground faults is higher because the parasitic element and the fault path form a closed loop as shown in Figure 4.6; for line-line faults, there would be no closed-path between the fault and the cable parasitic elements.

4.4 Sensitivity analysis

In real applications, operating parameters of PV systems, such as irradiance, temperature, PV parasitic elements, fault resistance, and switching frequencies of the converters, might change with time. The following study analyzes the effect of these parameters on the high frequency noise patterns and the proposed fault location method. Furthermore, the monitored signals in real PV systems usually have environment noise and transducer error, which will also affect the performance of the fault location method. Therefore, parameter sensitivity analysis, which examines the impact of varying temperature, insolation, parasitic elements, and fault resistance, etc., was done to investigate the feasibility of the fault location approach for practical applications.

4.4.1 Performance of classifier for different noise conditions

The error of signal measurement sensors and environment noise were considered as additive white Gaussian noise (AWGN) in this research. In order to examine the robustness of the fault locating algorithm for different noise conditions, the fault location performance was tested with input signals containing various signal to noise ratio (SNR) values between 20 and 50 dB. The value of the SNR is given by

$$\text{SNR (dB)} = 10 \log \left(\frac{P_s}{P_n} \right) \tag{4.2}$$

where P_s is the power of the signal and P_n is that of the noise. A typical SNR value of 30 dB is equivalent to a peak noise magnitude of nearly 3.5% of the voltage signal [94].

Table 4.5: Percentage of correct cable fault locations for different SNR values

Fault location	20 dB	35 dB	45 dB	50 dB
No fault	100	99.84	100	100
Loc. #1	100	99.84	100	99.36
Loc. #2	100	99.68	99.68	99.84
Loc. #3	99.84	99.84	100	100
Loc. #4	98.72	99.68	100	100
Loc. #5	100	100	100	100
Loc. #6	100	100	100	100
Loc. #7	100	100	100	100
Loc. #8	99.2	99.84	100	100
Loc. #9	100	99.84	100	100
Loc. #10	88.64	99.28	99.28	92.64
Loc. #11	100	100	100	100
Loc. #12	100	100	100	99.36
Loc. #13	87.04	85.12	88.48	91.52
Overall	98.10	98.35	98.96	98.76

The performance of the fault locator for the cable and PV faults in noisy conditions was analyzed in this research. However, only results of the cable faults are discussed. Results of the fault location algorithm for cable faults using the voltage waveform contaminated with various level of noise are presented in Table 4.5. It is noted that although the accuracy decreases with the noise level, a satisfactory fault locating success rate can be achieved even though the input signals contain different levels of noise. Table 4.5 shows that an overall accuracy of 98.10% can be still obtained even with a high noise level of 20 dB. Thus, it is clear that the proposed fault location algorithm has robust performance with noisy inputs.

A comparison of the fault location accuracies with the various features extracted from norms, energy, RMS, variance, and mean was undertaken, and the results are presented in Figure 4.8. The results show that the proposed norm-based approach gives better accuracy and is robust for different noise levels. The results obtained also show that the features generated from the mean have a low accuracy and are also not robust under noisy conditions.

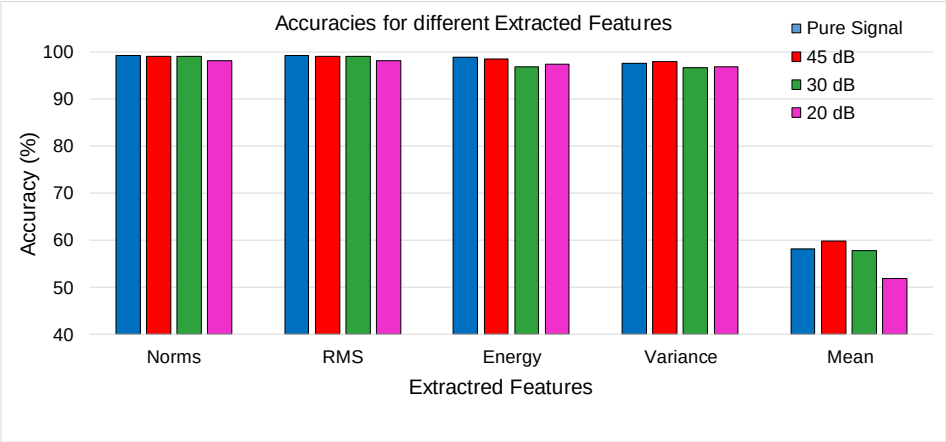

Figure 4.8: Accuracy of different extracted features

4.4.2 Variation of Fault Resistance

Fault resistance is in the path of grounding oscillatory circuits, and will impact the generated noise patterns. Resistance of cables for frequencies in the hundred of kHz is 300 mΩ as shown in Table 2.1. For the bolted fault types (resistances on the order of several mΩ) or faults with small resistance values less than 100 mΩ, the loop resistance is still going to be dominated by the cable resistance. Therefore, fault resistances <100 mΩ do not change the noise level very much. In contrast, when the fault involves high resistance, the degree of its impact on the noise level largely depends on the specific fault resistance. For ungrounded PV systems, however, we can locate the high resistance fault when it evolves into a small resistance fault.

Figure 4.9 shows the effect of fault resistance on the accuracy of the fault locator for ground and line to line fault types at different locations of the PV system. It can be clearly seen that the fault location error does not exceed 2.4% in the worst case condition for the ground faults at 500 mΩ. But, in the case of line-line faults at 500 mΩ or above, SC faults at the inverter input (Loc. #10) and converter 2 output terminals (Loc. #13) result in more than 14% location error. This means the fault locator is more immune to changes in fault resistance (0 to 300 mΩ) for ground faults but marginally less immune for line-line faults.

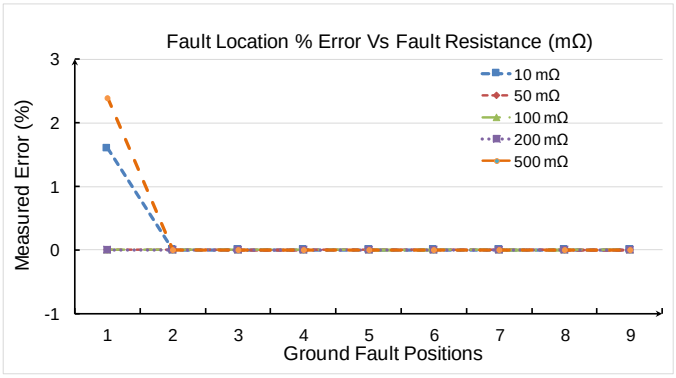

(a)

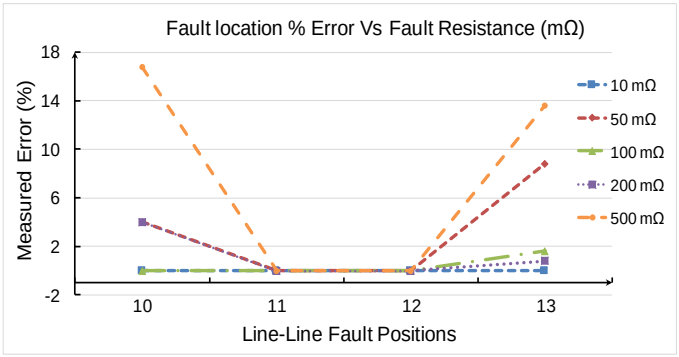

(b)

Figure 4.9: Effect of fault resistance during (a) ground faults and (b) line-line faults

4.4.3 Variation of Power Generation

The output power of the PV arrays mainly depends on the solar insolation values at the time of operation. As shown in Table 4.1, when the solar insolation level varies between 250 and 1,000 W/m^2, the power output changes from 200 to 500 kW. Basically, changing the output power will change the amount of current to be switched on and off by the switching operation of power converters, which act like a high frequency noise generator. For a fault at a given location, varying the insolation levels will only change the magnitude of the measured noise but the noise pattern bars where it peaks will be the same.

Figure 4.10 illustrates the performance of the fault locator with varying output power for ground and line-line faults. It is interesting to note that the fault location error is almost 0% for ground faults in all locations, except is 3.2% at Loc. #1 with a change in solar insolation.

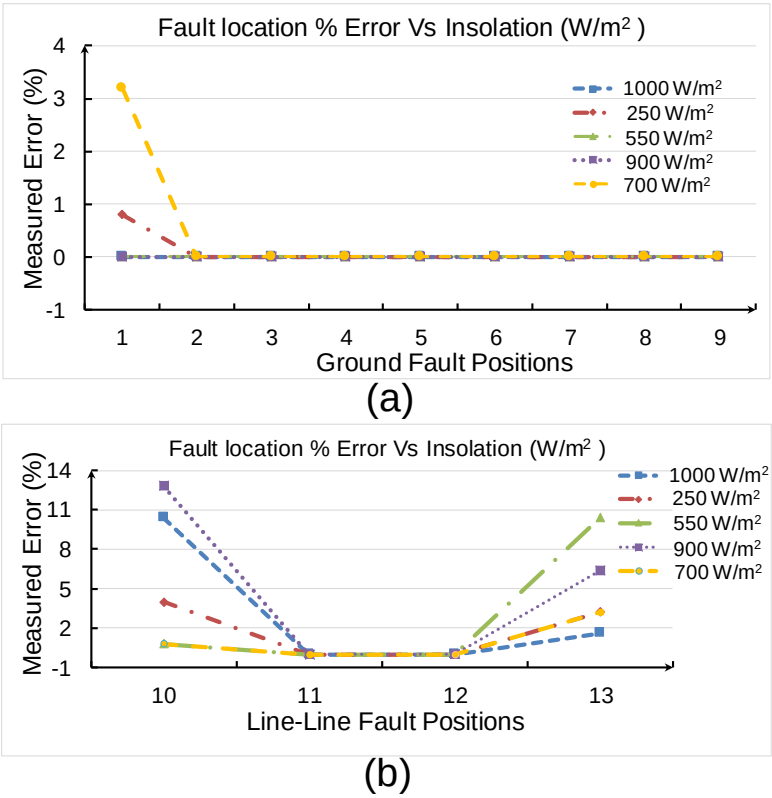

Figure 4.10: Effect of insolation (power output) during (a) ground faults and (b) line-line faults

However, in case of line-line faults, the fault location error jumps to 12.8% at 900 W/m^2 for a SC fault at Loc. #10. Figure 4.10 (b) shows that higher insolation levels slightly affect the accuracy of the fault location method in the case of line-line faults at Loc. #10 and Loc. #13 because these faults do not include ground loops, which generate nearly similar features for the two locations.

4.4.4 Variation of PV Parasitic Elements

As mentioned previously, the parasitic elements of the PV panels are mostly dependent on environmental parameters such as ambient temperature and humidity. Variations in humidity play as significant role in changes of parasitic capacitance. Five different values of parasitic elements were obtained by varying humidity from 30 to 70% and used to study the

effect of parasitic elements on the performance of the fault locator.

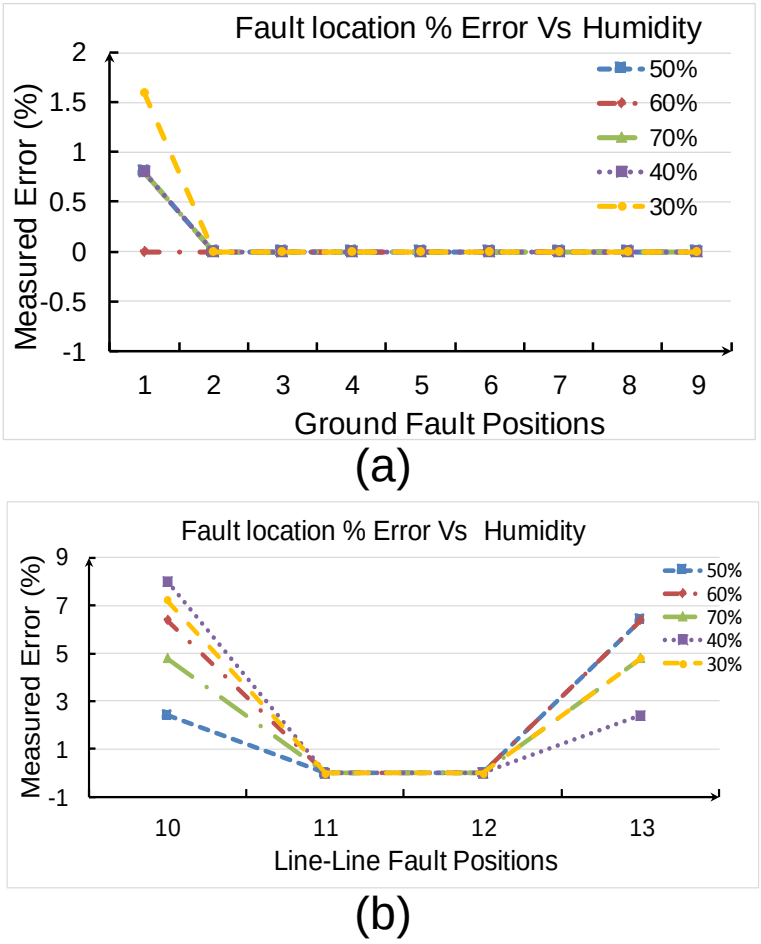

Figure 4.11: Effect of PV parasitic element (humidity) during (a) ground faults and (b) line-line faults

Figure 4.11 (a) demonstrates that the change in parasitic elements has no effect on the performance of the fault locator for ground faults. The fault location error in this case does not exceed 1.6% in the worst case condition. On the other hand, Figure 4.11 (b) clearly explains that the measured error at low humidity (about 30% and 40%) does not go beyond 8% for a short circuit fault at the inverter input terminal (Loc. #10). Thus, it is clear that the change in parasitic elements does not affect the fault location accuracy for ground faults but slightly affects them for line to line faults.

4.4.5 Variation of Temperature

Ambient temperature affects the power output and the parasitic elements of PV modules. Real applications would be subjected to temperature variations. Hence, it is important to study the fault locator with varying temperature values. Generally, temperature variation does not change the oscillatory loops, so varying the temperature of the modules does not change the noise signature within the same loop.

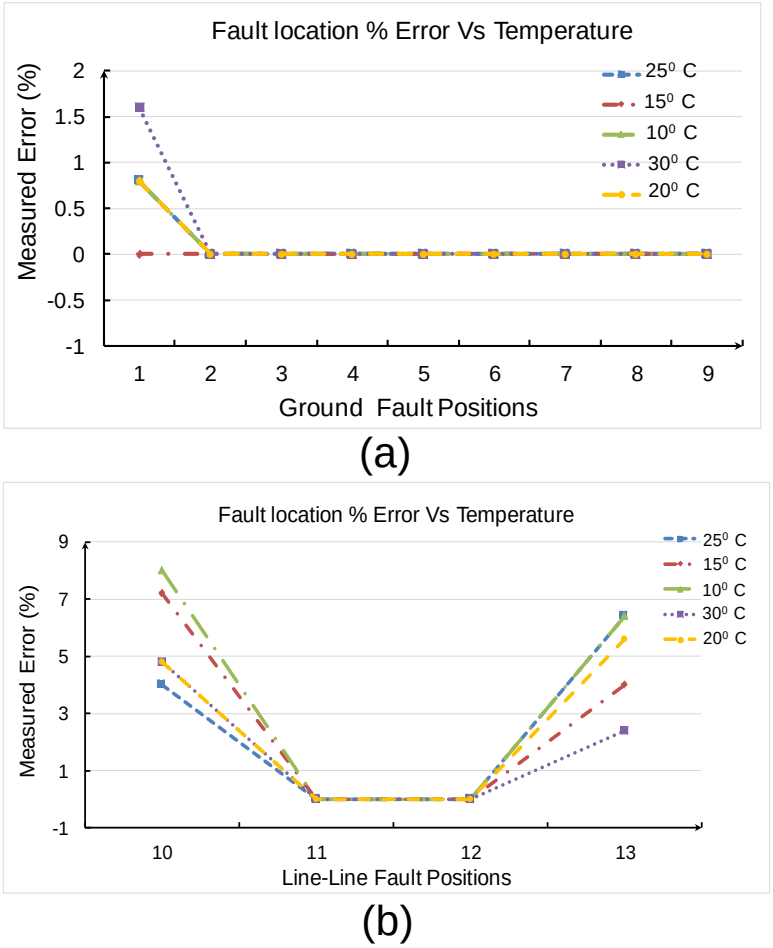

Figure 4.12: Effect of temperature during (a) ground faults and (b) line-line faults

Figure 4.12 (a) illustrates how variations in temperature do not affect the accuracy of the fault location technique for ground faults. The fault location error for higher ambient temperatures (30^0C) does not exceed 1.6% for a ground fault at Loc. #1. In contrast, Figure

4.12 (b) clearly shows the measured error at low ambient temperatures (about 10^0 and 15^0C) does not exceed 8% in the worst case condition for a line to line fault at the inverter input terminal. Therefore, the change in temperature has no effect on the fault location accuracy for ground faults but has a small affect for line to line type faults.

4.4.6 Switching frequency of converters

Inverter manufacturers can design converters with different switching frequencies to achieve various system specifications. It is important to analyze the performance of the proposed fault locator with different switching frequency ranges. The simulation studies with different switching frequencies of the power converters illustrate that the switching frequency has a marginal impact on the high frequency noise level.

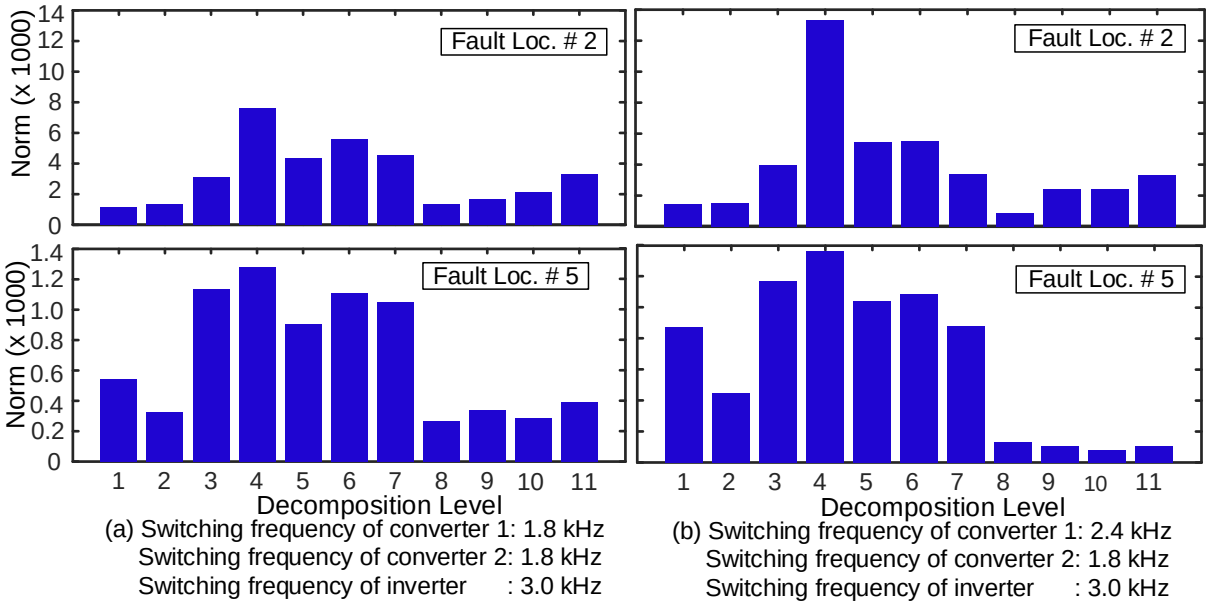

Figure 4.13: Effect of switching frequencies

It has been shown in previous work [31] that the switching frequency can affect the noise level primarily due to two reasons. On one hand, higher switching frequency results in more switching operations in a given time interval. Each switching operation introduces high frequency noise, so more switching operations will result in higher noise levels when the

magnitude or energy of the noise is measured within the time range. On the other hand, a higher switching frequency means a shorter switching period, so the maximum current reached will have a lower value. Because the average current is the same as the load current and the time period (L/R) is a constant, a smaller switching interval therefore leads to less energy flow in the current leakage path due to the switching operation.

Figure 4.13 shows a case when the switching frequency of converter 1 increased from 1.8 to 2.4 kHz while that of the inverter and another converter remained the same. It is noted from the results that the norms slightly increased without changing the pattern of the features for each fault location. Hence, with varying switching frequencies, the feature vectors will provide nearly similar characteristics at different MRA levels and not affect the performance of the fault locator very much.

4.5 Summary

This chapter presents the results obtained from time-frequency resolution with WT-based MRA for different cable and PV module faults in PV systems. The results of the feature extraction show that the norm values give distinguishable patterns at dominant frequency bands for ground faults and line-line faults at various location of PV modules and cables.

The performance of the ANN classifier was also discussed and results presented for both cable and PV module faults. The results from the classifier show that an overall fault location accuracy of 99.177 and 97.851% could be achieved for cable faults and PV module faults, respectively. In the case of cable faults, fault accuracies of 99.92 and 97.32% were be found for ground and line-line type faults, respectively. On the other hand, the proposed algorithm could correctly classify 98.08% of ground faults and 96.91% of line-line faults in PV modules. The results obtained from the ANN classifier demonstrate that the proposed fault locator is very accurate for ground faults and also gives good accuracy for line to line faults in ungrounded PV systems.

There are no publications available in the research literature discussing the accuracy of fault location methods for PV systems, but there are publications discussing wavelet methods for DC shipboard distribution systems. So, a comparison was made with the results obtained for the DC shipboard distribution systems. Work conducted at Florida State University [31, 32] on wavelet and fractal analysis of high frequency signals at the inverter terminals shows a clear differentiation between two fault locations. An overall fault classification accuracy of about 99.58% was obtained using a wavelet and ANN based method for an ungrounded DC shipboard distribution systems [34]. The above results show that the proposed wavelet and ANN approach discussed in this thesis gives comparable results to those obtained for DC shipboard power systems.

A sensitivity analysis was also done to examine the impact of system parameter variations and environment noise levels. The results showed that an overall accuracy of 98.10% could be still obtained, even with a high SNR value of 20 dB. Moreover, fault location performance was studied for different features extracted from norms, energy, RMS, variance, and mean, and the results showed that the proposed norm-based approach gives better accuracy and is robust for different noise levels. The studies also showed that changed in operating parameters have an insignificant effect on the performance of the proposed method. Sensitivity analysis was also done taking into account the fault location, fault resistances, parasitic elements of PV panels, temperature, and power outputs. The ANN classifier could be trained with actual fault data records to make the approach robust for practical applications.

Chapter 5

Summary and Conclusions

5.1 Summary

Ground fault location in ungrounded PV systems has always been a challenging task. As discussed in Chapter 1 of this thesis, there is no circulating fault current due to only one ground fault in an ungrounded PV system. Thus, ground faults are difficult to detect using traditional current sensing devices. Also, the second ground fault on a healthy line causes a short circuit in the system. Hence, it is important that the ground fault be detected, located, and isolated from the ungrounded PV system as soon as possible. Different existing fault location methods described in the literature generally locate the fault manually or by costly current sensors and relays. Therefore, the main objective of this thesis was to develop a fault location technique for ungrounded PV systems that does not need any additional high frequency signal injector, is accurate, and avoids manual testing with a probe.

This thesis presented a fault locator based on the characteristics of the high frequency noise initiated by the repetitive switching transients of converters interacting with parasitic elements of cables and PV panels. In ungrounded PV systems, the different fault locations result in different fault current loops and different noise patterns. Thus, the proposed fault locator is based on the recognition of high frequency noise patterns introduced in the system. The main objective of this thesis was to develop an accurate technique for finding the fault positions and to test the performance of the method for different system parameters. Therefore, time domain noise signals were first transformed into time-frequency domain signals using the DWT technique and then the ANN was used to find the exact fault locations.

Electromagnetic simulations/real-time simulations were very helpful for testing the performance of the developed fault locator. Chapter 2 discussed the highly detailed transient simulation model of each component of an ungrounded, 500 kWp, multi-string PV farm a in real-time simulation platform. RTDS was utilized with a small time-step of 2.94 μs for electromagnetic simulations. The sampling rate and the measurement window size were determined for a frequency range from 0.1 to 170 kHz. A frequency dependent π cable model was used instead of the lumped parameter π model to accurately capture the high-frequency behavior of the cable.

The DWT based-MRA technique was studied in this thesis to extract the unique features of the noise signal measured at the mid-point of the DC-DC converter. Then, the norm values of the different resolution scales were utilized as a feature vector for pattern recognition. The suitable mother wavelet and the optimum decomposition levels were chosen according to the characteristics of the noise waveform so that the proposed fault locating method achieves better performance. Moreover, the three-layer feed-forward ANN was adopted as a classifier of the pattern recognition-based fault locator to classify exact fault locations. The feature vectors extracted for each fault location were used as inputs and gave the fault position as an output of the ANN. The network was trained with a Levenberg-Marquardt back-propagation learning algorithm as discussed in Chapter 3.

The fault location method studied in Chapter 3 was implemented for different types of faults at different locations of the PV system. The detailed simulation and feature extraction results obtained demonstrate that the feature vectors of each fault position provide a unique signature, which made possible location of the fault location. Ground faults and line-line faults were applied at various locations of the test system. An ANN classifier was capable of identifying exact fault locations for the cables and PV modules of the ungrounded PV systems. Furthermore, the ANN classifier results illustrated that the fault locator is highly accurate for ground faults and achieves satisfactory performance for line to line faults.

Another important piece of the investigation that was carried out was the parameter sensitivity analysis, which analyzed the impact of varying power outputs, temperature, fault impedances, PV parasitic elements, and switching frequencies of the converters to examine

the feasibility of the fault location technique for practical applications. The fault locator performance was also tested with noisy input signals and the results show that the fault location algorithm has a robust performance in a noisy environment and with varying system parameters.

In a nutshell, this thesis demonstrated the benefits of the pattern recognition-based fault location approach using wavelet MRA and an ANN. It was shown in the thesis that the fault locator required only one voltage signal as an input, which actually reduced the number of sensing devices as well as costs. Different simulation and classification results show the proposed method is promising, accurate, and robust with respect to changes in operating parameter values. This locator can automatically find the fault points even if the PV systems are in operation. Thus, it reduces fault locating time and also minimizes the risk of electric shock hazards for personnel working in PV power plants.

5.2 Thesis Contributions

The major contributions of this thesis are as follows:

- *Developing a real-time simulation model of a utility-scale multi-string ungrounded solar PV farm taking into account the complexities of maximum power point tracking of the PV array and the frequency dependent cable model:* As discussed previously, detailed real-time electromagnetic simulation models are capable of accurately representing system behavior of an ungrounded multi-string PV system. In this thesis, an MPPT algorithm was implemented in the DC-DC converter to generate maximum power from PV arrays. The two-level, three-phase, voltage source inverter was modeled along with the AC harmonic filter. The simplified voltage control algorithm was utilized to control power flow through the inverter and the PWM technique was employed to generate firing control signals. Additionally, the frequency dependent π cable model was used for transient modeling of short cables. The simulation model developed was a combination of large time-step and small time-step models in RTDS to simulate all components of an ungrounded PV system.

- *A pattern recognition-based fault location technique using DWT-based MRA and ANN for ungrounded PV systems:* The proposed fault location scheme is based on the system generated background noise waveform, which features different patterns for faults at different locations. The use of WT-MRA provided better time-frequency resolution of the transient voltage waveform and was also capable of extracting unique features for pattern recognition. The neural network classifier was trained with fault data obtained from RTDS simulations. Test results showed that the designed fault locator is highly accurate for ground and line-line faults and for cases of both cable and PV module faults in PV systems. This fault location approach allows the selection of an appropriate mother wavelet function and frequency resolution level with respect to the characteristics of the noise waveform to achieve better performance. Furthermore, the proposed fault locator does not require any extra equipment compared to existing methods in the literature; it actually requires fewer transducers and does not require any costly external high frequency generators. This fault location approach could be used when a PV system is in operation.

- *Testing the proposed approach with varying system parameters and examining performance of the fault locator with noisy input signals:* The effectiveness of the proposed approach was verified using detailed EMT simulations for various test scenarios by varying system parameters and environmental noise levels. The fault locator showed encouraging results in all test cases, validating the feasibility, accuracy, and robustness of the proposed design.

5.3 Future Works

Based on the research carried out in this thesis, the following studies are recommended for future investigations:

- *Application of the proposed method for fault locations on the AC side distribution lines of PV systems:* The method can be tested on the AC side distribution lines of ungrounded PV systems. Although a line-line fault at infinite bus was studied in this

thesis, distribution side fault location is also an interesting topic for future investigations.

- *Testing the proposed algorithm for different solar PV topologies:* This research work only tested the proposed fault locator for a multi-string PV farm connected to the grid. It would be interesting to apply this algorithm to other PV topologies, such as central inverter types, string inverter types, and stand alone type PV configurations. In these cases, further investigations will be needed to utilize more than one system signal containing noise for signal analysis.

- *Implementation of the proposed technique into industrial hardware and performance of real-time hardware-in-the-loop (HIL) testing:* The fault locator algorithm could be developed on fast processing hardware (e.g., FPGA) for industrial use and the real-time HIL testing of the fault locator done with a RTDS. This would assist in verification of the method and also demonstrate the practicality of the fault locator in real field conditions.

- *Validating the proposed fault location algorithm using real fault data records from practical ungrounded PV power plants:* The proposed fault location approach could be validated using real fault data records obtained from PV farms. This will comprise additional validation of the proposed method.

References

[1] S. E. I. Association *et al.*, "US Solar Market Insight: 2015 Year in Review (Executive Summary)," *Washington, DC March*, 2016. [Online]. Available: http://www.seia.org/sites/default/files/gMOip8F78iSMI2015YIR.pdf

[2] B. Brooks, "The ground-fault protection blind spot: Safety concern for larger PV systems in the US," *Solar American Board for Codes and Standards*, 2012.

[3] M. K. Alam, F. Khan, J. Johnson, and J. Flicker, "A Comprehensive Review of Catastrophic Faults in PV arrays: Types, Detection, and Mitigation Techniques," *Photovoltaics, IEEE Journal of*, vol. 5, no. 3, pp. 982–997, 2015.

[4] W. I. Bower and J. C. Wiles, "Analysis of grounded and ungrounded photovoltaic systems," in *Photovoltaic Energy Conversion, 1994., Conference Record of the Twenty Fourth. IEEE Photovoltaic Specialists Conference - 1994, 1994 IEEE First World Conference on*, vol. 1, Dec 1994, pp. 809–812 vol.1.

[5] G. Ball, B. Brooks, J. Flicker, J. Johnson, A. Rosenthal, J. Wiles, and L. Sherwood, "Inverter Ground-Fault Detection Blind Spotand Mitigation Methods," *Solar American Board for Codes and Standards*, 2013.

[6] M. Falvo and S. Capparella, "Safety issues in PV systems: Design choices for a secure fault detection and for preventing fire risk," *Case Studies in Fire Safety*, vol. 3, pp. 1–16, 2015.

[7] D. B. Jason Fisher, "Ungrounded PV Power Systems in the NEC," *Solar Pro*, vol. 5.5, August/September 2012. [Online]. Available: http://solarprofessional.com/print-issue/august-september-2012

[8] Bender, "Ground Fault Protection Photovoltaic Systems," *Brochure*, no. NAE1111041, 09 2012. [Online]. Available: http://www.bender-us.com/documents/Solar_brochure_NAE1111041.pdf

[9] J. Flicker, J. Johnson, M. Albers, and G. Ball, "Recommendations for isolation monitor ground fault detectors on residential and utility-scale pv systems," in *Photovoltaic Specialist Conference (PVSC), 2015 IEEE 42nd.* IEEE, 2015, pp. 1–6.

[10] T. Klassen, "Ground-fault protection for solar applications," *Littelfuse Inc.*, 2012. [Online]. Available: http://www.littelfuse.com/~/media/electrical/white-papers/littelfuse_ground_fault_solar_applications_white_paper.pdf

[11] J. C. Hernández and P. G. Vidal, "Guidelines for protection against electric shock in PV generators," *Energy Conversion, IEEE Transactions on*, vol. 24, no. 1, pp. 274–282, 2009.

[12] T. Baldwin and F. Renovich, "Analysis of fault locating signals for high-impedance grounded systems," in *Industry Applications Conference, 2001. Thirty-Sixth IAS Annual Meeting. Conference Record of the 2001 IEEE*, vol. 3, Sept 2001, pp. 1823–1830 vol.3.

[13] B. Group, "The power in electrical safety," *Brochure*, no. NAE4001450, 2015. [Online]. Available: http://www.bender.org/documents/Overview_brochure_NAE4001450.pdf

[14] P. Chen, B. Xu, and J. Li, "A traveling wave based fault locating system for HVDC transmission lines," in *Power System Technology, PowerCon 2006. International Conference on.* IEEE, 2006, pp. 1–4.

[15] E. O. Schweitzer, A. Guzmn, M. V. Mynam, V. Skendzic, B. Kasztenny, and S. Marx, "Locating faults by the traveling waves they launch," in *Protective Relay Engineers, 2014 67th Annual Conference for*, March 2014, pp. 95–110.

[16] T. W. Stringfield, D. J. Marihart, and R. F. Stevens, "Fault location methods for overhead lines," *Transactions of the American Institute of Electrical Engineers. Part III: Power Apparatus and Systems*, vol. 76, no. 3, pp. 518–529, April 1957.

[17] S. Marx, B. K. Johnson, A. Guzmán, V. Skendzic, and M. V. Mynam, "Traveling wave fault location in protective relays: Design, testing, and results," in *proceedings of the 16th Annual Georgia Tech Fault and Disturbance Analysis Conference, Atlanta, GA*, 2013.

[18] K. Nanayakkara, A. Rajapakse, and R. Wachal, "Fault Location in Extra Long HVDC Transmission Lines using Continuous Wavelet Transform," in *submitted to the International Conference on Power Systems Transients, Deft, the Netherlands*, 2011.

[19] O. Nanayakkara, A. Rajapakse, and R. Wachal, "Fault Location in Extra Long HVDC Transmission Lines Using Discrete Wavelet Transform," in *Proc. CIGRE Canada Conf. Power Syst*, 2010.

[20] L. Schirone, F. P. Califano, U. Moschella, and U. Rocca, "Fault finding in a 1 mw photovoltaic plant by reflectometry," in *Photovoltaic Energy Conversion, 1994., Conference Record of the Twenty Fourth. IEEE Photovoltaic Specialists Conference - 1994, 1994 IEEE First World Conference on*, vol. 1, Dec 1994, pp. 846–849 vol.1.

[21] M. K. Alam, F. Khan, J. Johnson, and J. Flicker, "PV ground-fault detection using spread spectrum time domain reflectometry (SSTDR)," in *2013 IEEE Energy Conversion Congress and Exposition*, Sept 2013, pp. 1015–102.

[22] M. K. Alam, F. H. Khan, J. Johnson, and J. Flicker, "PV arc-fault detection using spread spectrum time domain reflectometry (SSTDR)," in *2014 IEEE Energy Conversion Congress and Exposition (ECCE)*, Sept 2014, pp. 3294–3300.

[23] S. Singh and D. N. Vishwakarma, "Intelligent techniques for fault diagnosis in transmission lines - An overview," in *Recent Developments in Control, Automation and Power Engineering (RDCAPE), 2015 International Conference on*, March 2015, pp. 280–285.

[24] Z. Chen and J. C. Maun, "Artificial neural network approach to single-ended fault locator for transmission lines," *IEEE Transactions on Power Systems*, vol. 15, no. 1, pp. 370–375, Feb 2000.

[25] M. T. Hagh, K. Razi, and H. Taghizadeh, "Fault Classification and Location of Power Transmission Lines using Artificial Neural Network," in *2007 International Power Engineering Conference (IPEC 2007)*, Dec 2007, pp. 1109–1114.

[26] L. L. Jiang and D. L. Maskell, "Automatic fault detection and diagnosis for photovoltaic systems using combined artificial neural network and analytical based methods," in *2015 International Joint Conference on Neural Networks (IJCNN)*, July 2015, pp. 1–8.

[27] Syafaruddin, E. Karatepe, and T. Hiyama, "Controlling of artificial neural network for fault diagnosis of photovoltaic array," in *Intelligent System Application to Power Systems (ISAP), 2011 16th International Conference on*, Sept 2011, pp. 1–6.

[28] A. M. Gaouda, E. F. El-Saadany, M. M. A. Salama, V. K. Sood, and A. Y. Chikhani, "Monitoring HVDC systems using wavelet multi-resolution analysis," *IEEE Transactions on Power Systems*, vol. 16, no. 4, pp. 662–670, Nov 2001.

[29] S. Ekici and S. Yildirim, "Fault location estimation on transmission lines using wavelet transform and artificial neural network." in *IC-AI*, 2006, pp. 181–184.

[30] W. J. Cheong and R. K. Aggarwal, "Accurate fault location in high voltage transmission systems comprising an improved thyristor controlled series capacitor model using wavelet transforms and neural network," in *Transmission and Distribution Conference and Exhibition 2002: Asia Pacific. IEEE/PES*, vol. 2, Oct 2002, pp. 840–845 vol.2.

[31] Y. Pan, "Noise pattern analysis based ground fault location approach for ungrounded electrical distribution systems," Ph.D. dissertation, THE FLORIDA STATE UNIVERSITY, Tallahassee, FL, 2009.

[32] Y. Pan, P. M. Silveira, M. Steurer, T. L. Baldwin, and P. F. Ribeiro, "A fault location approach for high-impedance grounded DC shipboard power distribution systems," in *Power and Energy Society General Meeting - Conversion and Delivery of Electrical Energy in the 21st Century, 2008 IEEE*, July 2008, pp. 1–6.

[33] Y. Pan, M. Steurer, and T. L. Baldwin, "Ground fault location testing of a noise-pattern-based approach on an ungrounded dc system," *IEEE Transactions on Industry Applications*, vol. 47, no. 2, pp. 996–1002, March 2011.

[34] W. Li, A. Monti, and F. Ponci, "Fault detection and classification in medium voltage dc shipboard power systems with wavelets and artificial neural networks," *IEEE Transactions on Instrumentation and Measurement*, vol. 63, no. 11, pp. 2651–2665, Nov 2014.

[35] S. Pederson and R. Gokaraju, "Ground Fault Location in Ungrounded Large Scale PV Generators," in *IEEE PES General Meeting, Student Poster Presentation*, Vancouver, BC, Canada, July 2013.

[36] J. Mahseredjian, V. Dinavahi, and J. A. Martinez, "Simulation tools for electromagnetic transients in power systems: Overview and challenges," *IEEE Transactions on Power Delivery*, vol. 24, no. 3, pp. 1657–1669, July 2009.

[37] R. Technologies, *RTDS Users Manual*, Winnipeg, Canada.

[38] P. Forsyth and R. Kuffel, "Utility applications of a RTD$S^{®}$ simulator," in *Power Engineering Conference, 2007. IPEC 2007. International.* IEEE, 2007, pp. 112–117.

[39] T. M. J. Giesbrecht, "Small time-step ($< 2\mu$sec) VSC model for the real time digital simulator," in *Proc 2005 International Conference on Power Systems Transients*, no. IPST05-168, June 2005.

[40] J.-M. Kwon, B.-H. Kwon, and K.-H. Nam, "Grid-connected photovoltaic multistring PCS with PV current variation reduction control," *Industrial Electronics, IEEE Transactions on*, vol. 56, no. 11, pp. 4381–4388, Nov 2009.

[41] M. Meinhardt, G. Cramer, B. Burger, and P. Zacharias, "Multi-string-converter with reduced specific costs and enhanced functionality," *Solar Energy*, vol. 69, Supplement 6, pp. 217 – 227, 2001, {EUROSUN} 2000 Selected Proceedings.

[42] M. Calais, J. Myrzik, T. Spooner, and V. Agelidis, "Inverters for single-phase grid connected photovoltaic systems-an overview," in *Power Electronics Specialists Conference, 2002. pesc 02. 2002 IEEE 33rd Annual*, vol. 4, 2002, pp. 1995–2000.

[43] F. Blaabjerg, F. Iov, R. Teodorescu, and Z. Chen, "Power electronics in renewable energy systems," in *Power Electronics and Motion Control Conference, 2006. EPE-PEMC 2006. 12th International*, Aug 2006, pp. 1–17.

[44] H. Ghoddami, "Enhanced voltage-sourced inverters for large-scale grid-connected photovoltaic systems," Ph.D. dissertation, The University of Western Ontario, 2013.

[45] A. E. I. Inc., "Advantages of distributed and central architectures in solar arrays," July 2013. [Online]. Available: http://www.grosolar.com/content/advanced-energy-white-paper

[46] J. Gow and C. Manning, "Development of a photovoltaic array model for use in power-electronics simulation studies," *Electric Power Applications, IEE Proceedings* -, vol. 146, no. 2, pp. 193–200, Mar 1999.

[47] M. Villalva, J. Gazoli, and E. Filho, "Comprehensive approach to modeling and simulation of photovoltaic arrays," *Power Electronics, IEEE Transactions on*, vol. 24, no. 5, pp. 1198–1208, May 2009.

[48] J. Hernández, P. Vidal, and A. Medina, "Characterization of the insulation and leakage currents of PV generators: Relevance for human safety," *Renewable Energy*, vol. 35, no. 3, pp. 593–601, 2010.

[49] S. S. T. Inc., "Capacitive leakage currents," Technical Information. [Online]. Available: https://www.researchgate.net/file.PostFileLoader.html?id=55ae2b6b614325ac2a8b45d7&assetKey=AS%3A273815953707010%401442294218952

[50] D. Sera, L. Mathe, T. Kerekes, S. Spataru, and R. Teodorescu, "On the perturb-and-observe and incremental conductance MPPT methods for PV systems," *Photovoltaics, IEEE Journal of*, vol. 3, no. 3, pp. 1070–1078, July 2013.

[51] M. Masoum, H. Dehbonei, and E. Fuchs, "Theoretical and experimental analyses of photovoltaic systems with voltageand current-based maximum power-point tracking," *Energy Conversion, IEEE Transactions on*, vol. 17, no. 4, pp. 514–522, Dec 2002.

[52] G. Farivar, B. Asaei, and S. Mehrnami, "An analytical solution for tracking photovoltaic module MPP," *Photovoltaics, IEEE Journal of*, vol. 3, no. 3, pp. 1053–1061, July 2013.

[53] W. Xiao, M. Lind, W. Dunford, and A. Capel, "Real-time identification of optimal operating points in photovoltaic power systems," *Industrial Electronics, IEEE Transactions on*, vol. 53, no. 4, pp. 1017–1026, June 2006.

[54] P. Vinay and M. Mathews, "Modelling and analysis of artificial intelligence based MPPT techniques for PV applications," in *Advances in Green Energy (ICAGE), 2014 International Conference on*, Dec 2014, pp. 56–65.

[55] A. Kalbat, "PSCAD simulation of grid-tied photovoltaic systems and total harmonic distortion analysis," in *Electric Power and Energy Conversion Systems (EPECS), 2013 3rd International Conference on*, Oct 2013, pp. 1–6.

[56] N. Mohan and T. M. Undeland, *Power electronics: converters, applications, and design*. John Wiley & Sons, 2007.

[57] S. Mouhadjer, A. Chermitti, and A. Neçaibia, "Comprehensive and field study to design a buck converter for photovoltaic systems," *Revue des Energies Renouvelables*, vol. 15, no. 2, pp. 321–330, 2012.

[58] B. Wu, *High-power converters and AC drives*. John Wiley & Sons, 2006.

[59] T. Kalitjuka, "Control of voltage source converters for power system applications," 2011.

[60] Y. Porasad and H. Hosseinzadeh, "Comparison of voltage control and current control methods in grid connected inverters," *Journal of Applied Sciences*, vol. 8, no. 4, pp. 648–653, 2008.

[61] B. Yin, R. Oruganti, S. Panda, and A. Bhat, "Performance comparison of voltage mode control and current mode control of a three-phase pwm rectifier based on a dual SISO

model," in *IEEE Industrial Electronics, IECON 2006 - 32nd Annual Conference on*, Nov 2006, pp. 1908–1914.

[62] J. Svensson, "Grid-connected voltage source converter," Ph.D. dissertation, Chalmers University of Technology Göteborg, Sweden, 1998.

[63] K. Chatterjee, B. Fernandes, and G. Dubey, "An instantaneous reactive volt-ampere compensator and harmonic suppressor system," *Power Electronics, IEEE Transactions on*, vol. 14, no. 2, pp. 381–392, Mar 1999.

[64] K. Ahmed, S. Finney, and B. Williams, "Passive filter design for three-phase inverter interfacing in distributed generation," in *Compatibility in Power Electronics, 2007. CPE '07*, May 2007, pp. 1–9.

[65] "IEEE recommended practices and requirements for harmonic control in electrical power systems," *IEEE Std 519-1992*, pp. 1–112, April 1993.

[66] B. Liu and B.-M. Song, "Modeling and analysis of an LCL filter for grid-connected inverters in wind power generation systems," in *Power and Energy Society General Meeting, 2011 IEEE*, July 2011, pp. 1–6.

[67] E. Bjerkan, "High frequency modeling of power transformers : Stresses and diagnostics," Ph.D. dissertation, Norwegian University of Science and Technology, Department of Electrical Power Engineering, 2005.

[68] A. Pokryvailo, "Accounting for parasitic parameters in high-voltage converters."

[69] S. Chimklai, "High-frequency transformer model for switching transient studies," Ph.D. dissertation, University of British Columbia, 1995.

[70] A. Fernandes and W. Neves, "Phase-domain transmission line models considering frequency-dependent transformation matrices," *Power Delivery, IEEE Transactions on*, vol. 19, no. 2, pp. 708–714, April 2004.

[71] J. Marti, "Accurate modelling of frequency-dependent transmission lines in electromagnetic transient simulations," *Power Apparatus and Systems, IEEE Transactions on*, vol. PAS-101, no. 1, pp. 147–157, Jan 1982.

[72] L. Marti, "Simulation of transients in underground cables with frequency-dependent modal transformation matrices," *Power Delivery, IEEE Transactions on*, vol. 3, no. 3, pp. 1099–1110, Jul 1988.

[73] L. Colla, S. Lauria, and F. Palone, "Finite sections modeling of power cable systems," in *Proc 2011 International Conference on Power Systems Transients*, 2011, pp. 14–17.

[74] C. H. Kim and R. Aggarwal, "Wavelet transforms in power systems. i. general introduction to the wavelet transforms," *Power Engineering Journal*, vol. 14, no. 2, pp. 81–87, April 2000.

[75] O. Chaari, M. Meunier, and F. Brouaye, "Wavelets: a new tool for the resonant grounded power distribution systems relaying," *IEEE Transactions on Power Delivery*, vol. 11, no. 3, pp. 1301–1308, Jul 1996.

[76] F. H. Magnago and A. Abur, "Fault location using wavelets," *IEEE Transactions on Power Delivery*, vol. 13, no. 4, pp. 1475–1480, Oct 1998.

[77] F. Martin and J. A. Aguado, "Wavelet-based ANN approach for transmission line protection," *IEEE Transactions on Power Delivery*, vol. 18, no. 4, pp. 1572–1574, Oct 2003.

[78] S. Santoso, E. J. Powers, and W. M. Grady, "Electric power quality disturbance detection using wavelet transform analysis," in *Time-Frequency and Time-Scale Analysis, 1994., Proceedings of the IEEE-SP International Symposium on*, Oct 1994, pp. 166–169.

[79] I. S. Kim, "Fault detection algorithm of the photovoltaic system using wavelet transform," in *Power Electronics (IICPE), 2010 India International Conference on*, Jan 2011, pp. 1–6.

[80] M. Davarifar, A. Rabhi, A. Hajjaji, E. Kamal, and Z. Daneshifar, "Partial shading fault diagnosis in pv system with discrete wavelet transform (dwt)," in *Renewable Energy Research and Application (ICRERA), 2014 International Conference on*, Oct 2014, pp. 810–814.

[81] Z. Wang, S. McConnell, R. S. Balog, and J. Johnson, "Arc fault signal detection-fourier transformation vs. wavelet decomposition techniques using synthesized data," in *Photovoltaic Specialist Conference (PVSC), 2014 IEEE 40th.* IEEE, 2014, pp. 3239–3244.

[82] D. C. Robertson, O. I. Camps, J. S. Mayer, and W. B. Gish, "Wavelets and electromagnetic power system transients," *IEEE Transactions on Power Delivery*, vol. 11, no. 2, pp. 1050–1058, Apr 1996.

[83] S. G. Mallat, "A theory for multiresolution signal decomposition: the wavelet representation," *IEEE Transactions on Pattern Analysis and Machine Intelligence*, vol. 11, no. 7, pp. 674–693, Jul 1989.

[84] C. S. Burrus, R. A. Gopinath, and H. Guo, "Introduction to wavelets and wavelet transforms," 1997.

[85] T. M. Lai, L. A. Snider, E. Lo, and D. Sutanto, "High-impedance fault detection using discrete wavelet transform and frequency range and rms conversion," *IEEE Transactions on Power Delivery*, vol. 20, no. 1, pp. 397–407, Jan 2005.

[86] A. I. Megahed, A. M. Moussa, H. B. Elrefaie, and Y. M. Marghany, "Selection of a suitable mother wavelet for analyzing power system fault transients," in *Power and Energy Society General Meeting - Conversion and Delivery of Electrical Energy in the 21st Century, 2008 IEEE*, July 2008, pp. 1–7.

[87] J. Antonino-Daviu, M. Riera-Guasp, J. Roger-Folch, F. Martnez-Gimnez, and A. Peris, "Application and optimization of the discrete wavelet transform for the detection of broken rotor bars in induction machines," *Applied and Computational Harmonic Analysis*, vol. 21, no. 2, pp. 268 – 279, 2006.

[88] J. Gracia, A. J. Mazon, and I. Zamora, "Best ANN structures for fault location in single-and double-circuit transmission lines," *IEEE Transactions on Power Delivery*, vol. 20, no. 4, pp. 2389–2395, Oct 2005.

[89] M. H. Bollen and I. Gu, *Signal processing of power quality disturbances*. John Wiley & Sons, 2006, vol. 30.

[90] H. Demuth, M. Beale, and M. Hagan, *Neural Network Toolbox^{TM}, Users Guide*. Natick, MA, USA: Mathworks Inc., 2016.

[91] S. Haykin, *Neural networks: A Comprehensive Foundation*, 2nd ed. Upper Saddle River, NJ, USA: Prentice Hall Inc., 1999.

[92] N. K. Chanda and Y. Fu, "ANN-based fault classification and location in MVDC shipboard power systems," in *North American Power Symposium (NAPS), 2011*, Aug 2011, pp. 1–7.

[93] M. T. Hagan, H. B. Demuth, M. H. Beale, and O. De Jesús, *Neural network design*. PWS publishing company Boston, 1996, vol. 20.

[94] M. Uyar, S. Yildirim, and M. T. Gencoglu, "An effective wavelet-based feature extraction method for classification of power quality disturbance signals," *Electric Power Systems Research*, vol. 78, no. 10, pp. 1747–1755, 2008.

Appendix A

System Data

A.1 PV Array Parameters

Table A.1: 500 kWp PV array test system data

PV Module parameters (@STC: 1,000 W/m^2, 25^0 C)	**Value**
Max. Power (P_{max})	315 W
Max. power voltage (V_{mp})	39.8 V
Max. power current (I_{mp})	7.92 A
Open circuit voltage (V_{oc})	49.2 V
Short circuit current (I_{oc})	8.5 A
Number of series connected cells per module (N_c)	72
Number of parallel strings of cells (N_{cp})	1
Short circuit current temperature coefficient (J_{tmp})	0.061 %/degC
Open circuit voltage temperature coefficient (K_v)	-0.36 %/degC
Open circuit series resistance (R_{so})	0.5 Ω
Short circuit shunt resistance (R_{sho})	100 Ω
Number of series modules in a string (N_s)	17
Number of parallel strings (N_p)	48

A.2 PV Array Parasitic Elements

Table A.2: PV array parasitic data (at STC with 50% humidity)

Parameters	250 kWp	2.825 kWp	1.576 kWp
R_{iso}	0.3264 MΩ	28.885 MΩ	51.77 MΩ
C_{lek}	33.0875 μF	0.3738 μF	0.208 μF
R_s	8.41 MΩ	8.386 MΩ	6.68 MΩ
R_p	252.38 MΩ	251.579 MΩ	200.4 MΩ

A.3 Buck Converter Parameters

Table A.3: Buck converter test system data

DC-DC Converter Parameters	Value
Nominal power	250 kVA
Nominal voltage	600 Vdc
Switching frequency	1.8 kHz
Inductance	0.3 mH
Input capacitance	10000 μF
Controller Parameters	Value
Proportional gain (k_p)	10
Integral gain (k_i)	1
Integral time constant (τ_i)	0.2 s

A.4 Voltage Source Inverter (VSI) Parameters

Table A.4: Inverter test system data

VSI Parameters	Value
Nominal power	500 kVA
Nominal input voltage	600 Vdc
Nominal output voltage	210 Vac
Switching frequency	3.0 kHz
DC link capacitor(C_{dc})	95000 μF
Interface resistance (R_f)	0.01 mΩ
Interface inductance (L_f)	68.2 μH
High-pass filter capacitance (C_f)	3007.5 μF
High-pass filter resistance (R_{hf})	0.0177 Ω
High-pass filter inductance (L_{hf})	0.935 μH
P-Controller Parameters	
Proportional gain (k_p)	0.4
Integral gain (k_i)	1
Integral time constant (τ_i)	0.1 s
Q-Controller Parameters	
Proportional gain (k_p)	0.2
Integral gain (k_i)	1
Integral time constant (τ_i)	0.1 s

A.5 Transformer Parameters

Table A.5: Transformer test system data

Transformer Parameters	Value
Power rating	500 kVA
Voltage ratio	0.21/20 kV
Frequency	60 Hz
Phase	3
Connection	Δ/Y
Leakage inductance	0.05 p.u
Magnetizing current	1 %
Transformer Parasitic	Value
Capacitance C_{LG}, C_{HG} and C_{HL}	5 pF
Resistance R_{LG}, R_{HG} and R_{HL}	10 Ω

A.6 Load and Grid Parameters

Table A.6: Load and grid test system data

Grid Parameters	Value
Voltage	20 kV
Frequency	60 Hz
Source impedance type	L
Impedance	0.05 H
Dynamic Load Parameters	Value
Type	RL
Voltage	0.21 kV
Frequency	60 Hz
Active power	0.1 MW
Reactive power	0.01 MVAR

Appendix B

B.1 Cable physical parameters

Table B.1: Physical parameters of cables used in test system

Parameters	Cable 1 and Cable 2	Cable 3
Location	Buck converter to DC bus	DC bus to inverter input
Total length	90 m	200 m
Voltage rating	1 kV	1 kV
Base frequency	60 Hz	60 Hz
Size	250 MCM	750 MCM
Conductor outer radius	6.35 mm	11 mm
Conductor resistivity	1.68 $\times 10^{-}8$ Ωm	1.68 $\times 10^{-}8$ Ωm
Insulator outer radius	16.383 mm	21.463 mm
Insulator relative permittivity	3.19	3.19

B.2 Data preparation for the frequency dependent π cable model

The frequency dependent π cable model parameters of 30 m (section of cable 1 and 2) and 100 m long cables (section of cable 3) are obtained using following calculation steps:

- The resistance ($R_{modal}(\omega)$), inductance ($L_{modal}(\omega)$), capacitance ($C_{modal}(\omega)$) and impedance ($Z_{modal}(\omega)$) values of short cable are obtained for various frequencies (ω) either by measurement or by offline electromagnetic simulation using frequency dependent (modal) cable model. The logarithmic plot of resistance ($R_{modal}(\omega)$) as a function of frequency has been plotted in Figure B.1.

- Then three transition frequencies and respective resistance values are selected as shown

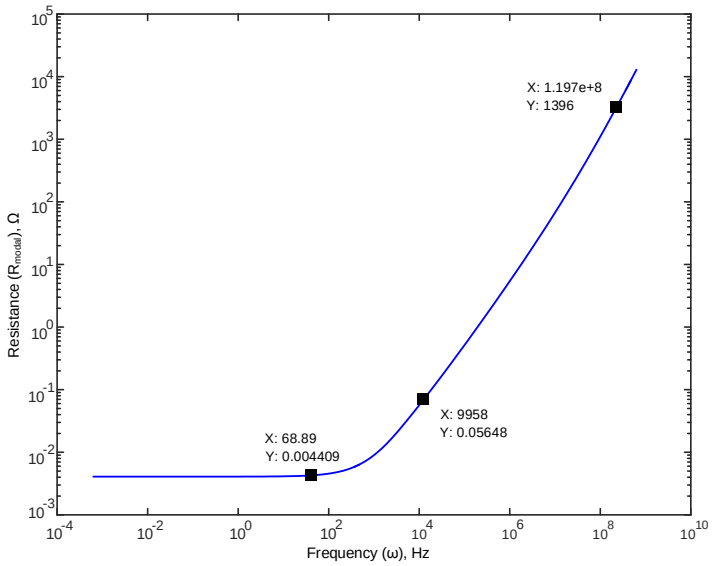

Figure B.1: Logarithmic plot of resistance of 30 m cable as a function of frequency

in Figure B.1. Suppose these frequencies and resistance pairs are (Z_{R1}, ω_{R1}), (Z_{R2}, ω_{R2}) and (Z_{R3}, ω_{R3}), where $\omega_{R1} < \omega_{R2} < \omega_{R3}$. By comparing Figure B.1 with typical plot of frequency dependent resistance Figure 2.22, the following parameters could be determined;

$$\begin{aligned} R_1 &= Z_{R3} \\ L_1 &= \frac{R_1}{\omega_{R3}} \\ R_2 &= \frac{L_1}{\omega_{R2}} \\ L_2 &= \frac{R_2}{\omega_{R2}} \\ R_3 &= \frac{Z_{R1}.Z_{R2}}{Z_{R1} - Z_{R2}} \end{aligned} \tag{B.1}$$

- The impedance of frequency dependent resistance ($Z_R(\omega) = R_r(\omega) + jX_r(\omega)$) is calculated using Equation 2.21.

- The fixed inductance (L_5) is obtained from following equations:

$$\begin{aligned} L_{in}(\omega) &= L_{modal}(\omega) - \frac{X_r(\omega)}{\omega} \\ L_5 &= \frac{1}{3}.min(L_{in}(\omega)) \\ L_{FDLARR} &= L_{in}(\omega) - L_5 \end{aligned} \tag{B.2}$$

- The logarithmic plot of inductance (L_{FDLARR}) as a function of frequency (ω) is plotted in Figure B.2 and compared with typical frequency dependent inductance plot shown in Figure 2.23. The three transition frequencies and respective inductance, (Z_{L1}, ω_{L1}), (Z_{L2}, ω_{L2}) and (Z_{L3}, ω_{L3}), where $\omega_{L1} < \omega_{L2} < \omega_{L3}$ are selected from Figure B.2 and the parameters of the frequency dependent inductance part are obtained as follows:

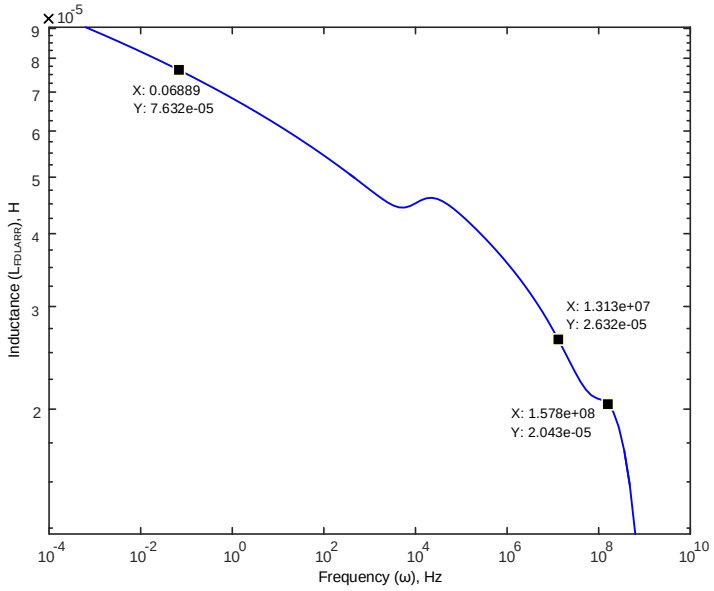

Figure B.2: Logarithmic plot of inductance (L_{FDLARR}) as a function of frequency

$$
\begin{aligned}
L_3 &= Z_{L1} \\
L_4 &= \frac{L_3.Z_{L2}}{L_3 - Z_{L2}} \\
R_{4.1} &= L_3 \times \omega_{L1} \\
R_{4.2} &= L_4 \times \omega_{L2} \\
R_4 &= \sqrt{R_{4.1} \times R_{4.2}} \\
R_5 &= L_4 \times \omega_{L3}
\end{aligned}
\tag{B.3}
$$

- The impedance of frequency dependent inductance ($Z_L(\omega) = R_l(\omega) + jX_l(\omega)$) is calculated using Equation 2.22. The total resistance and inductance of 30 m cable calculated from frequency dependent π model are given by:

$$
\begin{aligned}
R_{pi}(\omega) &= R_r(\omega) + R_l(\omega) \\
L_{pi}(\omega) &= \frac{X_r(\omega)}{\omega} + \frac{X_l(\omega)}{\omega} + L_5
\end{aligned}
\tag{B.4}
$$

  The comparison plot between actual frequency dependent modal resistance and inductance with total resistance and inductance calculated from frequency dependent π model are shown in Figure B.3.

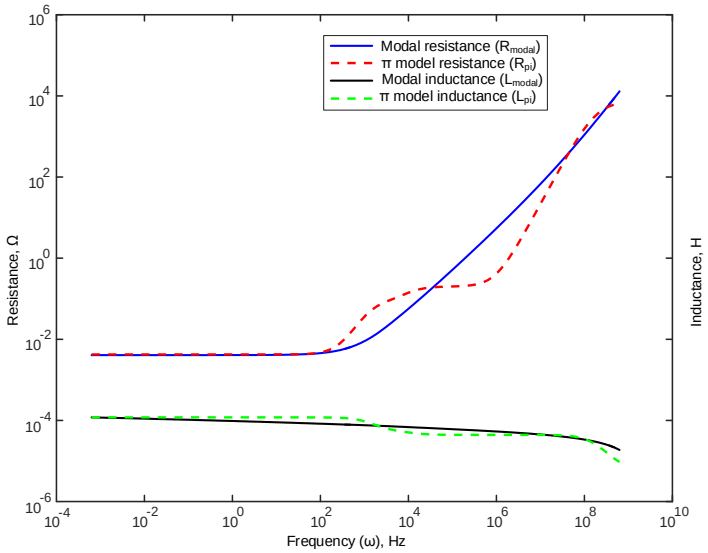

Figure B.3: Comparison between frequency dependent modal and π model parameters

- The impedance ($Z_{pi}(\omega)$) of the cable calculated from frequency dependent π model is equal to:

$$\begin{aligned} Z_{pi}(\omega) &= R_{pi}(\omega) + j.\omega.L_{pi}(\omega) \\ &= |Z_{pi}(\omega)|\angle Z_{pi}(\omega) \end{aligned} \tag{B.5}$$

The magnitude and phase of the cable impedance calculated using frequency dependent (modal) model or from measurement data and frequency dependent π cable model are plotted and compared in Figure B.4. From figures B.3 and figure B.4, it can be seen that the frequency dependent π cable model parameters are satisfactorily close to the parameters from frequency dependent (modal) model or parameters from experimental data.

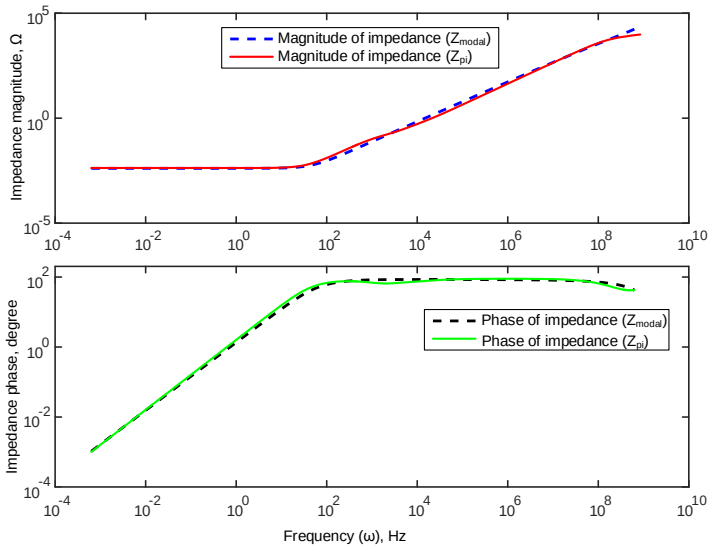

Figure B.4: Impedance magnitude and phase comparison between frequency dependent modal and π model parameters

- The shunt capacitance of the cable is constant for all frequencies. The resistance (R_{shnt}) of the RC branches is very small and can be neglected. Therefore, the shunt capacitance of the frequency dependent π cable model is determined as:

$$C_{shnt} = \frac{1}{2} C_{modal}(\omega) \tag{B.6}$$

B.3 Frequency dependent π cable model parameters

Table B.2: Frequency dependent π cable model parameters

Parameters	30 m section of cable 1	100 m section of cable 3
R_1	1396 Ω	1151 Ω
R_2	0.1161 Ω	0.2193 Ω
R_3	0.0044 Ω	0.0047 Ω
R_4	0.1664 Ω	0.4203 Ω
R_5	5858.9 Ω	11243 Ω
L_1	1.1662 $\times 10^{-}5$ H	2.9036 $\times 10^{-}5$ H
L_2	1.1662 $\times 10^{-}5$ H	2.9036 $\times 10^{-}5$ H
L_3	9.0410 $\times 10^{-}5$ H	3.007 $\times 10^{-}4$ H
L_4	3.7129 $\times 10^{-}5$ H	1.2379 $\times 10^{-}4$ H
L_5	6.1041 $\times 10^{-}5$ H	1.7098 $\times 10^{-}5$ H
C_{sht}	0.004402 μ F	0.02087 μ F